

HELICAL RAIL GUNS: THE APPLICATION OF LINEAR ELECTRIC MOTORS
TO AIRCRAFT LAUNCHING

by

Osa Edward Fitch

SUBMITTED TO THE DEPARTMENT OF AERONAUTICS AND ASTRONAUTICS
IN PARTIAL FULFILLMENT OF THE REQUIREMENTS
OF THE DEGREE OF MASTER OF SCIENCE

and

SUBMITTED TO THE DEPARTMENT OF PHYSICS
IN PARTIAL FULFILLMENT OF THE REQUIREMENTS
OF THE DEGREE OF BACHELOR OF SCIENCE

at the

MASSACHUSETTS INSTITUTE OF TECHNOLOGY

April 1982

© Massachusetts Institute of Technology 1982

Signature of Author Signature redacted
Department of Aeronautics and Astronautics
Department of Physics
April 30, 1982

Certified by Signature redacted
Henry H. Kolm
Thesis Supervisor

Accepted by Signature redacted
Harold Y. Wachman
Chairman, Aero/Astro Departmental Graduate Committee

Accepted by Signature redacted
George F. Koster
Chairman, Physics Departmental Committee

Archives

MASSACHUSETTS INSTITUTE
OF TECHNOLOGY

MAY 26 1982 ✓

LIBRARIES

HELICAL RAIL GUNS: THE APPLICATION OF LINEAR ELECTRIC MOTORS
TO AIRCRAFT LAUNCHING

by

OSA EDWARD FITCH

Submitted to the Department of Aeronautics and Astronautics
on April 30, 1982 in partial fulfillment of the requirements
of the Degree of Master of Science
and submitted to the Department of Physics
on April 30, 1982 in partial fulfillment of the requirements
of the Degree of Bachelor of Science

ABSTRACT

The class of linear electric motors known as helical rail guns is described and defined. The theory of operation of such a device is explained. Its thermal, mechanical and electrical limits are explored.

The construction and testing of three of these devices by the Electromagnetic Acceleration Group at MIT's National Magnet Laboratory is described. A small bench-top helical rail gun was first built and tested. Next, a longer 4 meter helical rail gun was constructed for the purpose of launching model gliders. Finally, a saddle bucket was tested on the helix of the bench-top model for proof of feasibility.

The application of helical rail guns to aircraft launching is next examined. A number of different tasks for helical rail guns are found to be feasible, including launching military aircraft from ships and hangars, and launching commercial aircraft from airports.

Thesis Supervisor: Dr. Henry H. Kolm

Title: Senior Research Scientist

TABLE OF CONTENTS

	Page
ABSTRACT.....	2
ACKNOWLEDGEMENTS.....	5
I. INTRODUCTION.....	7
II. THEORY.....	17
1. Elementary Limits.....	17
1.1 Thermal Limits.....	19
1.2 Mechanical Limits.....	24
1.3 Electrical Limits.....	34
1.4 Scaling Limits.....	52
2. Coupling to the Load.....	53
2.1 Inside Geometries.....	54
2.2 Outside Geometries.....	57
2.3 Saddle Buckets.....	59
3. Efficiency.....	62
4. Exotic Solutions.....	67
4.1 Permanent Magnet Buckets.....	68
4.2 Ferromagnetic Buckets.....	74
4.3 Exotic Solution Conclusions.....	82
III. EXPERIMENTAL RESULTS.....	84
1. 1-Meter Bench-Top Helical Rail Gun.....	84
2. Glider Launcher.....	87
2.1 Construction.....	89
2.2 Capacitor Banks.....	97
2.3 Testing.....	102

2.3.1 Experimental Limits.....	104
2.3.2 Fault Conditions.....	109
3. Saddle Bucket Tests.....	115
IV. HELICAL RAIL GUN DESIGN CONSIDERATIONS.....	120
1. Motivation.....	120
2. Design Method and Point Designs.....	125
2.1 Design Method.....	126
2.2 Design Example: Navy Catapult.....	139
2.3 Point Design: Air Force Fighter Launcher..	147
2.4 Point Design: Harrier Launcher.....	150
2.5 Point Design: Airliner Launcher.....	157
3. Power Supplies.....	159
V. CONCLUSIONS.....	162
APPENDICES.....	164
BIOGRAPHICAL NOTE.....	184
BIBLIOGRAPHY.....	185

ACKNOWLEDGEMENTS

This thesis represents the culmination of my work here at MIT, and it has not been done in a vacuum. Quite the contrary! Without the encouragement and support of the Electromagnetic Acceleration Crew at the National Magnet Lab my task would have been far more difficult and my life much less enjoyable over that period of time. In particular I would like to thank Whitney Hamnett, Marc Zeitlin, Adrian Nye, and Dave Cope for their help, and Fred Williams for his sometimes offbeat, but always thought provoking ideas. I would also like to thank Ken McKinney for his friendship and help both inside and outside the group, for as long as I've known him, and Henry Kolm for his guidance and hospitality, as well as his expert direction of this motley crew. Perhaps most of all I would like to thank Peter Mongeau for his invaluable direction, help and advice, not to mention his ability to put up with my penchant for argument. Without him, much would not have gotten done, little would have been designed, and this thesis would have turned out far differently. He has also been a good friend.

Finally I would like to thank my parents. All too often I have encountered people who, for one reason or another, have had to struggle to achieve against great opposition, either without the help of their parents, or in direct conflict with them. For me, this has not been the case, and I am

indeed fortunate because of it. My parents have encouraged me in all of my endeavours, from learning to read, through attending MIT, always urging me to do my best, and never attempting to fit me into a mold. In the last analysis it can be said with all honesty that they are responsible for much of my success and happiness. I love you Mom and Dad, and I dedicate this work to you.

I. Introduction.

This thesis deals with a unique class of linear electric motors known as helical rail guns. Helical rail guns have existed since at least 1961, when Thom and Norwood performed experiments at Langley Research Center. However, the concept lay dormant until it was independently reinvented by the Electromagnetic Acceleration Group at MIT's National Magnet Laboratory in 1979 in the course of a study of the feasibility of many different types of mass drivers (a generic term for electromagnetic macro-particle accelerators). Since that time, helical rail gun technology has matured enormously, and has proven to be capable of performing many varied tasks.

Helical rail guns are linear, brush commutated, DC electric motors, which are well suited to accelerating large masses (kilograms to tonnes) to low or moderate velocities (less than one kilometer per second). They have the following characteristic components: a stator, which consists of a conducting helix with insulated turns and one surface (inside or outside) of exposed conductor; commutating helix brushes, which slide on the exposed conductor of the helix and energize a section of it; and a moveable armature, known as the bucket (from early mass driver research), which slides along the helix and generates the force needed to accelerate a payload. The commutating brushes are rigidly attached to the bucket, and the section

of helix they energize is known as the drive coil (again from early mass driver research).

Additionally, provision must be made for delivering power to the bucket. This can be accomplished with brushes sliding on feed-rails, or in some cases by a tether of flexible power cables. Figure I.1 shows a helical rail gun illustrating these basic components.

Within these constraints helical rail guns are incredibly flexible. Since the commutating brushes can be wired to produce either polarity of magnetic field, two drive coils can be used with a single bucket and configured so that the drive coil ahead attracts the bucket, while the drive coil behind repels the bucket. In similar fashion, two bucket coils can be used with a single drive coil to produce the same effect.

Another option is the use of either active or passive buckets. An active bucket consists of energized windings, similar to the drive coil. A passive bucket consists of either permanent magnets or soft iron, neither of which is energized. In both cases the thrust is produced by the magnetic interaction between the bucket and the drive coil; the only significant difference is that passive buckets using soft iron (i.e. ferromagnets) are limited to "pull only" drive coils. With either type of bucket power must still be supplied to the bucket assembly to energize the drive coils through the commutating helix brushes. Figure I.2 illustrates these basic electrical wiring schemes.

Figure I.1

Helical Rail Gun Basic Components

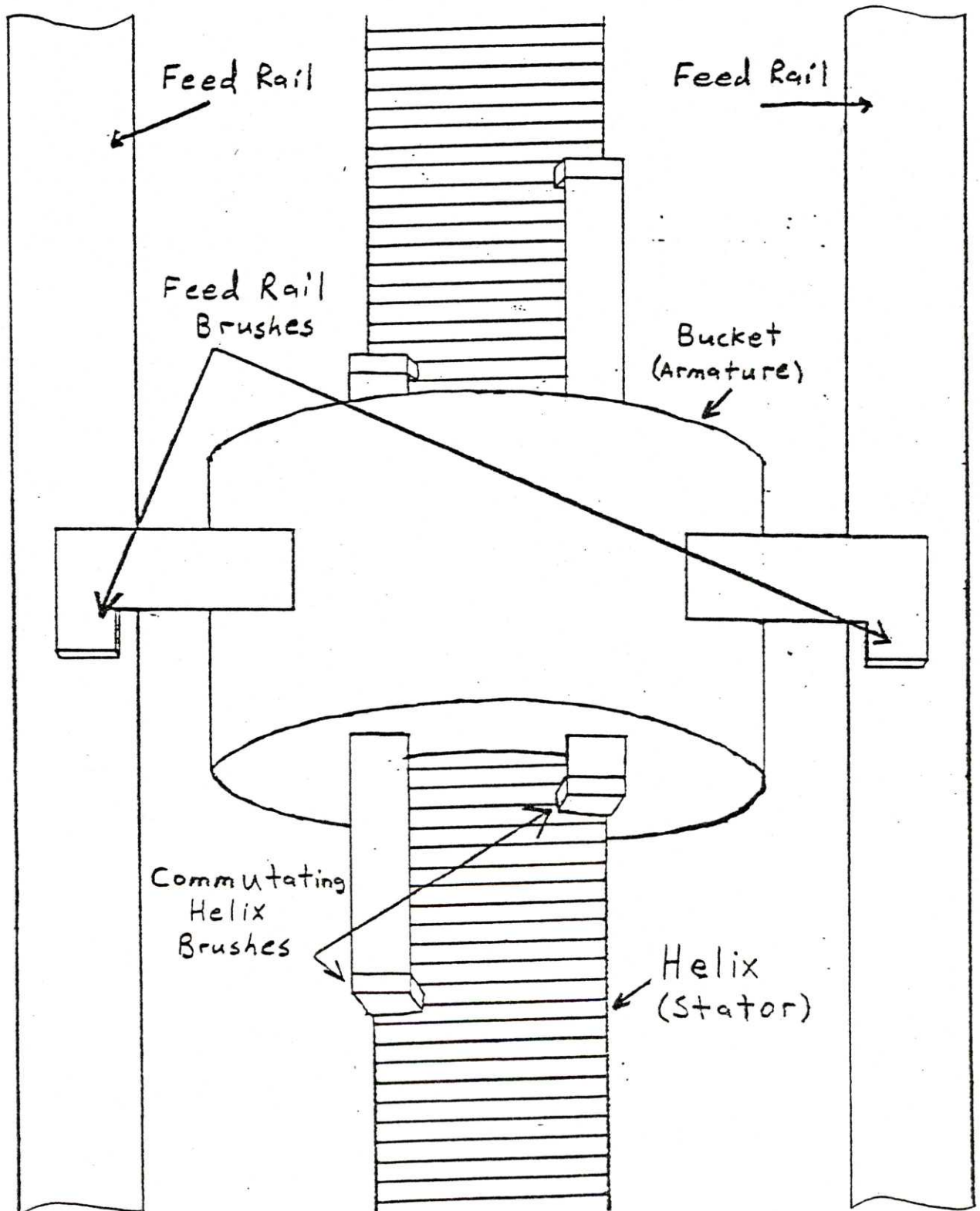
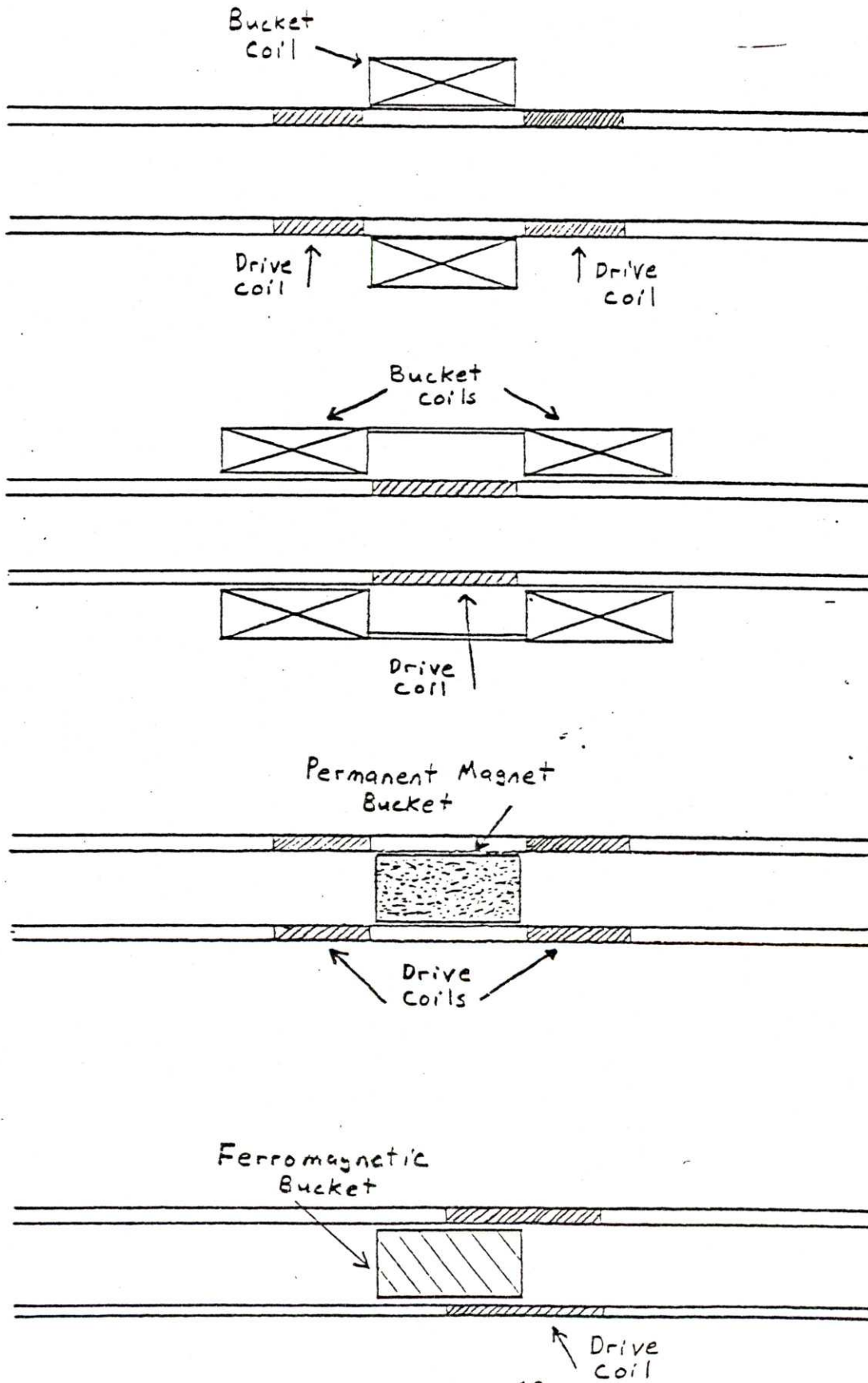


Figure I.2

Helical Rail Gun Basic Wiring Schemes



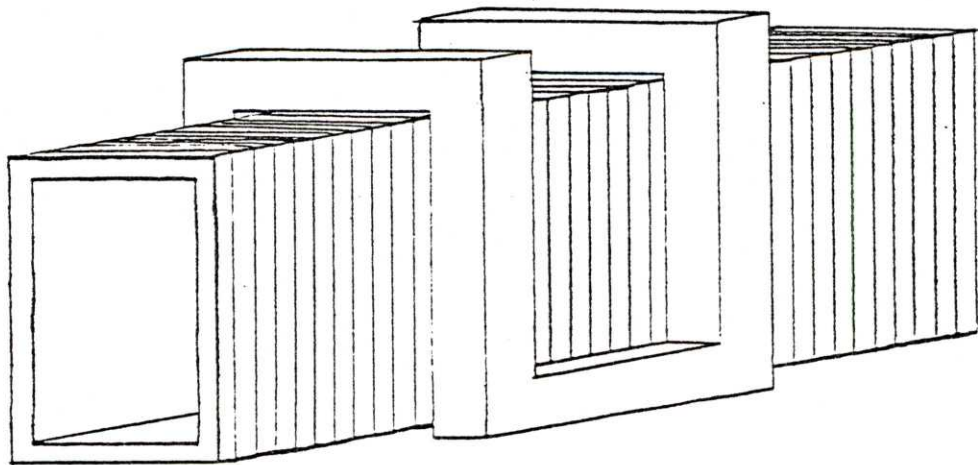
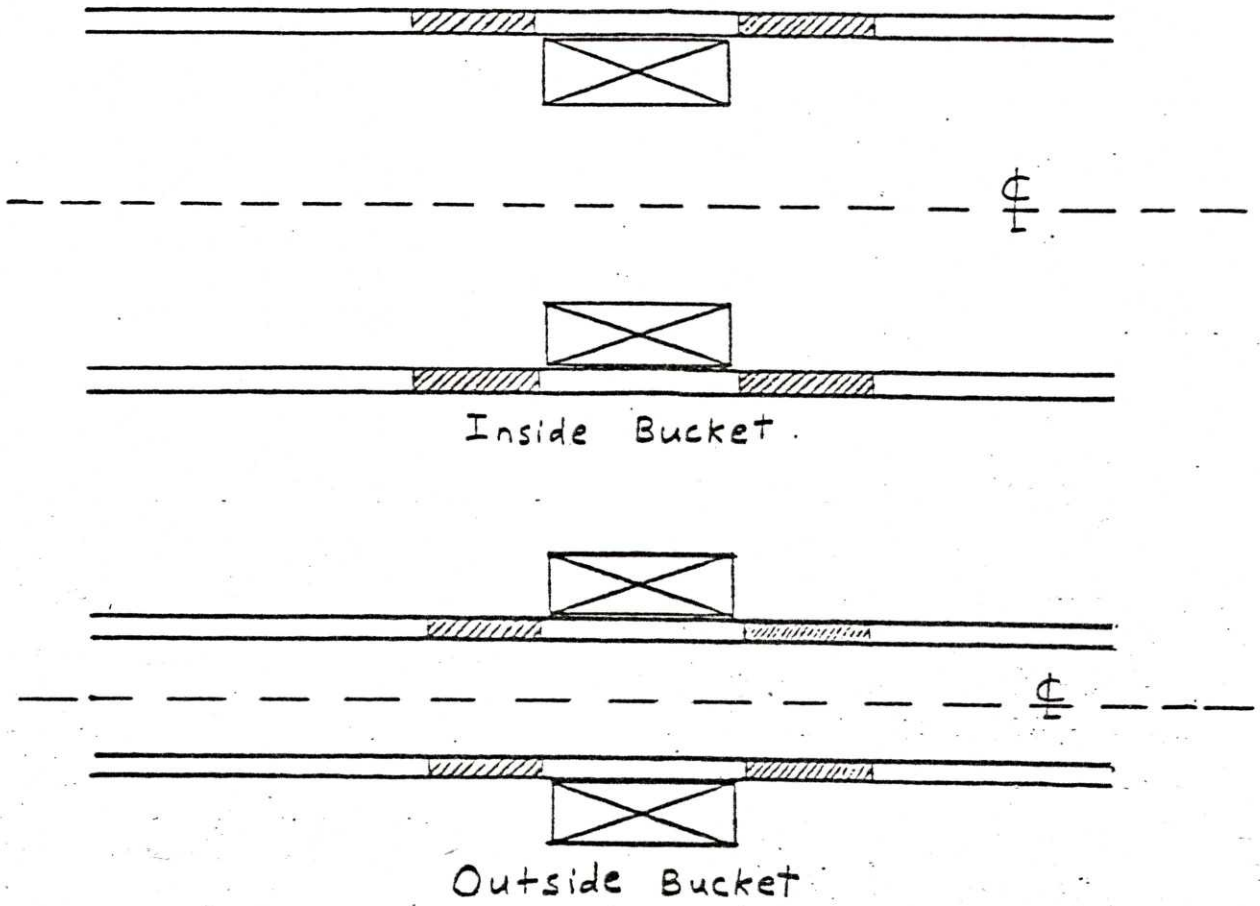
The topology of the helical rail gun is also capable of being varied quite extensively. The cross-section of the helix can be made any shape desired, with rectangular and circular cross-sections of particular interest for most applications. Also, the bucket can be made to slide over the outside of the helix (outside geometry) or on the inside of the helix (inside geometry). And finally the bucket need not completely encircle the helix. A class of buckets which do not, known as saddle buckets, are particularly useful if the load to be accelerated is a large arbitrarily shaped object such as an aircraft. These different geometries are illustrated in Figure I.3.

Helical rail guns also scale up very well to large size. In order to get more force from a particular type of helical rail gun, the following strategies may be followed: geometric scaling, where the diameter of the helix is increased, but the fixed mechanical clearances are not; boom multiplication, where multiple helices are built, and the separate buckets fixed rigidly together; and bucket multiplication, where multiple buckets are wound on a single helix and attached rigidly together. These three methods of scaling are shown in Figure I.4.

Finally, helical rail guns are very easy to deal with theoretically. Since the commutating brushes are rigidly attached to the bucket, the relative position of the drive coils with respect to the bucket coils is fixed. This reduces the problem of finding the force produced by the

Figure I.3

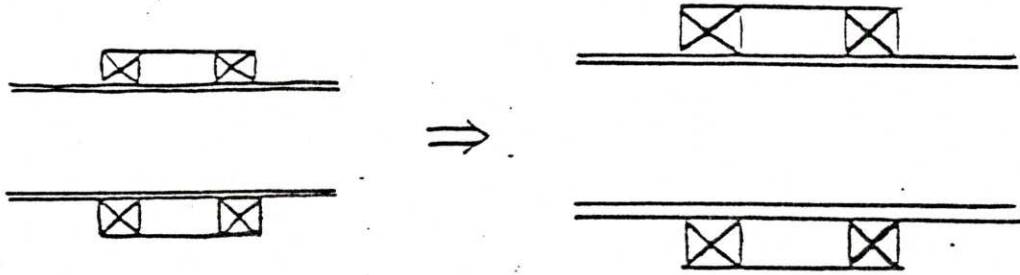
Helical Rail Gun Geometries



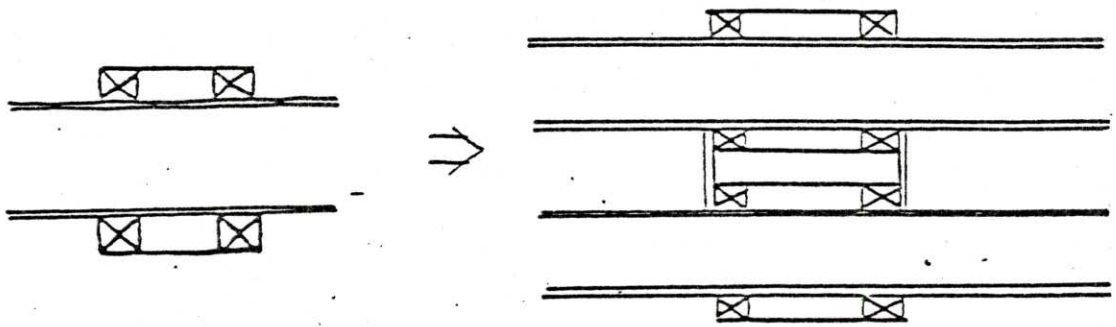
Saddle Bucket

Figure I.4

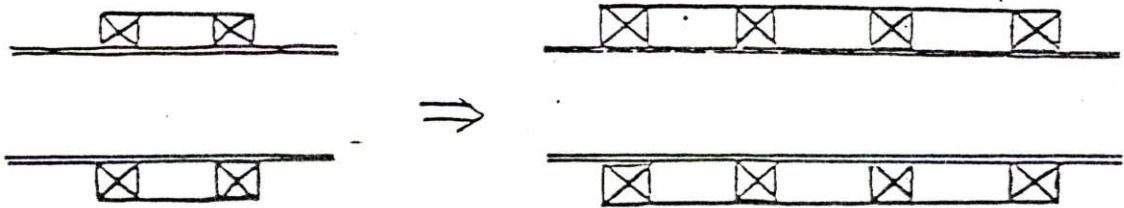
Helical Rail Gun Force Scaling



Geometric Scaling



Helix Multiplication



Bucket Multiplication

bucket to one of statics, since all questions regarding motion, timing or synchronization are eliminated. As with all electromagnetic accelerators, the force produced by a helical rail gun can be described by the mass driver equation,

$$F = N_b I_b N_d I_d dM/dz \quad I.1$$

which is derived by Mongeau. F is the force produced by the bucket, I_b and I_d are the currents which flow through the bucket and drive coils respectively, N_b and N_d are the number of turns in the bucket and drive coils, and dM/dz is the mutual inductance gradient or magnetic coupling (z is the axis along which the force is produced). Thus, in order to maximize the force, it is necessary to maximize the bucket current-turns product, the drive coil current-turns product and the magnetic coupling. In general, the amount of current which can be put through a bucket or drive coil is limited by thermal constraints, mechanical bursting constraints, or electrical constraints such as arcing. The maximum magnetic coupling which can be achieved is limited by the need to maintain fixed mechanical clearances, and by size requirements imposed by the other constraints (such as the need to maintain a certain size conductor cross-section to limit ohmic heating). The theoretical analysis of helical rail guns therefore comes down to the quantification of these limits.

There is also practical experience with helical rail guns. The Electromagnetic Acceleration Group has been engaged in research into helical rail guns for the last three years, in which time three of these have been built and tested. They are: a 1-meter long bench-top model, with a conventional outside geometry bucket; a 4-meter long transportable model glider launcher, capable of accelerating 5-kilogram radio controlled model gliders to 50 meters per second at an angle of 45 degrees; and a saddle bucket wound for use on the 1-meter bench-top helix. These devices have demonstrated the feasibility of helical rail guns.

This thesis will document the work which has been done to date by the Electromagnetic Acceleration Group on helical rail guns, and will present several applications for their use. The first part of the thesis will deal with the theory and analysis of helical rail guns, and will discuss their thermal, mechanical, and electrical limits, as well as the topics of magnetic and mechanical coupling, efficiency, and passive and active buckets. The second part of the thesis deals with the construction and testing of the three helical rail guns mentioned above, and the results of those tests. And finally, the third part of the thesis is devoted to the application of helical rail guns to real tasks. A systematized method of design for helical rail guns is given, which is then used to determine the parameters for various types of aircraft launchers. These include launching Navy aircraft from aircraft carriers, launching fully loaded

VTOL Harrier aircraft from other Navy surface combatants, launching Air Force fighters directly from armored hangars, and using helical rail guns to assist commercial airliners during take-off.

II. Theory

II.1. Elementary Limits

As stated in the introduction the central equation in helical rail gun analysis is the mass driver equation, repeated here for clarity,

$$F = N_b I_b N_d I_d dM/dz \quad \text{II.1.1}$$

For analysis of existing systems this equation allows us to determine the force generated by the bucket if the number of turns is known, the current distribution is known and the magnetic coupling is known. For any given system the number of turns is fixed, as is the magnetic coupling, which can be calculated or experimentally determined. Thus the performance of an existing system is limited by the amount of current which can be made to flow through the bucket and drive coil. There are several obvious limits to this. If a large current is maintained for a long enough time, the ensuing ohmic heating will cause a significant temperature rise which can damage the device, either through burned electrical insulation, structural weakening or even melting. Also, if very large currents are used, even for very short times, the ensuing high magnetic pressure created can cause mechanical bursting. And, if large currents are forced through the finite electrical resistance of the device, the

voltages generated can become large enough to cause arcing through the electrical insulation, destroying its effectiveness. This section will examine and quantify each of these limits (thermal, mechanical and electrical) in turn.

II.1.1 Thermal Limits

When current flows in an ohmic conductor, power is dissipated as heat throughout the volume of that conductor. Although the mechanisms of conduction, convection and radiation exist to carry heat away, convection is applicable only to fluids and radiation only becomes important at extremely elevated temperatures. Conduction is the only important heat removal mechanism which operates at low to moderate temperatures in solid conductors. Conduction, however, takes a certain amount of time to operate, and it will not have a chance to remove any significant amounts of heat if the current pulse is of sufficiently short duration. The heating is then said to be adiabatic.

The criterion for deciding whether conduction effects can be ignored is the thermal diffusion equation,

$$\frac{\partial T}{\partial t} = \frac{K}{C_v} \nabla^2 T \quad \text{II.1.1.1}$$

where T is the temperature, K is the thermal conductivity, and C_v is the specific heat per unit volume of the material. For a uniform initial temperature rise ΔT , which is allowed to decay, simple systems can be modeled as a thermal resistor in series with a thermal capacitor. The temperature decay with time is found to be exponential, having a time constant of

$$\tau_{\text{conduction}} = R_{\text{th}} C_{\text{th}} \quad \text{II.1.1.2}$$

where R_{th} is the thermal resistance and C_{th} is the thermal capacitance. The thermal resistance may be calculated simplistically as

$$R_{\text{th}} = L/(K A) \quad \text{II.1.1.3}$$

where L is the length through which the heat must flow, while A is the area of flow. In similar fashion, the thermal capacitance is calculated as

$$C_{\text{th}} = C_v V \quad \text{II.1.1.4}$$

where V is the volume of the conductor. For most geometries of interest V is approximately equal to L times A ; plugging in yields a new expression for the decay time constant

$$\tau_{\text{conduction}} = (C_v/K) L^2 \quad \text{II.1.1.5}$$

which to be meaningful should be used with L equal to the smallest characteristic dimension of the coil of interest.

To determine if conduction is a significant effect, the thermal decay time constant should be compared with the duration of the current pulse. If $\tau_{\text{conduction}}$ is much larger than the pulse length, then conduction effects will be small, and the heating should be modeled as adiabatic. If

τ conduction is much smaller than the pulse length, a steady state temperature is reached in which conduction just balances the electrical power dissipation. Since most applications involving helical rail guns have a rather short current pulse compared to their thermal time constant, adiabatic heating is the correct model to use. Because of this, and because adiabatic heating is a worst case, this thesis will deal solely with adiabatic heating, and not attempt to quantify the effects of conduction further.

For adiabatic heating due to ohmic power dissipation, the power per unit volume deposited in the conductor manifests itself as a temperature rise. This is described by

$$c_v \, dT/dt = \rho \, J^2 \quad \text{II.1.1.6}$$

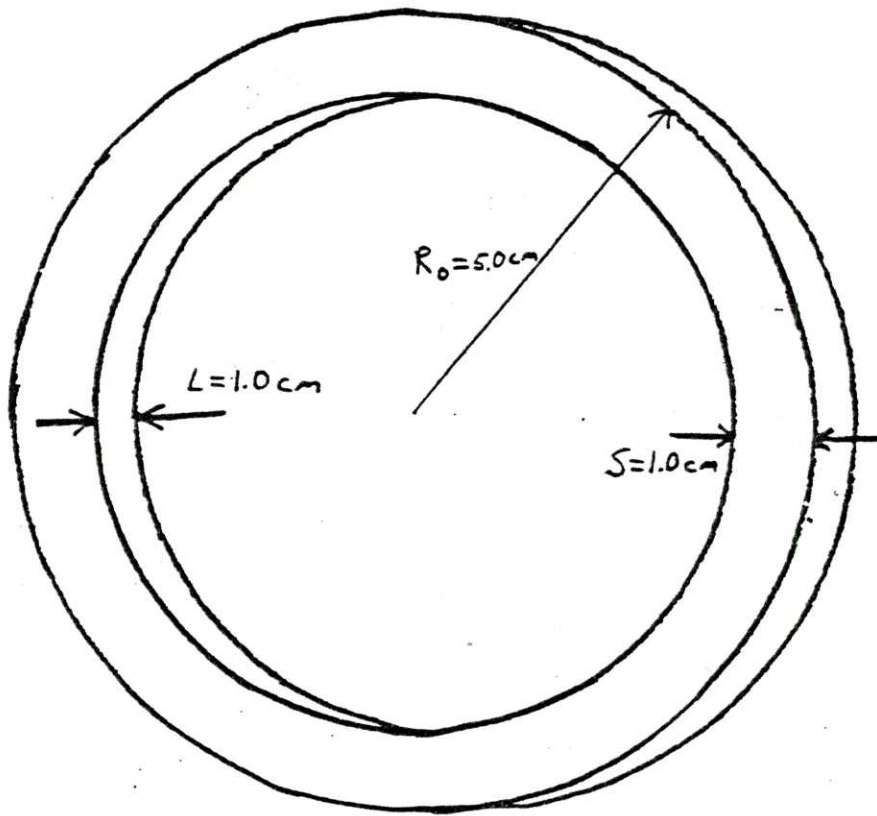
where ρ is the electrical resistivity of the conductor and J is the current density flowing. By integrating this equation, the current integral is obtained,

$$\int_0^t J^2 \, dt = \int_T^{T+\Delta T} \left(\frac{c_v}{\rho} \right) dT \quad \text{II.1.1.7}$$

Thus, if we know the current distribution, the temperature rise can be calculated; conversely, if we know the maximum temperature rise which can be tolerated, the current density can be determined.

For example, suppose that the finite build coil shown in Figure II.1.1.1 is the bucket of a helical rail gun, wound

Figure II.1.1.1



from a single turn of copper wire. If the bucket is to have a constant current applied for a duration of 0.1 seconds, but can tolerate a temperature rise of only 25°C, what is the maximum current which can be allowed to flow for this period of time? Equation II.1.1.7 becomes

$$J^2_{\max} \Delta t = \int_T^{T+\Delta T} \left(\frac{c_v}{\rho} \right) dT = \left(\frac{c_v}{\rho} \right) \Delta T \quad \text{II.1.1.8}$$

where the first equality holds by the assumption of constant current, and where the second equality holds since the specific heat and resistivity stay relatively constant with the small temperature change. If this had not been the case, tables and graphs giving the current integral for different materials and different initial and final temperatures could have been used to give a more accurate answer.

For the case of copper at room temperature the specific heat and resistivity are $c_v = 3.4 \text{ J/cm}^3$ and $\rho = 1.7 \text{ micro-ohm cm}$. Thus solving the problem yields $J = 22 \text{ kilo-amps/cm}^2$. Since the coil build is 1 cm on a side, the maximum current which can flow is $I = 22,000 \text{ amps}$.

II.1.2. Mechanical Limits

The circular geometry bucket illustrated in Figure II.1.1.1 is also limited in the amount of current which can be put through it by mechanical constraints. From the Lorentz force law,

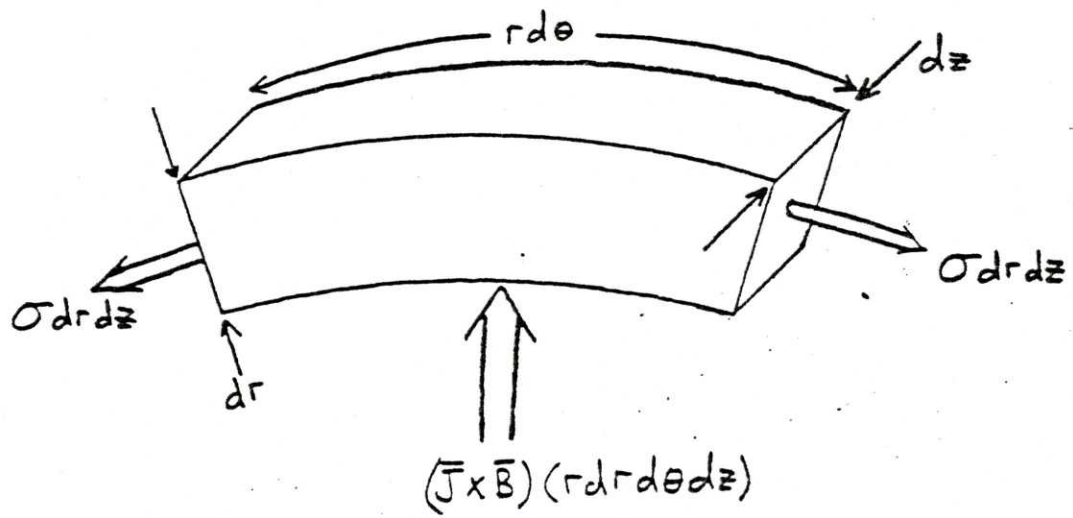
$$\vec{f} = \vec{J} \times \vec{B} \quad \text{II.1.2.1}$$

where \vec{f} is the force per unit volume, \vec{J} is the current density and \vec{B} is the magnetic field. For the material of the coil to be in static equilibrium, this magnetic force must be balanced by the stress in the material. Figure II.1.2.1 shows a differential element of the coil being acted on by these stresses. This element is presumed to be isolated from the other elements around it, although in actuality a real differential element in the coil would react with its neighbors through radial stresses, which have been neglected in the figure. For the forces to be in balance, the tangential stress in the material, σ_t , must be

$$\sigma_t = J B r \quad \text{II.1.2.2}$$

This magnetically induced stress can then be compared with the yield stress in the material to determine if the coil will deform under static (or long-acting) forces.

Figure II.1.2.1
Differential Stress Element



Since we are trying to determine the limit to the amount of current which can be put through our coil, we need to find the magnetic field acting on the conductor. Although there are accurate computer codes available to determine the magnetic field of an arbitrary configuration of current carrying conductors, this approach is far more complicated than necessary for an initial analysis. What we would like to have are simple analytic expressions, and there are two approximations which provide just that: the coil may be modeled as an infinite straight wire; or the coil may be modeled as an infinite solenoid. Of the two, the infinite solenoid model is the more important, since its predicted magnetic field will always be greater than the actual field generated by a coil of finite build. It is therefore a worst case assumption. The infinite straight wire approximation will be given here for completeness, but no further analysis will be done using it. This approximation is sometimes useful when the build and length of a coil are very much less than the radius of curvature, that is when the coil is very thin radially and very short axially. Since calculation of the field at any point around a wire of arbitrary cross-section is an involved task, and since we are only interested in an approximate value anyway, the following method of calculation may be used: for a coil with a rectangular cross-section, of axial length L and radial thickness S , first approximate the current density flowing in the coil as a current filament of value $I = J L S$; then

use Ampere's law to obtain the magnetic field at the inner surface of the coil as

$$B = \mu J L / \pi \quad \text{II.1.2.3}$$

where μ is the magnetic permeability, and where the distance from the current filament to the inside surface of the coil has been taken as $S/2$.

For an infinite solenoid, with the same build (radial thickness) as the finite coil of interest, the magnetic field at all points inside is

$$B = \mu J S \quad \text{II.1.2.4}$$

where S is the build of the coil. The magnetic field then falls off through the build of the infinite solenoid to zero outside.

To find the largest stress generated in the material, the magnetic field just calculated in Equation II.1.2.4 can now be substituted into Equation II.1.2.2, yielding

$$\sigma_{tmax} = \mu J^2 S R \quad \text{II.1.2.5}$$

where R would normally be chosen as the outside radius of the coil. This equation assumes that the current density is constant throughout the build of the coil and that the total magnetic field is due to the coil's self field. If additional external fields are also present, the above

equation should be modified accordingly.

The previous method of analysis assumed that the radial stresses generated between the windings of a coil could be safely ignored. For circular coils in which the radial thickness of the build is smaller than the inside radius, this is indeed a good assumption, and the stress calculated above will actually be a maximum. However, if the radial thickness is greater than the inside radius, or if a more accurate analysis is desired, it is possible to include the radial stresses and still obtain an analytical answer.

If radial stresses are included, Equation II.1.2.2 must be modified to become

$$\sigma_t - d(r \sigma_r) / dr = J B r \quad \text{II.1.2.6}$$

and the radial and tangential stresses can then be determined using the method of displacements as described by Montgomery. The shear stress is

$$\sigma_s = (\sigma_t - \sigma_r) / 2 \quad \text{II.1.2.7}$$

Finally, the maximum values of these stresses can be compared with the tensile yield stress and shear yield stress to determine whether the coil of interest is mechanically limited and should be reinforced.

The analysis of the mechanical limits of rectangular geometry coils is similar in style to the analysis of

circular geometries, just completed. A rectangular helix, for example, typically consists of windings of conductor epoxied to a strong substrate. Therefore these windings could be modeled as unsupported segments of conductor held in place against the magnetic pressure by the stress in the epoxy alone; failure would be assumed to occur if the magnetic pressure exceeded the epoxy bond strength. Alternatively, a rectangular coil may be modeled as four beams, each rigidly clamped at both ends (at the corners of the rectangle), and each loaded along its length by the magnetic pressure. The maximum tensile and shear stresses will then occur at the ends of the beams, which for beams of rectangular cross-section are given by

$$\sigma_{tmax} = 1/2 (W/L) (D/S)^2 \quad \text{II.1.2.8}$$

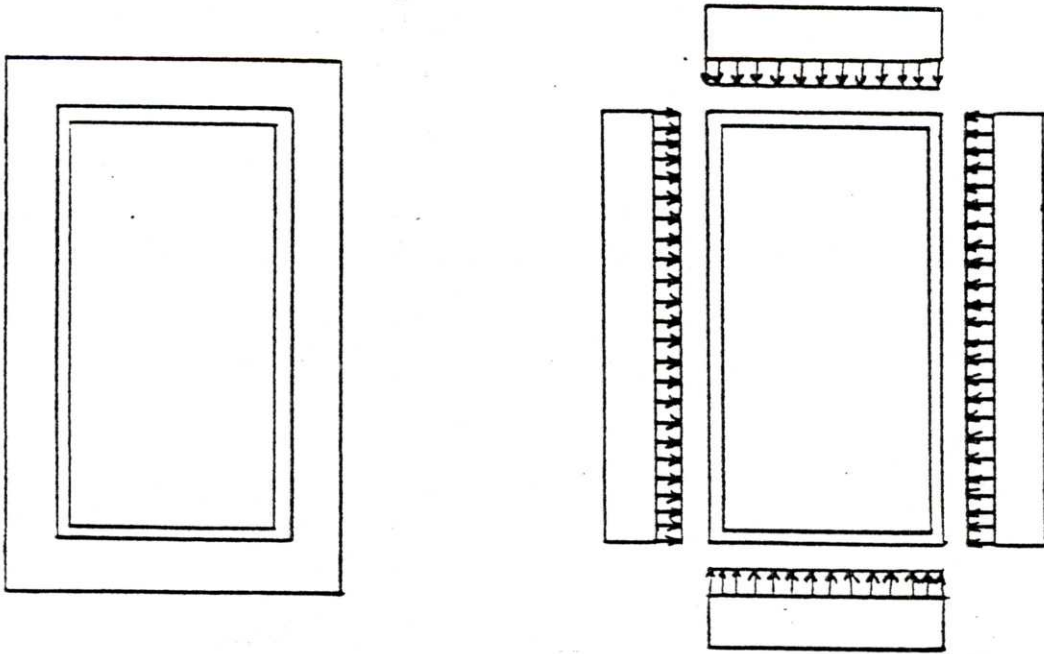
and

$$\sigma_{smax} = 3/4 (W/L) (D/S) \quad \text{II.1.2.9}$$

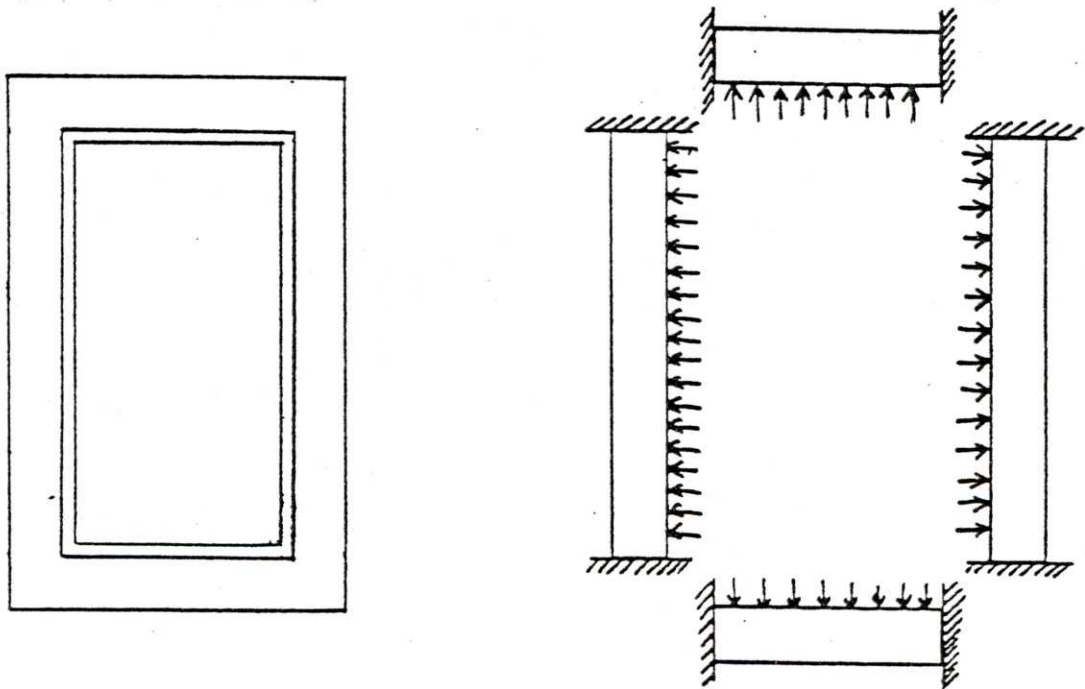
where W is the force per unit length being applied to the beam, L is the axial length of the coil, which is also the beam width, S is the transverse depth of the windings or beam height, and D is the length of the beam, which will be the length of the side under analysis. Figure II.1.2.2 illustrates both of these methods of analysis.

Finally, to determine the mechanical limits of a rectangular saddle coil, the fully supported top side should

Figure II.1.2.2



Epoxy Bond Strength Method



Fixed End Beams Method

be modeled as the clamped beam just analysed, and the two sides should be modeled as cantilevered beams, possibly with rolling supports at their free ends. Again they are assumed to be loaded along their length by the magnetic pressure. For an unsupported cantilevered rectangular beam, both the maximum tensile stress and the maximum shear stress occur at the clamped end. They are

$$\sigma_{tmax} = 3 (W/L) (D/S)^2 \quad \text{II.1.2.10}$$

and

$$\sigma_{smax} = 3/2 (W/L) (D/S) \quad \text{II.1.2.11}$$

For a supported cantilevered rectangular beam, the maximum tensile stress occurs 5/8 of the distance from the clamped end to the supported end and is

$$\sigma_{tmax} = 27/64 (W/L) (D/S)^2 \quad \text{II.1.2.12}$$

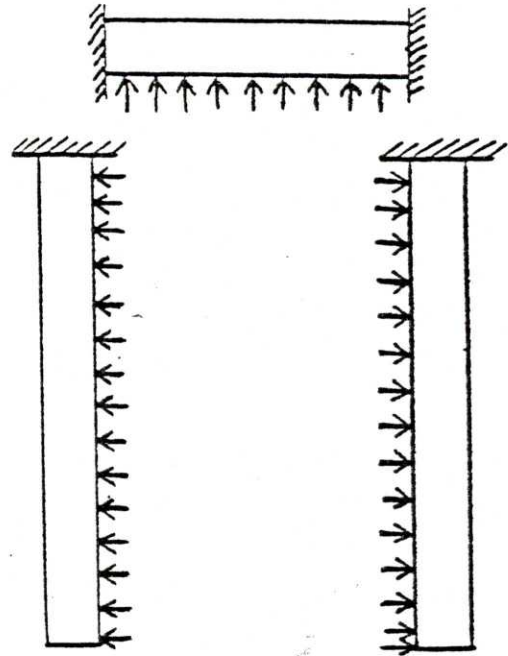
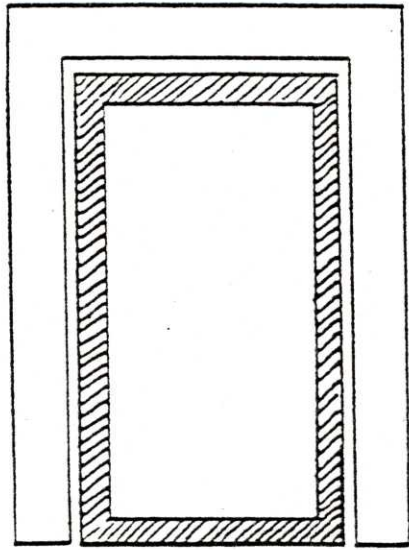
while the maximum shear stress occurs at the clamped end and is

$$\sigma_{smax} = 15/16 (W/L) (D/S) \quad \text{II.1.2.13}$$

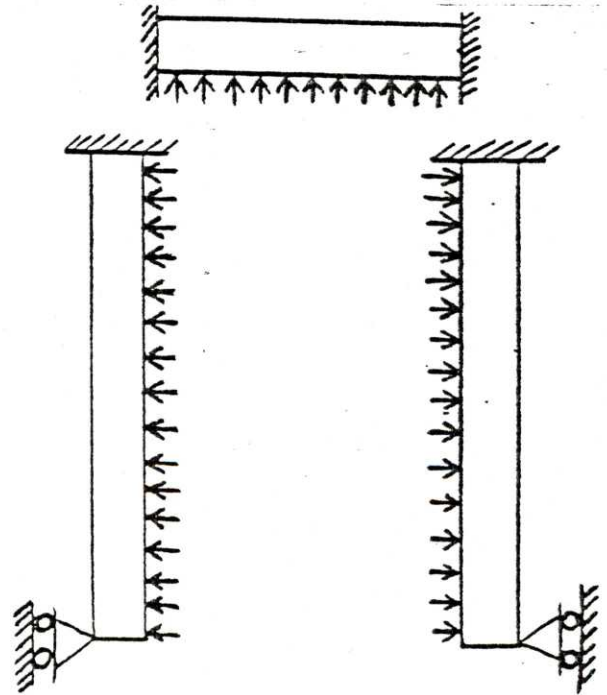
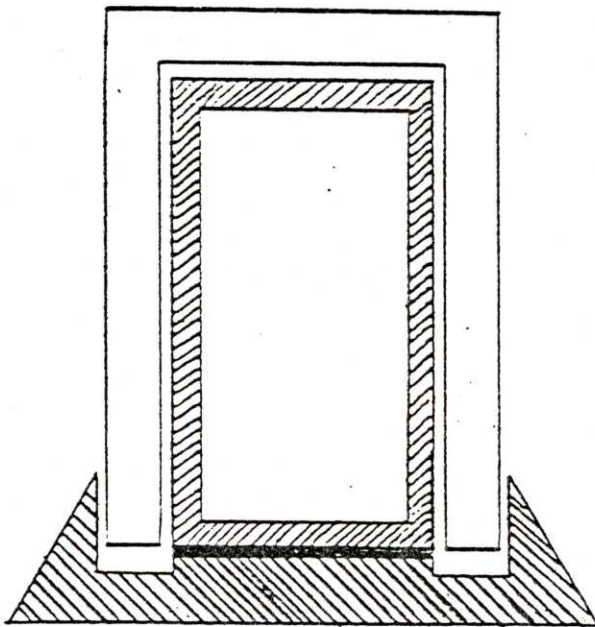
Both of these configurations are shown in Figure II.1.2.3.

To summarize, the following approach should be used when dealing with the mechanical limits of helical railguns.

Figure II.1.2.3



Cantilevered Beams



Supported Cantilevered Beams

First, the worst case magnetically should be chosen for each component involved. Second, using worst case quantities as in Equation II.1.2.5, and simplified analysis, the current density which is guaranteed to keep the stress in the windings below the yield stress of the material should be determined. And third, only if a more detailed analysis is then called for should a more complicated model be used.

This approach is valid because helical rail guns are generally limited by thermal heating rather than mechanical bursting. Thermal heating grows as J^2t , while mechanical stress only grows as J^2 ; since helical rail guns typically operate for much longer periods of time than other electromagnetic accelerators they tend to be thermally limited. Also, coils can have their mechanical bursting pressure increased by adding external reinforcement, something which cannot be done for the thermal limit if the heating in the windings is adiabatic. For an example of the difference in magnitude between mechanical bursting limits and thermal heating limits, consider the bucket coil used to illustrate thermal heating (see Figure II.1.1.1). For a pulse lasting 0.1 seconds, the current was limited to 22,000 amps for a temperature rise of 25°C. This same coil has an unreinforced mechanical bursting current limit of 33,330 amps, assuming a soft copper yield stress of only 6.98×10^7 N/m² (10,000 psi). In the designs considered later, this difference is even more graphic, as the pulse lengths used are typically several seconds.

II.1.3. Electrical Limits

The current which can be put through helical rail guns is also limited by electrical considerations. On the time scale of helical rail guns, that limit is Ohm's law, since inductive effects are negligible, and since voltage appears across a conductor with current flowing in it due to the finite resistance of the conductor (superconductors being highly impractical for use in helical rail guns). If the voltage generated becomes high enough, the current will arc, flowing through paths not planned for it and almost certainly damaging the device. This is generic to all electromagnetic accelerators. There is however a limit which is particular to helical rail guns, and which is a consequence of their basic design. This is the surface heating of the commutating brushes, and the generation of arcs if the brush current density is pushed too high.

There are three mechanisms for brush heating: bulk ohmic heating, surface electrical power dissipation, and frictional surface heating. Calculation of the bulk ohmic heating is straight-forward. The temperature rise throughout the volume of the brush can be calculated using Equation II.1.1.7 and is

$$\Delta T = \left(\frac{\rho_{br}}{C v_{br}} \right) \int_0^t J_{br}^2 dt = \left(\frac{\rho_{br}}{C v_{br}} \right) J_{br}^2 t \quad \text{II.1.3.1}$$

where ρ_{br} is the bulk resistivity of the brush, and C_{vbr} is the specific heat per unit volume of the brush. The second equality holds if the brush current density, J_{br} , is reasonably constant over the length of the pulse.

The next two brush heating mechanisms, surface electrical power dissipation and frictional heating, involve the diffusion of heat from the sliding surface into the bulk of the brush material. Electrical power dissipation on the surface of the brush is caused whenever the brush carries current. A potential difference, V , is then generated across the brush/conductor interface (typically 1 to 2 volts unless gross arcing develops) which, when multiplied by the current density flowing in the brush, J_{br} , yields the surface electrical power dissipation. Frictional heating occurs because the brushes resist being dragged along the rough surface of the helix. The power flux generated in this case is just the frictional force of the brushes, F_b , multiplied by the brush velocity, v , divided by the total brush area, A_{br} . The total thermal power flux at the interface is then

$$J_{th} = (V J_{br} + (F_b v) / A_{br}) / 2 \quad \text{II.1.3.2}$$

which has been divided by two since half of the power generated can be expected to wind up in the brush and half in the helix. This thermal power flux then diffuses into the bulk of the material according to the thermal diffusion equation

$$\frac{\partial T}{\partial t} = \left(\frac{K_{br}}{C_{vbr}} \right) \nabla^2 T$$

II.1.3.3

with the necessary boundary condition

$$\vec{J}_{th} = K_{br} \vec{\nabla} T$$

II.1.3.4

where K_{br} is the thermal conductivity of the brush material and C_{vbr} is the brush specific heat per unit volume. If the brush is now modeled as a semi-infinite slab, the highest temperature will be found on the surface where the heating is applied. This temperature will then increase with time according to the relation

$$\Delta T_{surf} = \frac{2}{\sqrt{\pi}} \sqrt{\left(\frac{J_{th}^2 t}{K_{br} C_{vbr}} \right)}$$

II.1.3.5

assuming the thermal power density is relatively constant with time. Figure II.1.3.1 shows this surface heating, where X is distance into the bulk of the brush, and t is time.

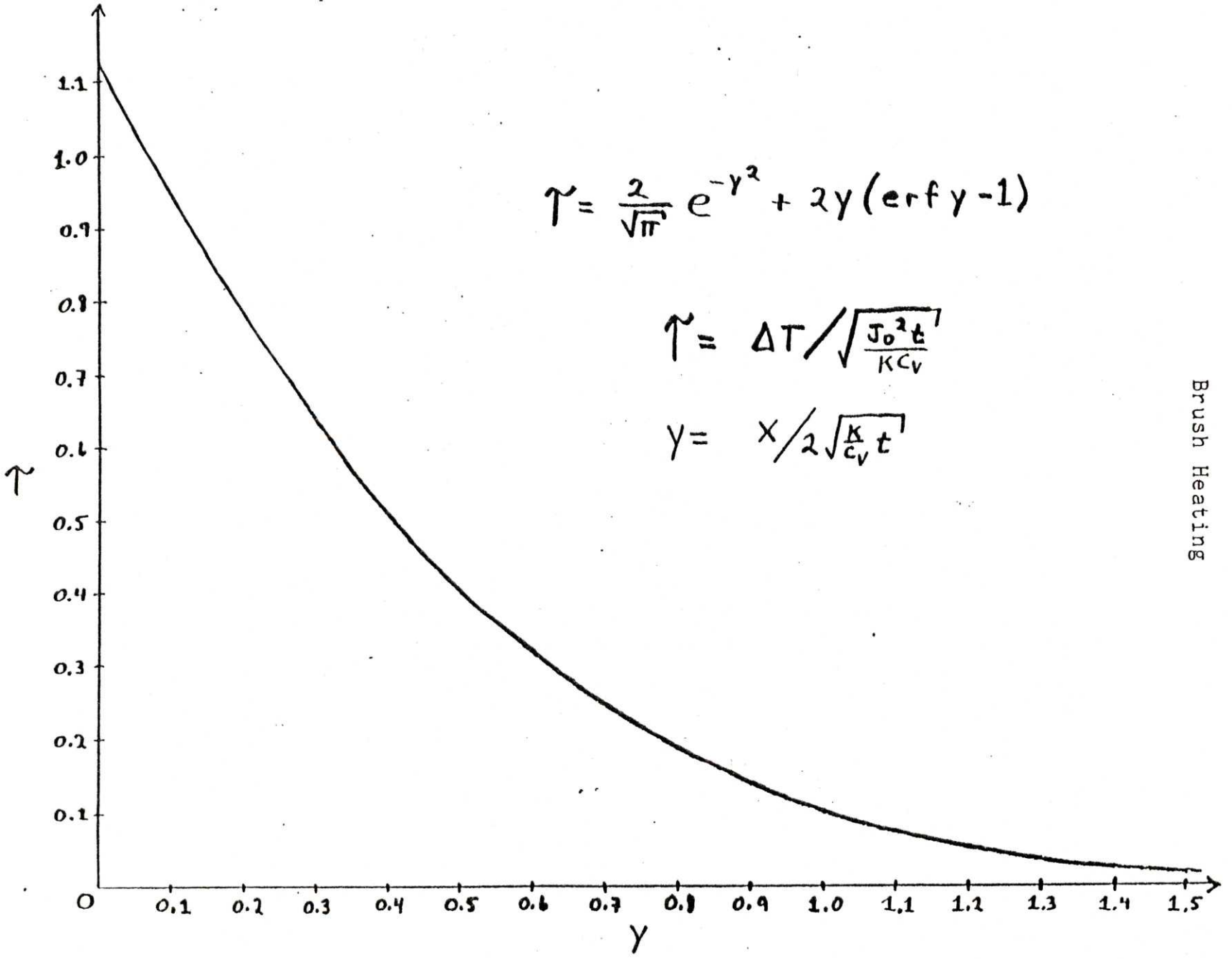
Both of the above heating mechanisms (bulk and surface) apply equally well to either the commutating helix brushes or the sliding feed-rail brushes. The large temperature increases at the surface of the brush soften the brush material and lead to greatly increased rates of frictional wear, thereby causing drastically decreased brush life. This is especially true for the helix brushes, since the helix is often much rougher than the feed-rails, and since the current densities are higher.

Figure II.1.3.1
Brush Heating

$$\gamma = \frac{2}{\sqrt{\pi}} e^{-\gamma^2} + 2\gamma(\operatorname{erf} \gamma - 1)$$

$$\gamma = \Delta T / \sqrt{\frac{J_0^2 t}{K C_V}}$$

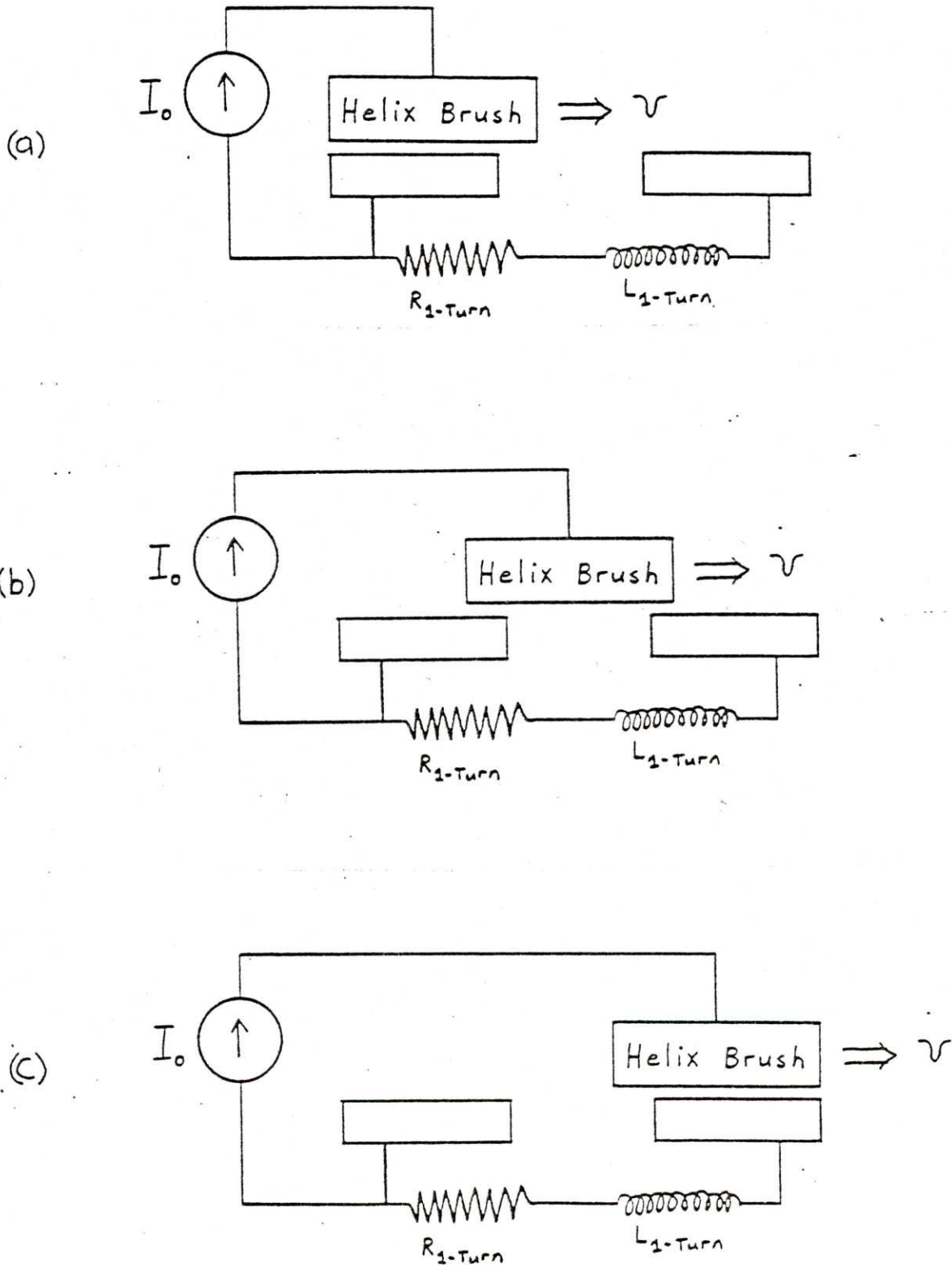
$$\gamma = x / 2 \sqrt{\frac{K}{C_V t}}$$



Commutating helix brush arcing is another phenomenon which can seriously degrade helical rail gun performance and lead to increased rates of brush wear. The commutating helix brushes have the job of energizing new turns of the drive coil and de-energizing old turns as the bucket moves down the length of the helix, in order to maintain the constant position of the drive coil relative to the bucket. There are three distinct phases to this process, illustrated in Figure II.1.3.2. In (a) the leading and trailing brushes are fully on the turns they are about to leave, providing current to those turns. For the case of the leading brush, this is the the turn which has just been energized, and for the case of the trailing brush, this is the turn which is about to be de-energized. In (b) both the leading and trailing brushes have partially left their old turns and have bridged the gap to their new turns. Finally in (c), the leading and trailing brushes are fully on their new turns, having completed a full cycle of commutation. Two models of how this is accomplished will now be examined.

The first model of brush commutation makes the explicit assumption that the current density flowing through the sliding surface of the brush is constant. Thus, as the brush slides along from the old turn to the new turn, the current is ramped up linearly from zero to the full value in the leading turn, and ramped down linearly from the full value to zero in the trailing turn. Making this assumption allows us to calculate the voltage difference, ΔV , which would be

Figure II.1.3.2
Brush Commutation



measured in the vicinity of the commutating brush,

$$\Delta V = L_{1\text{turn}} \frac{dI}{dt} + R_{1\text{turn}} I \quad \text{II.1.3.6}$$

where $L_{1\text{turn}}$ and $R_{1\text{turn}}$ are the inductance and resistance of the turn being ramped up or down, and I is the time varying current. The current through the new turn being energized in front is

$$I_{\text{leading}} = I_0 (v/d) t \quad \text{II.1.3.7}$$

while the current through the turn being de-energized in back is

$$I_{\text{trailing}} = I_0 [1 - (v/d) t] \quad \text{II.1.3.8}$$

In both cases v is the velocity of the bucket, and therefore of the brushes, d is the width of a turn on the helix, also assumed to be the thickness of a brush, and I_0 is the current flowing in the drive coil, assumed to be constant. Since a commutation cycle occurs every time a brush wipes across a full turn of the helix, t can vary from zero to d/v , corresponding to the brush just beginning to leave its old turn to the brush fully on the new turn. We are interested in the voltage difference produced when the brush leaves the old turn, since this is when the arcing occurs. Plugging in yields a turn to turn voltage drop of

$$\Delta V_{\text{leading}} = I_0 [L_{1\text{turn}} (v/d) + R_{1\text{turn}}] \quad \text{II.1.3.9}$$

and

$$\Delta V_{\text{trailing}} = -I_0 [L_{1\text{turn}} (v/d)] \quad \text{II.1.3.10}$$

where the trailing voltage drop is negative due to the convention that positive voltage drops are measured from the leading side to the trailing side. These voltage drops steadily increase with both the amount of current flowing through the brush, and the speed of the bucket, and they quickly become large enough to cause substantial arcing.

This whole model, of course, is based on the assumption stated earlier that the brush carries a constant uniform current density. By Ohm's law this implies that the voltage is constant in horizontal planes throughout the body of the brush, a condition that continues down to the sliding surface. But the sliding surface of the brush is assumed to be in metal to metal contact with the turns of the helix, between which a voltage was just calculated. Thus the predictions of the model are inconsistent with its assumptions. This does not mean, however, that the model is without value. For example, if the brush were very resistive fairly high turn to turn voltages could be sustained under the model, since they would generate only moderate cross-brush currents and affect the assumption of uniform current density very little. This model also applies if the brush is

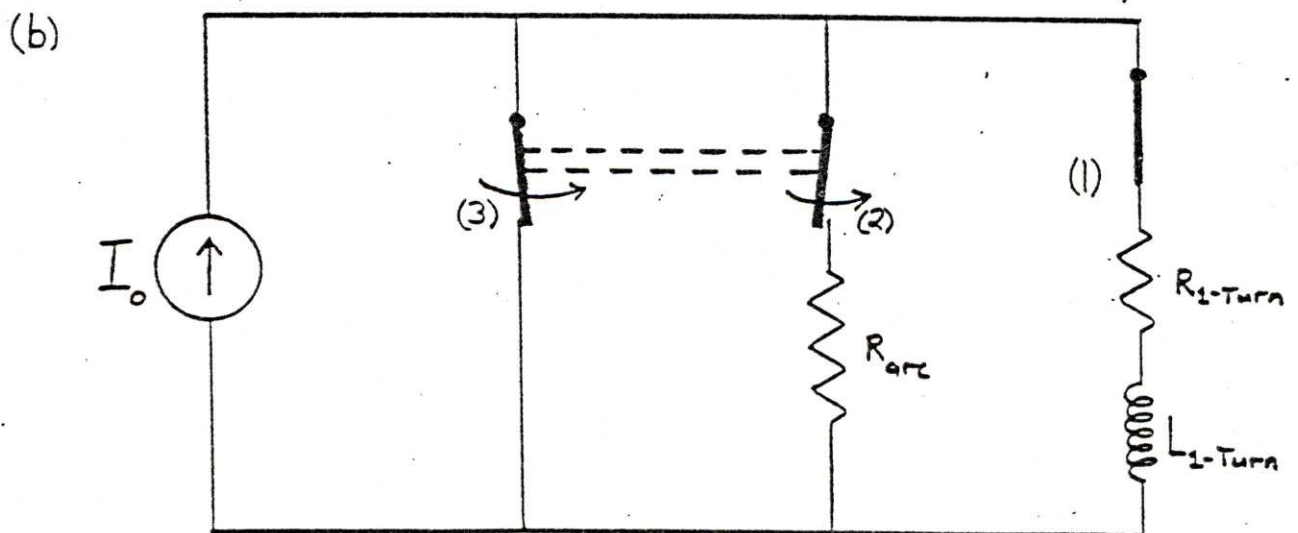
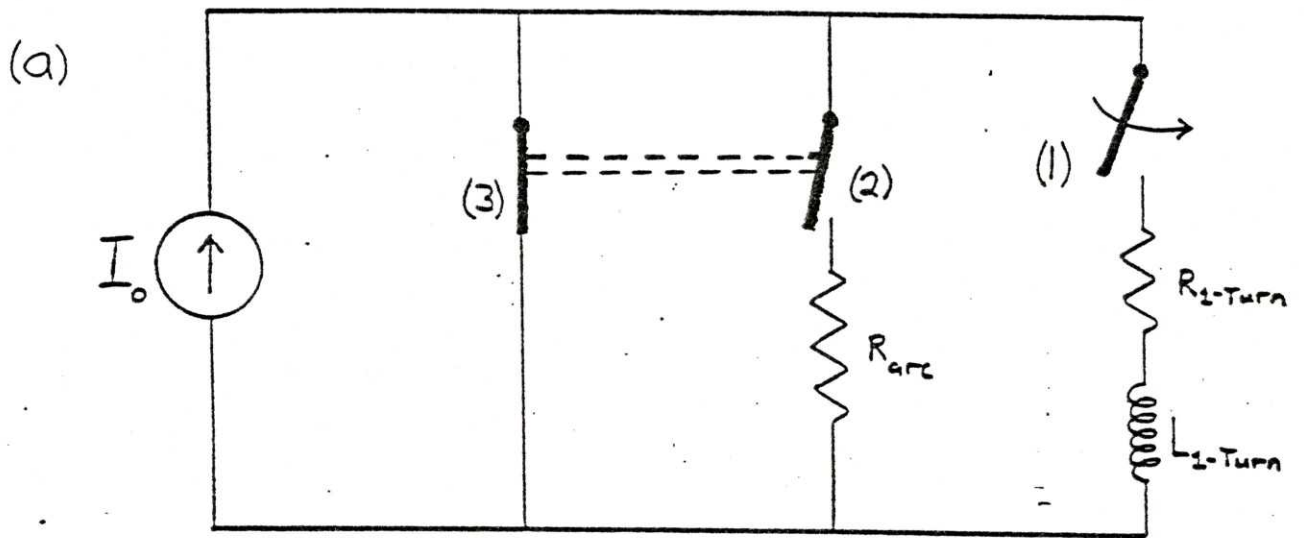
not so resistive, but the turn to turn voltages generated are low due to low speed or low current levels. Thus, at low speeds, low current levels, or high brush resistance this model is not too inconsistent and can probably be used to predict the onset of arcing.

The second model takes the other extreme, by explicitly assuming that the voltage on the sliding surface of the brush is constant. Then, as the leading brush bridges the gap between the old and new turns, there is no voltage difference to drive current into the new turn. Thus the full drive coil current, I_0 , continues to flow directly into the old turn through the diminishing contact area until contact is broken. The situation is similar in the trailing brush. There, as the trailing brush bridges the gap between the old turn and the new turn, the turn to be de-energized is crowbarred by the brush while the full drive coil current flows directly into the brush from the new turn, through the increasing contact area. The effect of crowbarring the trailing turn is that the current decays exponentially for the length of the commutation time, d/v , with a time constant of $L_{1\text{turn}}/R_{1\text{turn}}$.

As the two brushes leave physical contact with their old turns, arcs form since energized inductive circuits are being opened. If these arcs can be successfully modeled as having a constant resistance, R_{arc} , then their behavior can be analysed. Figure II.1.3.3 shows the equivalent circuit model for the leading brush arc. In (a), the leading brush

Figure II.1.3.3

Equivalent Circuit Model for the Leading Brush Arc



shorting the old and new turns is indicated by the closing of switch 1. And in (b), the leading brush leaving the old turn and forming an arc to maintain a continuous current is indicated by the simultaneous closing of switch 2 and the opening of switch 3. If $t = 0$ is taken to be the point in time when the brush leaves the old turn, then the current flowing through the leading brush arc is described by

$$I_{\text{leading-arc}} = I_0 \left\{ 1 - \left(\frac{R_{\text{arc}}}{R_{\text{arc}} + R_{1\text{-turn}}} \right) \left[1 - e^{-\frac{(R_{1\text{-turn}} + R_{\text{arc}})t}{L_{1\text{-turn}}}} \right] \right\} \quad \text{II.1.3.11}$$

which decays to the finite value of $I_0 \left[\frac{R_{1\text{-turn}}}{R_{\text{arc}} + R_{1\text{-turn}}} \right]$ rather than zero as time increases.

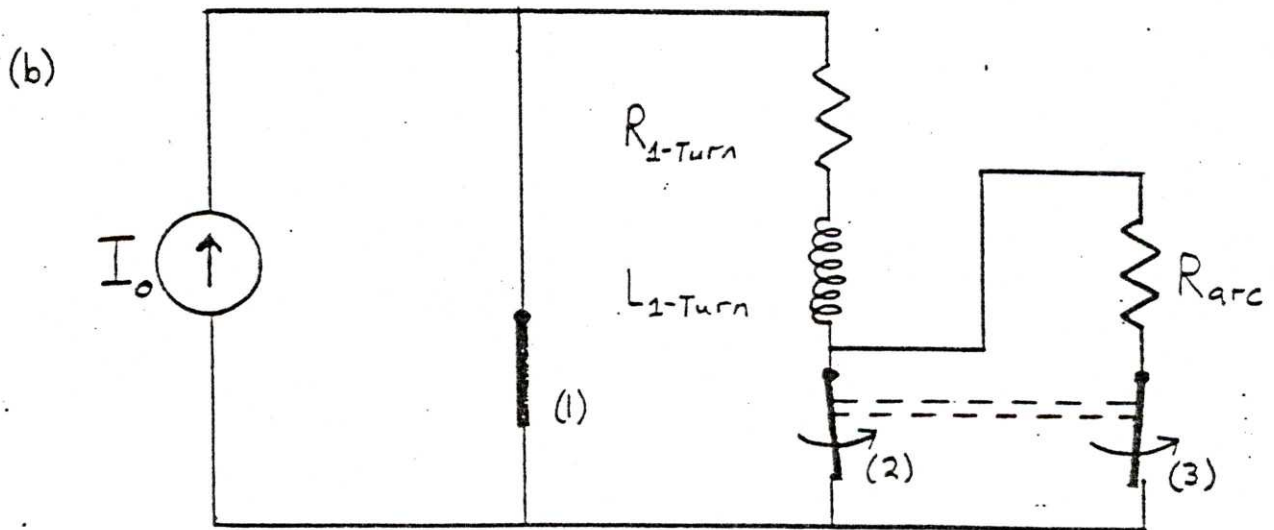
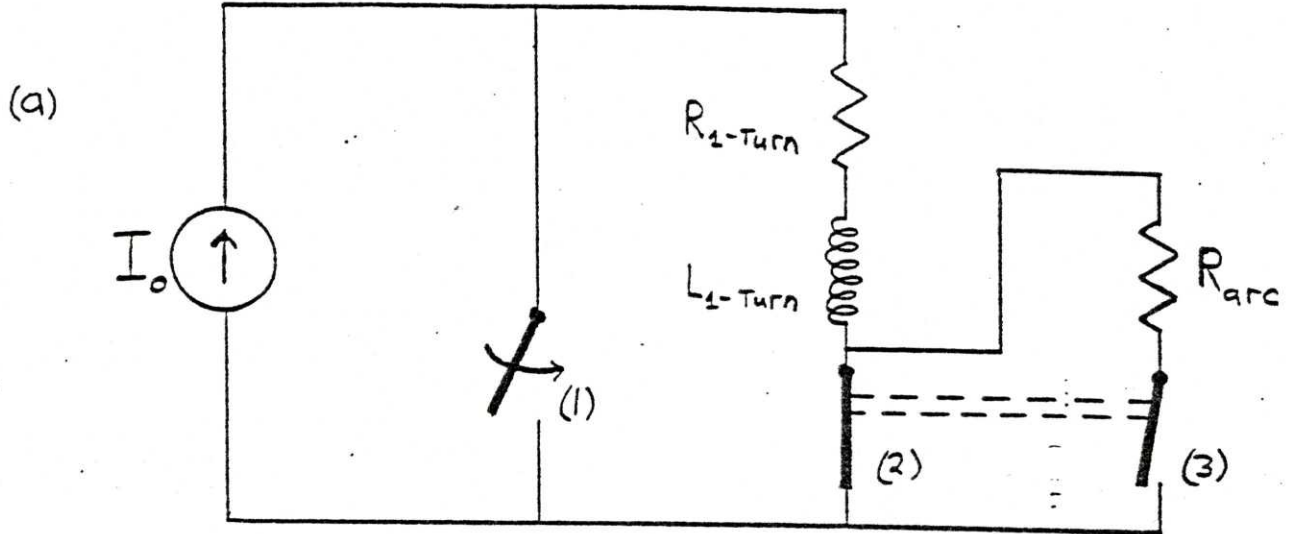
Figure II.1.3.4 shows the equivalent circuit model for the trailing brush arc. In (a), the shorting of the old and new turns by the trailing brush is indicated by the closing of switch 1, and in (b) the formation of an arc as the trailing brush leaves the old turn is indicated by the simultaneous opening of switch 2 and closing of switch 3. After its formation the current in the trailing arc decays exponentially according to the formula

$$I_{\text{trailing-arc}} = I_0 \left(e^{-\frac{d R_{1\text{-turn}}}{v L_{1\text{-turn}}}} \right) e^{-\frac{(R_{1\text{-turn}} + R_{\text{arc}})t}{L_{1\text{-turn}}}} \quad \text{II.1.3.12}$$

This model of helix commutation predicts that arcing will always occur, and that it will never cut off, although it will decrease in intensity. Both of these predictions are consequences of the assumptions made by the model, in the

Figure II.1.3.4

Equivalent Circuit Model for the Trailing Brush Arc



first case the assumption that the voltage is constant on the surface of the brush, and in the second case the constant resistance model of the arc. By Ohm's law, a constant voltage across the sliding surface of the brush is incompatible with the predicted non-uniform current distribution inside the brush, unless the brush is a perfect conductor. Again, this does not mean that the model does not have value. If the brush is a good conductor, or if the turn being wiped in or out of the circuit is very inductive (that is has a high $L \frac{dI}{dt}$), the voltages produced on the sliding surface of the brush may be enough to maintain a non-uniform current distribution. Then the model may have predictive power, especially in the high speed, high current or high conductivity regimes. The other prediction, that the arcs will decay rather than sharply cut off, is a consequence of the assumption of a constant arc resistance. Since arcs are so highly non-linear this prediction is of limited usefulness at best.

In both models of helix commutation thus far considered, rather severe helix brush arcing is predicted, at least beyond a certain value of brush current or speed, and this has been confirmed experimentally. The question then arises of whether it is possible to suppress this arcing, since it is so destructive to the brushes and causes such a marked decrease in performance. One scheme to accomplish this has been examined theoretically and will be presented here.

Although neither model of helix commutation is completely

applicable in all regimes of speed and current, they both admit to the same worst case. That is, both models predict that helix arcing will be most severe if the brushes are instantaneously moved from their old turns to their new turns. This is also intuitively reasonable. Thus, if helix arcing can be suppressed in this worst case, then the same scheme should work for more benign cases.

Figure II.1.3.5 illustrates a brush arrangement which should do just that. The front brush is directly connected to the main current carrying lead, just as before, and if the bucket were stationary this brush would continuously carry the full drive coil current. The rear brush is mechanically attached to the front brush, but electrically insulated from it; it is connected to the main current carrying lead, and therefore to the front brush, by the capacitor, C , and resistor, R_x . The capacitor is exactly analogous to the condensers used to suppress arcing in the points of an automobile ignition system; it absorbs the excess voltage produced in commutation, giving the forward current carrying brush time to leave the old turn. The resistor then tunes the time response of the circuit. In leading brushes the voltage absorbed by the capacitor is used to ramp up the new turn to full current, while in trailing brushes the voltage is used to ramp the current in the old turn down to zero. Figure II.1.3.6 shows the equivalent circuit for this configuration, where (a) shows the leading brush case and (b) shows the trailing brush case. The choice of the two variable circuit parameters C

Figure II.1.3.5

Capacitive Brush

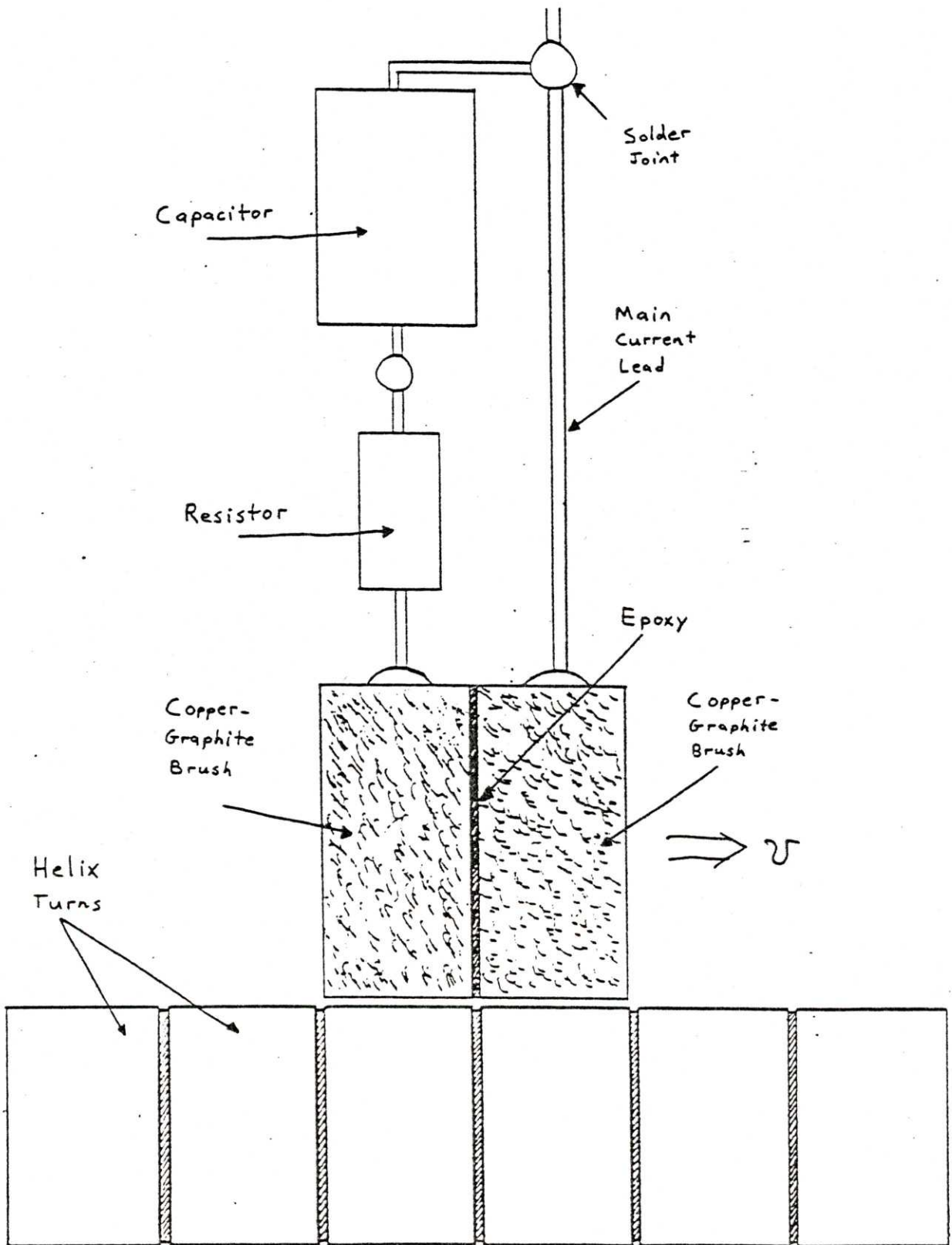
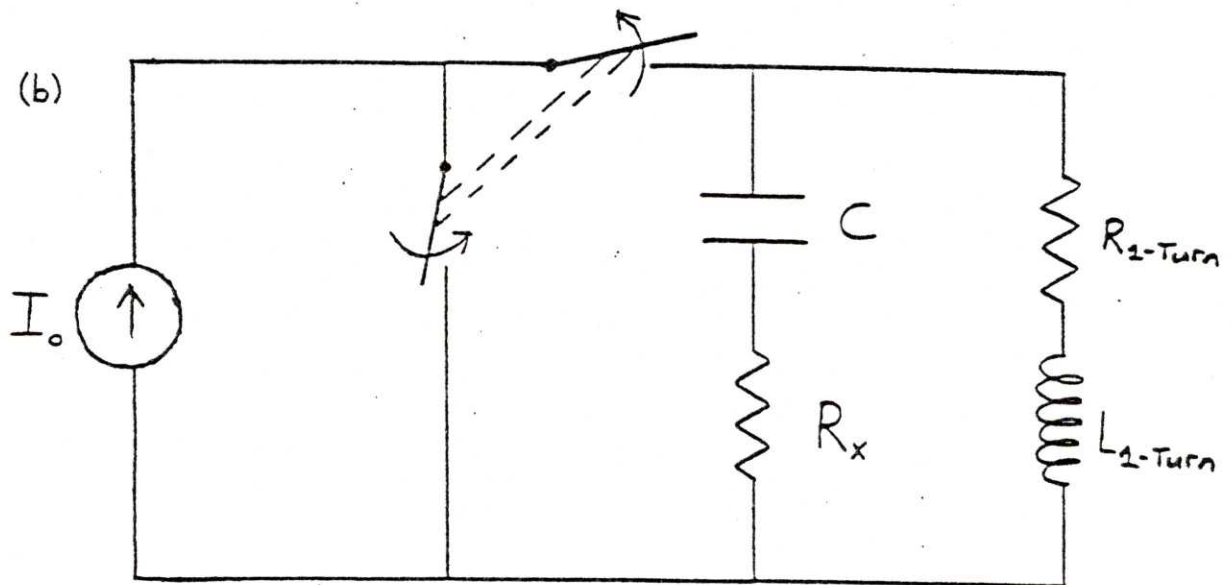
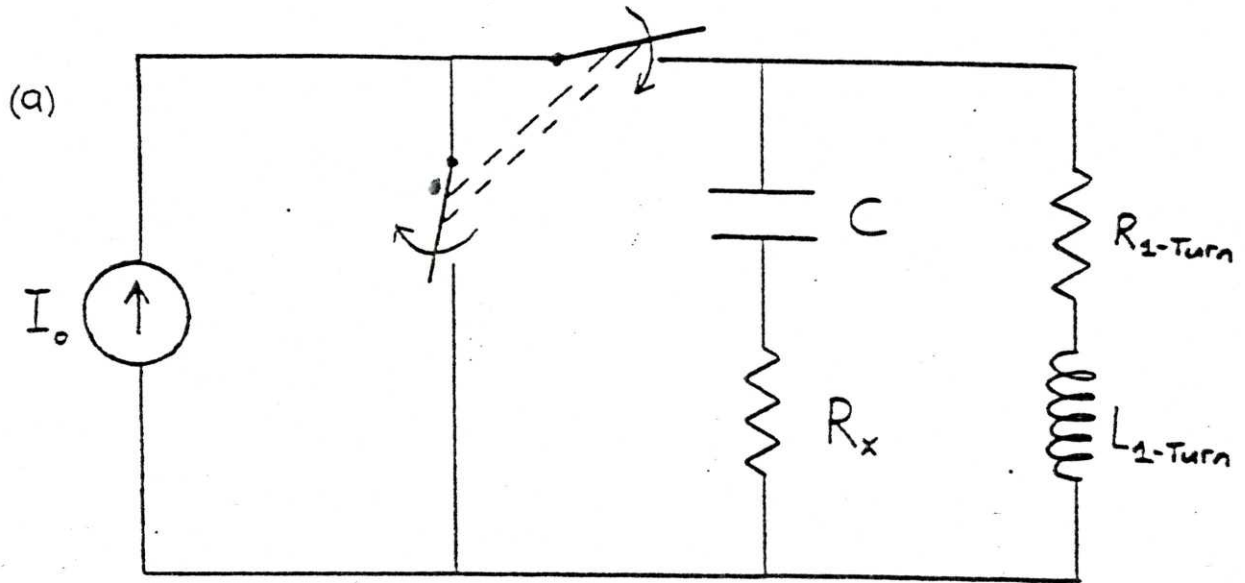


Figure II.1.3.6

Capacitive Brush Equivalent Circuit Model



and R_x will be the same in both cases and is governed by the need to achieve critical damping, and to bring the current to steady state in the commutation time, d/v . To achieve critical damping, the capacitor should have a value

$$C = 4 L_1 / (R_1 + R_x)^2 \quad \text{II.1.3.13}$$

The total resistance of the circuit should then be

$$R_1 + R_x = 2 K (v/d) L_1 \quad \text{II.1.3.14}$$

where K is equal to the commutation time divided by the time constant of the damping, and should generally be chosen greater than two, so that the current has a chance to reach steady state. Plugging this back in yields

$$C = (1 / K^2 L_1) (d/v)^2 \quad \text{II.1.3.15}$$

and the voltage rating on the capacitor should then be

$$V_{Cmax} = I_0 R_1 + I_0 K (v/d) L_1 \quad \text{II.1.3.16}$$

since the capacitor must maintain $I_0 R_1$ in steady state and experiences additional voltage peaks of $I_0 K (v/d) L_1$ during each commutation cycle.

In conclusion, the electrical limits of helical rail guns are really soft limits rather than hard limits such as those

presented in the thermal or mechanical sections. However, if they are not properly designed for, they can limit the performance of an accelerator to well below that predicted by theory by introducing arcing and excessive wear.

II.1.4 Scaling Limits

Although helical rail guns apparently have no intrinsic upper limit to their size, the need to allow for fixed mechanical clearances places a lower limit on their size. This is because the magnetic coupling, and therefore the performance of the accelerator, is heavily dependent upon the ratio of clearance to scale size, which should be made as small as possible for best results. (Indeed, this is a characteristic of all electromagnetic accelerators.)

II.2. Coupling To The Load, And The Effects Of Geometry

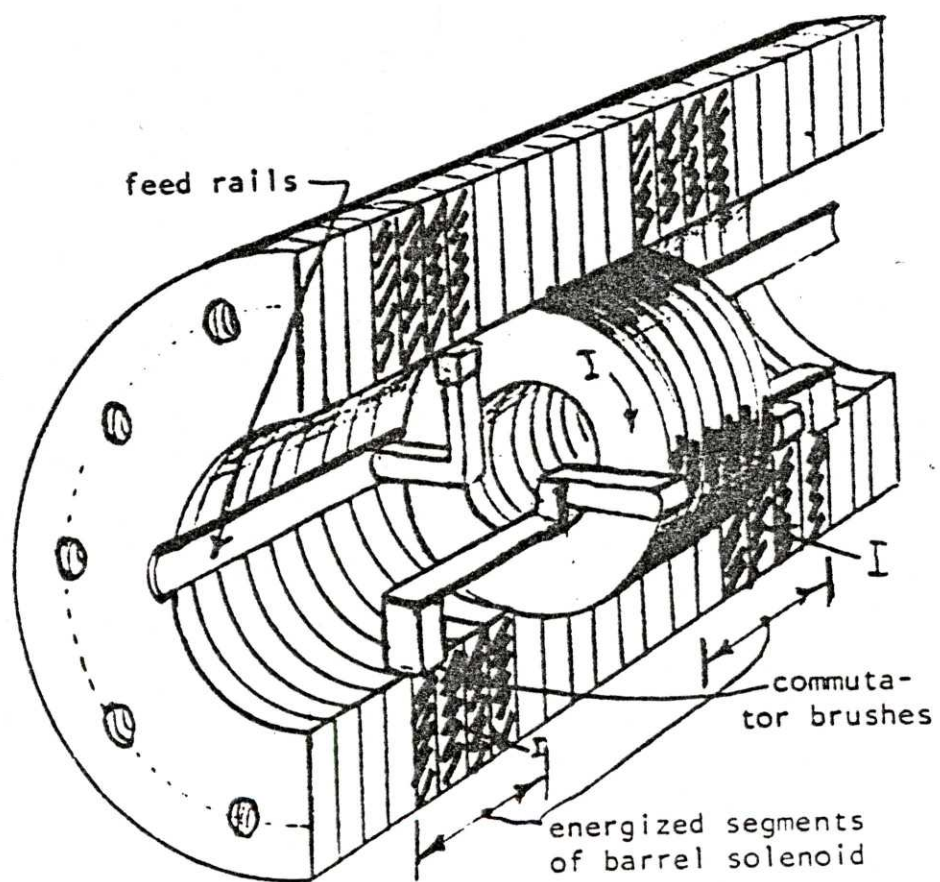
As mentioned in the introduction, the geometry of helical rail guns is capable of being varied quite extensively. The bucket can be wound to slide either on the inside or the outside of the helix; and the bucket can either completely encircle the helix or it can be wound into a saddle geometry. This section will examine the advantages and disadvantages of each of these alternatives in turn.

II.2.1 Inside Geometries

A typical helical rail gun exhibiting inside geometry is shown in Figure II.2.1.1. The bucket slides inside the helix which has certain advantages, and other counter balancing disadvantages. The most immediate advantage is the freedom to mechanically support the helix along its entire length, since there does not have to be clearance to allow for the movement of the bucket. This allows the helix to be made arbitrarily long, since sagging is eliminated as a problem. This advantage is offset by several disadvantages however. The first is the necessity to supply electrical power to the bucket, which requires either feed rails running the length of the helix on the inside, or power cables with the ability to be played out to the length of the helix as the bucket accelerates. Interior feed rails complicate the problem of mechanical clearances and often decrease the magnetic coupling which can be achieved; and accelerating power cables present engineering difficulties all their own.

Another difficulty is coupling to the load to be accelerated. If the load conveniently fits inside the helix, then mechanical coupling is easily accomplished, and the load can be accelerated as if it were a projectile in a gun. If the load is not so conveniently shaped, then some provision must be made to transfer to it the force generated by the bucket. Most schemes which come to mind, such as

Figure II.2.1.1
Inside Geometry Helical Rail Gun



push-rods or cable and pulley arrangements, have difficulties of their own, such as buckling of the push-rod or snapping of the cable under acceleration.

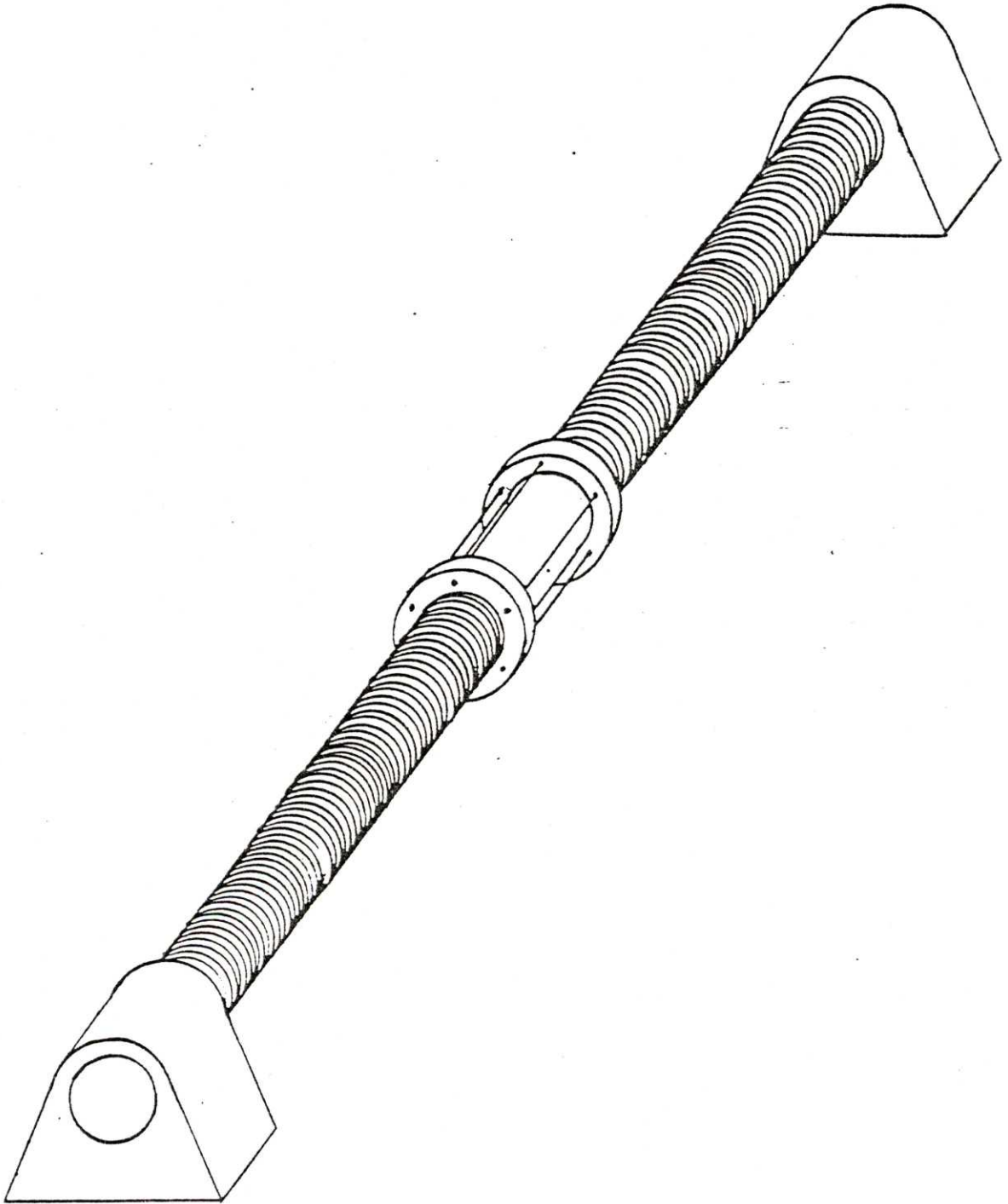
One further advantage of inside geometries should be noted. Since all of the exposed conducting surface of the helix is inside a tube, it is protected from environmental weathering to a much greater degree than any other geometry which will be considered here. This could be important in certain applications, such as field artillery.

II.2.2 Outside Geometries

Figure II.2.2.1 illustrates a typical helical rail gun with an outside geometry. Helical rail guns of this type are easy to construct and have several other advantages: an arbitrarily shaped and sized load may be directly attached to the bucket, thus alleviating problems of mechanical coupling; also, feed rails for bucket energization may be run alongside the helix and supported separately, where they will not interfere with the magnetic coupling of the bucket.

The primary disadvantage of outside geometries is that, for buckets which completely encircle the helix, the helix can only be supported at the two endpoints, assuming the bucket is brought to rest. (Otherwise, the helix would have to be cantilevered from the breech.) This leads to problems with helix sag and "twang" as the length to diameter ratio becomes large. However, if this can be kept within bounds, outside geometries work very well.

Figure II.2.2.1
Outside Geometry Helical Rail Gun



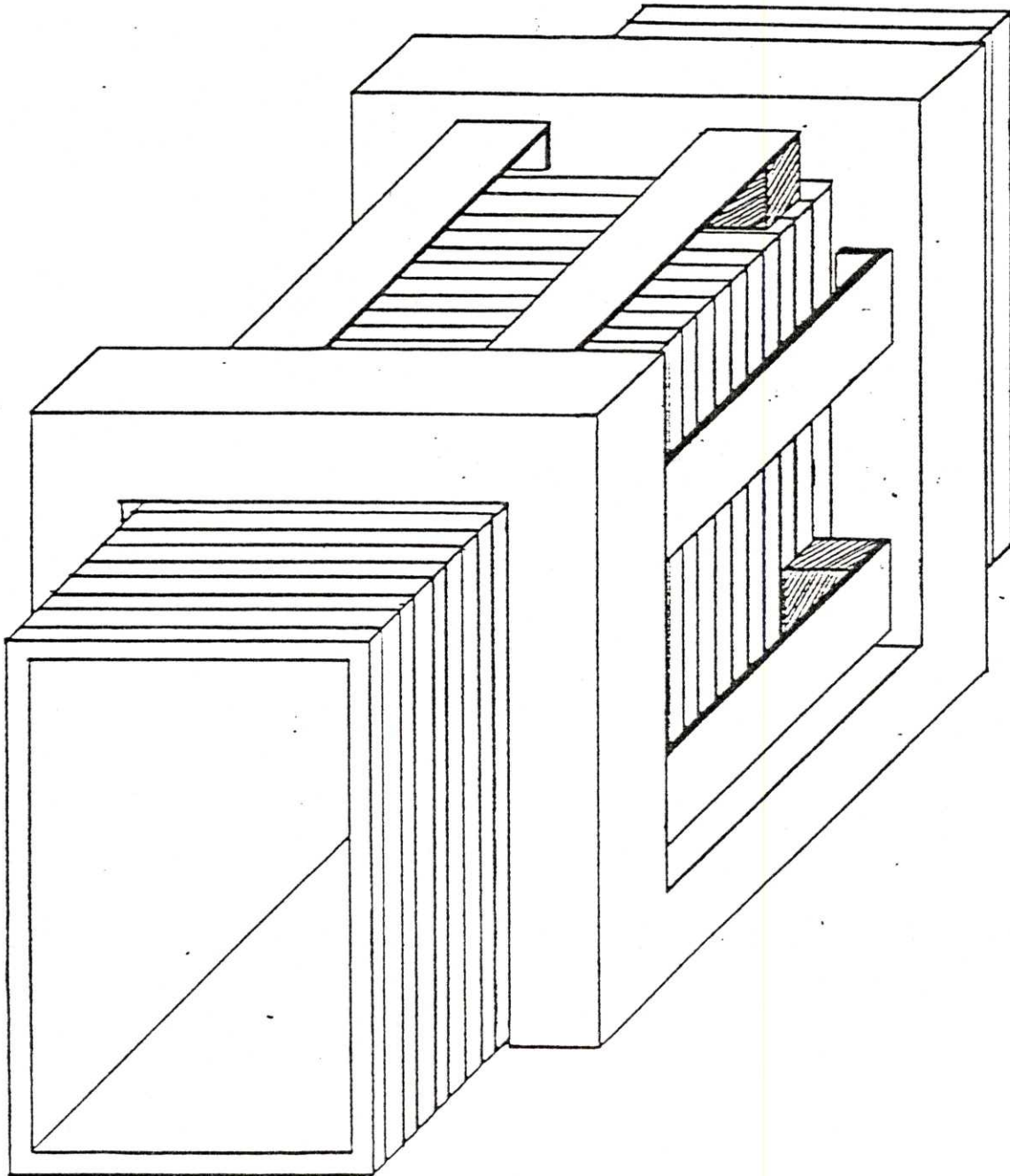
II.2.3. Saddle Buckets

The helical railgun described above suffers from an intrinsic limitation on the length of its helix, due to the lack of continuous mechanical support. One modification to this design, which allows support along the whole length of the helix while maintaining the flexibility of an outside geometry, is shown in Figure II.2.3.1. There, the completely encircling bucket of Figure II.2.2.1 has been replaced by a bucket exhibiting "saddle" geometry, in which the bottom of the bucket is split to allow for support of the helix. The saddle bucket is so named because the bucket sits on the helix like a saddle sits on a horse. This design has all of the advantages of an outside geometry bucket, but it pays for the ability to support the helix through reduced magnetic coupling. Typically this coupling is reduced by approximately the percent total encircling of the helix by the bucket. That is, if the bucket encircles 75% of the helix, then the coupling will be approximately 75% of that achieved by an equivalent bucket which fully encircles the helix.

In designing rectangular helical rail guns with saddle buckets, the effect of the height to width ratio of the helix must be considered. If the height to width ratio is made very much larger than one, i.e. if the helix is made tall and thin, then although the effect of the uncoupled

Figure II.2.3.1

Saddle Bucket Rectangular Geometry Helical Rail Gun



bottom of the helix is made negligible, the two sides of the helix begin to interfere with each others' coupling. Alternatively, if the height to width ratio is made less than one, then the uncoupled bottom of the helix begins to interfere with the coupling of the top, and the two sides begin to decrease in length, which also decreases their coupling. The optimum height to width ratio turns out to be very nearly 1.5 for a wide range of couplings, and this value should be used in default of a better choice.

One other disadvantage was briefly touched on in the section on mechanical limits. Since saddle buckets do not encircle the helix, they can not close on themselves and support mechanical bursting forces with hoop stress. This makes them intrinsically weaker than encircling buckets. However, by supporting their cantilevered sides, and using appropriate mechanical reinforcement, this should not be a limit to design or operation.

II.3 Efficiency

As in all electromagnetic accelerators the efficiency of helical rail guns increases as their speed of operation increases. The instantaneous efficiency of operation is

$$\eta_{inst} = P_{mech} / P_{in} \quad \text{II.3.1}$$

where the mechanical power, P_{mech} , and the total power input, P_{in} are

$$P_{mech} = F v \quad \text{II.3.2}$$

and

$$P_{in} = F v + P_{loss} \quad \text{II.3.3}$$

Plugging into Equation II.3.1 yields

$$\eta_{inst} = 1 / (1 + u/v) \quad \text{II.3.4}$$

where v is the velocity of operation, and where u , the break point velocity, has been substituted for the ratio of power lost to force generated.

The instantaneous efficiency given above can also be integrated with respect to time to give an average or total

efficiency,

$$\eta_{\text{total}} = 1 - (u/v) \ln(1 + v/u) \quad \text{II.3.5}$$

which is shown together with the instantaneous efficiency in Figure II.3.1. In both cases it is important for efficient operation that the operating velocity be significantly greater than the break point velocity.

The break point velocity will in general be a function of many variables, including current, magnetic coupling, resistance, air drag, friction, etc. However, it turns out that for almost all helical rail gun applications the dominant loss mechanism is resistive power dissipation. Plugging that into the equation for the break point velocity yields

$$u = \frac{I_b^2 R_b + I_d^2 R_d}{(I_b N_b)(I_d N_d) b} \quad \text{II.3.6}$$

where b has been used in place of dM/dz , the magnetic coupling. Rearranging terms yields

$$u = \left[\frac{1 + \left(\frac{N_d}{N_b}\right)^2 \left(\frac{R_d^{\circ}}{R_b^{\circ}}\right)}{\left(N_d/N_b\right)} \right] \left(\frac{R_b^{\circ}}{b}\right) \quad \text{II.3.7}$$

which holds for both series and parallel operation. R_d° is the single turn resistance of the drive coil and R_b° is the single turn resistance of the bucket coil, single turn referring to the resistance which would be measured if the

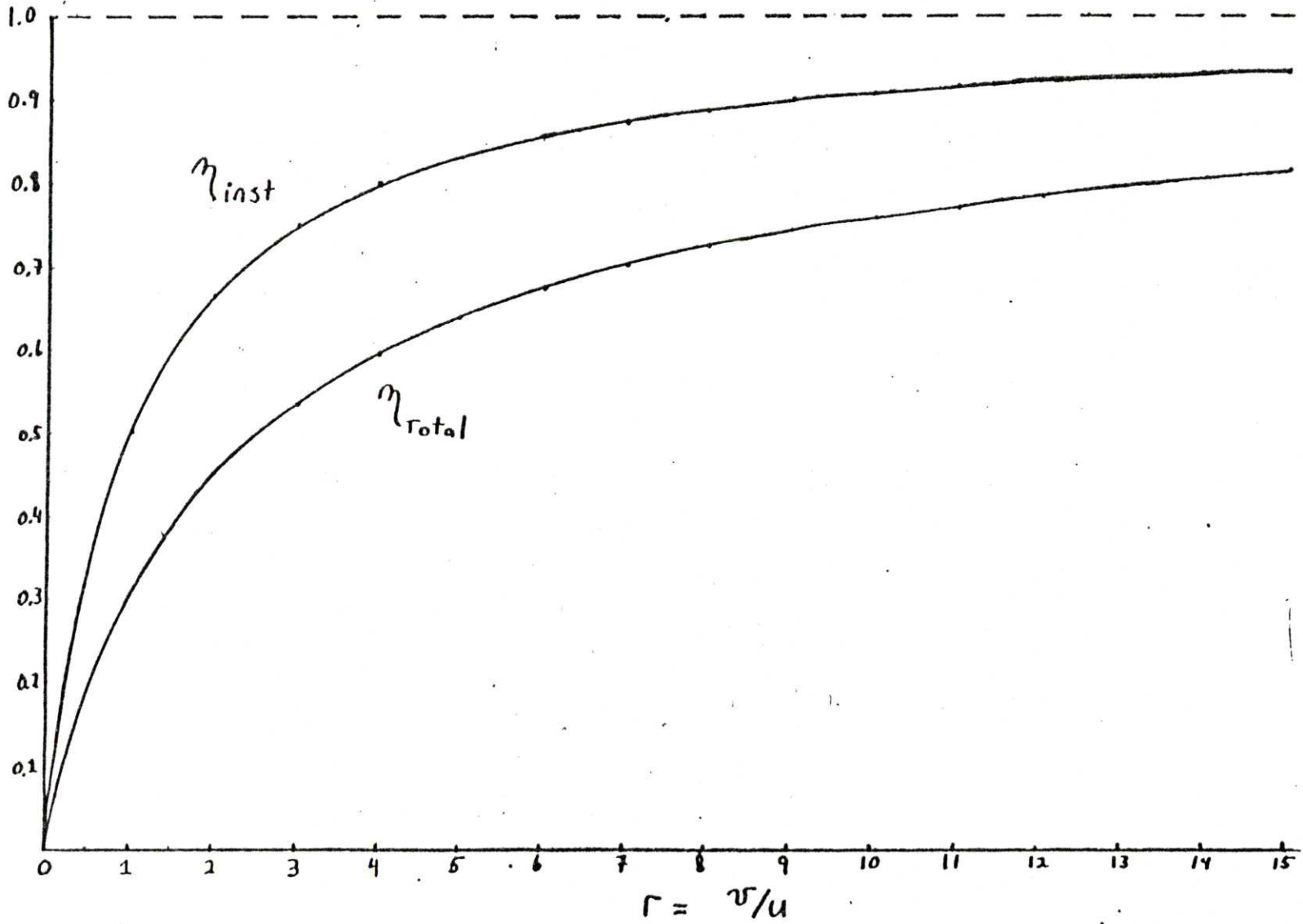


Figure II.3.1
Instantaneous and Total Efficiency

coil consisted of a single monolithic piece of conductor.

The efficiency given in Equation II.3.4 can be maximized by minimizing u given in Equation II.3.7. (The efficiency of an existing device is fixed; this argument applies mainly to the design of new devices.) The break point velocity, u , is minimized by varying the turns ratio, N_d/N_b . The maximum efficiency is obtained when the turns ratio is chosen to be

$$(N_d/N_b)_{\text{optimum}} = \sqrt{R_b^{\circ}/R_d^{\circ}} \quad \text{II.3.8}$$

which yields

$$u_{\text{minimum}} = \frac{2\sqrt{R_b^{\circ}R_d^{\circ}}}{b} \quad \text{II.3.9}$$

This turns ratio should be chosen whenever possible in the initial design of a helical rail gun. The actual number of turns can then be picked to match the voltage and current put out by the power supply.

As an interesting sidelight, it can be shown that the efficiency is maximized when the power dissipation in the bucket is equal to the power dissipation in the drive coil. The force generated by the bucket can be expressed in terms of the dissipated electrical power as

$$F = N_b N_d b \sqrt{(P_b P_d) / (R_b R_d)} \quad \text{II.3.10}$$

where P_b is $I_b^2 R_b$, the power dissipated in the bucket, and

P_d is $I_d^2 R_d$, the power dissipated in the drive coil. Since the sum of P_b and P_d is assumed to be a constant P_o , substituting in for P_d and differentiating with respect to P_b yields the power distribution which generates the most force, $P_b = P_o/2$. Thus the maximum force produced per unit power dissipated is found to occur when $P_b = P_d$, regardless of the geometry or configuration.

II.4. Exotic Solutions

In the introduction it was mentioned that helical rail gun buckets may be either active or passive; active buckets having energized conductors and passive buckets using permanent magnets or ferromagnetic materials. This section will examine the methods used to analyse passive buckets, beginning with permanent magnets, and then considering ferromagnets.

II.4.1. Permanent Magnet Buckets

Figure II.4.1.1 shows a passive bucket using a permanent magnet shaped in the form of a torus, with a rectangular cross-section. Although power must still be supplied through the bucket to the drive coils, the bucket itself does not need to be energized; instead, the magnetic field of the permanent magnet interacts with the currents in the drive coils to produce the drive force.

Since a permanent magnet is characterized by a constant magnetic dipole density throughout its bulk, it can be modeled as if there were an effective current flowing on its surface. For the bucket shape shown in Figure II.4.1.1 (see the upper drawing of Figure II.4.1.2) two counter-rotating surface currents are required to constrain the magnetization field to the body of the magnet.

If the magnetization vector \vec{M} is known, the magnitude of the magnetization surface current K can be calculated using Ampere's law. Using this gives

$$K = M$$

II.4.1.1

The direction of the flow can then be found using the right hand rule. Table II.4.1.1 gives the parameters of various permanent magnets, where the magnetization vectors can be calculated using the residual field listings.

Figure II.4.1.1

Permanent Magnet Bucket Helical Rail Gun

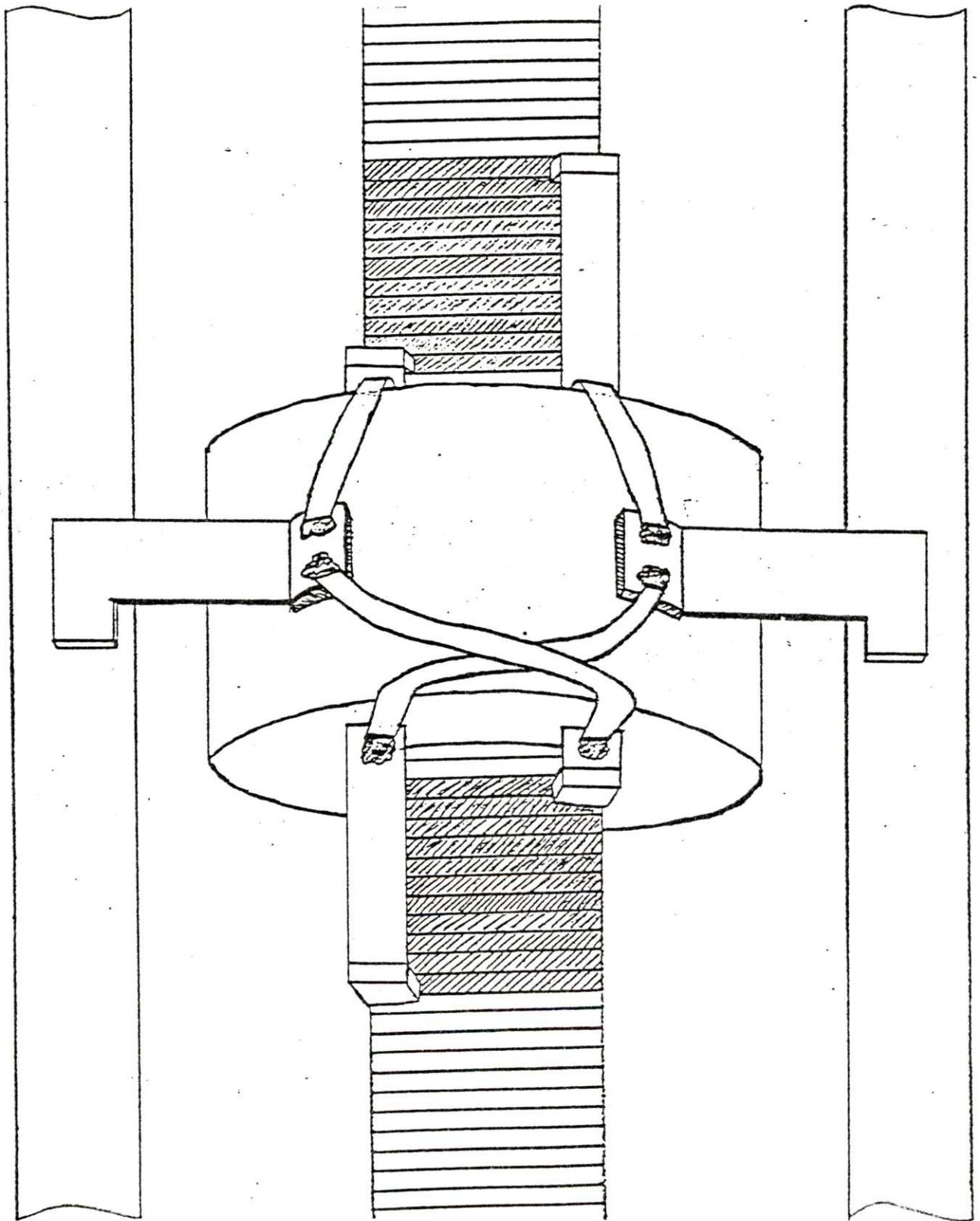


Figure II.4.1.2

Permanent Magnet Effective Surface Currents

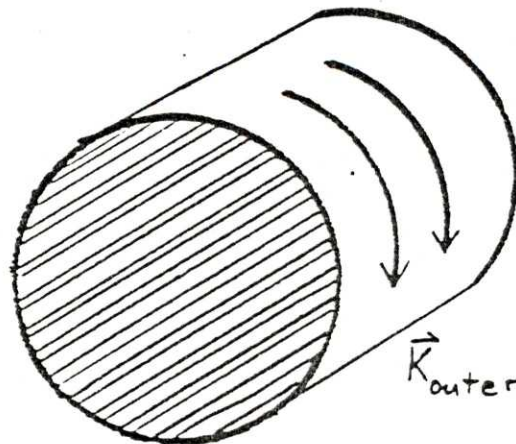
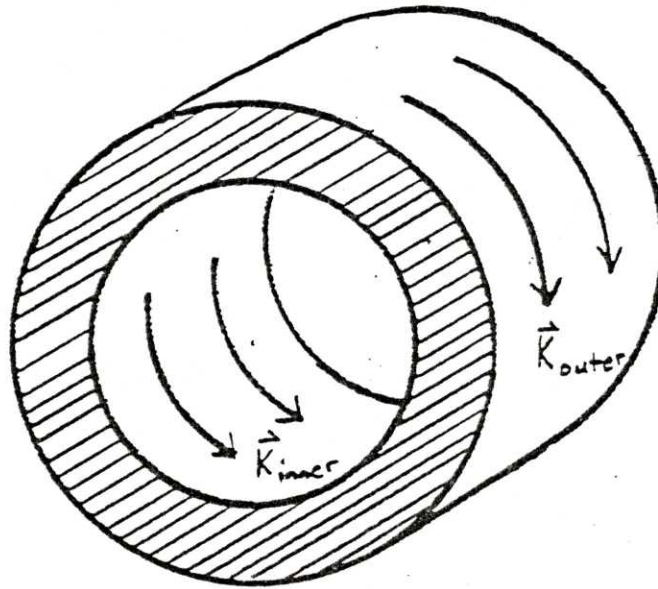


Table II.4.1.1

Constants of Permanent Magnet Materials

Name	H _c Coercive Force (Oersteds)	B _r Residual Field (Gauss)	μ _r Reversible Permeability	Density (gm/cm ³)
1% Carbon Steel	51	9000	7.8
5% Tungsten Steel	70	10,500	30	8.1
3.5% Chrome Steel	66	9,500	35	7.8
36% Cobalt Steel	240	9,750	12	8.2
Vicalloy-2	415	9,000	6.0*	8.2
Alnico-5	620	12,500	4.3	7.3
Alnico-6	750	10,500	4.8	7.4
Alnico-8	1,600	8,300	2.6	7.3
Alnico-9	1,450	10,500	1.3	7.3
Platinum Cobalt	4,300	6,450	1.2	15.7
Silmanal	6,300	590	1.1	9.0
Samarium Cobalt	8,400	8,700	1.05*	8.3*

Data taken from: **American Institute of Physics Handbook**,
pg. 5-165.

* Data from product information supplied by Thomas and
Skinner Inc., Indianapolis Indiana.

The performance of helical rail guns with permanent magnet buckets is easily analysed using the same method that was used to analyse buckets with active windings. That is, first the magnetic coupling or dM/dz is determined assuming that the magnetization surface current is really current flowing through a series of fine windings. Next the bucket current, I_b , is determined by multiplying the surface current, K , by the axial length of the magnet. The number of turns in the bucket, N_b , will be one. Finally, the drive coils are analysed as before, and the force is calculated using Equation II.1.1, the mass driver equation.

Since permanent magnet buckets provide "free" energization of the bucket coils, why bother with actively energized buckets at all? One reason is that the bucket coils of a permanent magnet (i.e. the surface currents) have poor magnetic coupling with the drive coils if enough magnet material is used to provide a reasonable total bucket current. For best magnetic coupling, the windings of an active bucket would like to be clustered in an annulus close to the mouth of the drive coil, of approximately equal axial and radial extent. The equivalent bucket coils of a permanent magnet, however, are shaped like thin cylindrical shells, of almost no radial thickness. Thus to get a bucket current which is large enough to be of value, the magnet must be extended in the axial direction, placing most of the extra surface current in a region of low magnetic coupling.

A further degradation of magnetic coupling occurs with

permanent magnets because most geometries (including all outside bucket geometries) require a return path for the magnetization surface current. This return current will of necessity flow in a direction opposite to the primary current and will therefore degrade the performance. Inside geometries with no holes are not affected by this, however, since the primary current path completely encircles the bucket. Figure II.4.1.2 illustrates this coupling problem with permanent magnets.

Permanent magnets also have difficulty generating high force levels. The force produced by the bucket of a helical rail gun is proportional to the product of the bucket current and the drive coil current. In an active bucket, these two currents are proportional to one another, and so the force produced by the bucket is proportional to, I_d^2 , the drive coil current squared. In a permanent magnet bucket, however, the equivalent bucket current is fixed, and limited by saturation to a relatively low value; therefore the force produced is only proportional to I_d . Thus, although permanent magnet buckets exhibit better performance at low current levels, they are quickly outdistanced by active buckets as the current is raised.

II.4.2. Ferromagnetic Buckets

Another passive configuration is the use of ferromagnetic materials in the bucket, with a single forward drive coil for attraction. Such a configuration is shown in Figure II.4.2.1. For values below saturation, the magnetic field generated in a ferromagnet is determined by the field imposed on it. Thus, the mass driver equation for ferromagnetic buckets becomes

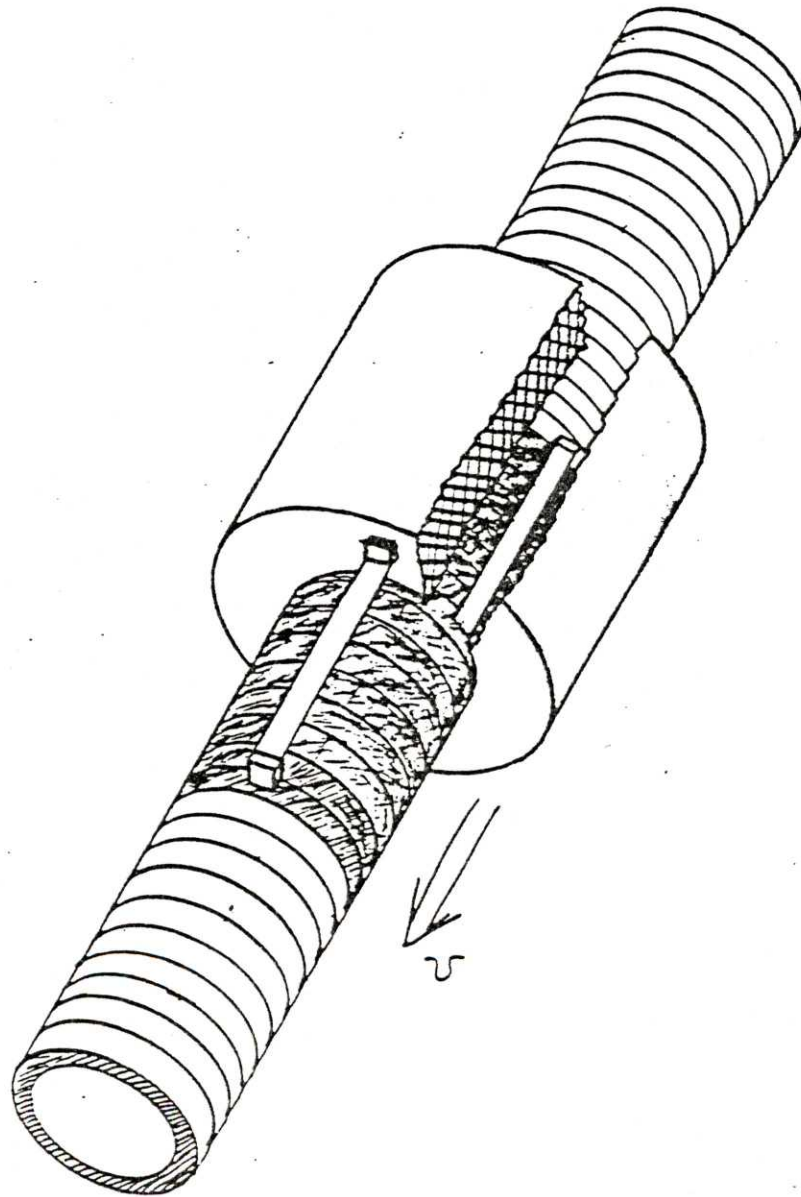
$$F = (1/2) N_d^2 I_d^2 dL/dz \quad \text{II.4.2.1}$$

where dL/dz is the gradient of the self inductance of the drive coil, a measure of the magnetic coupling between the drive coil and the ferromagnetic bucket. The analysis of passive ferromagnetic buckets then comes down to determining the self inductance gradient for various configurations of the bucket and drive coil.

For the purposes of this thesis, I decided to perform experimental tests on a few geometries of interest to determine the range of dL/dz 's which were available, rather than attempt elaborate analysis, since no simple techniques lent themselves to the problem. The tests were performed using coaxially mounted single layer coils and sections of steel pipe and bar stock. The inductance of a given configuration was measured with a resonant tank oscillator

Figure II.4.2.1

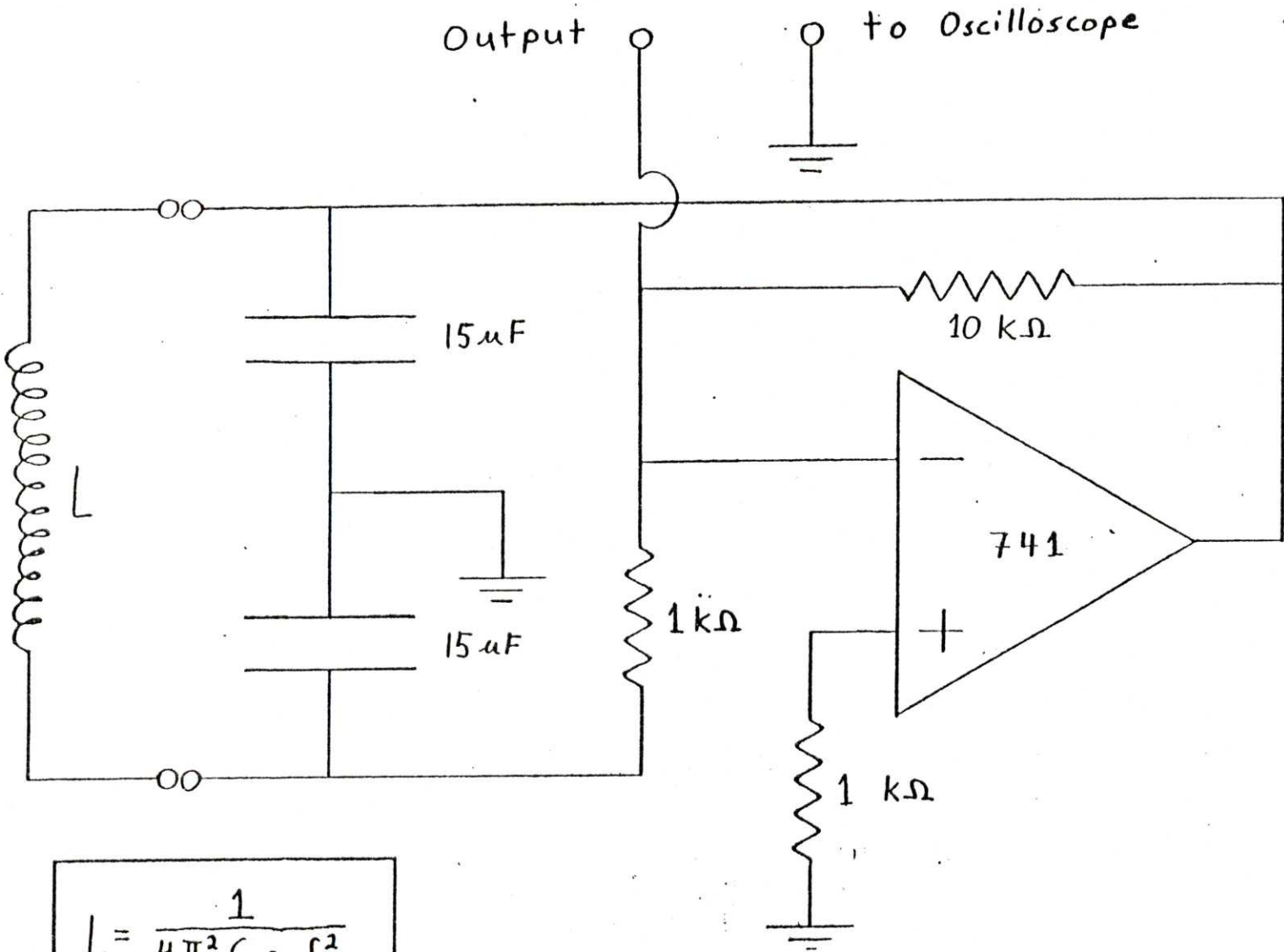
Ferromagnetic Bucket Helical Rail Gun



circuit (shown in Figure II.4.2.2) for various axial separations between the pipe and coil. Table II.4.2.1 gives the dimensional data on the coils and pipes used, and the coils and pipes themselves are shown in Figure II.4.2.3.

The inductance gradients were then determined from the slopes of the inductance vs separation curves, which are given in Figure II.4.2.4. This figure shows the normalized inductance of the coil (inductance divided by number of turns squared) plotted as a function of the separation between the coil and the iron. The maximum inductance gradient is seen to be about 2.7 microhenries per meter; it increases as the radial clearance between the coil and the iron decreases, and also increases as the radial extent of the iron increases. Also for a given piece of iron, with roughly equivalent radial clearances, inside geometries have higher performances than outside geometries. The outside geometries tested exhibited inductance gradients of about 0.5 microhenries per meter, much lower than the peak exhibited by the inside geometries, but comparable to those inside geometries not so tightly coupled. Outside geometries can probably be made to increase their inductance gradient by increasing the radial thickness of the iron, to intercept more flux, and by decreasing the radial clearance, thereby increasing the coupling.

Passive ferromagnetic buckets are certainly not to be ruled out as workable helical rail gun designs. They are capable of generating respectable magnetic couplings, comparable to those achievable with active buckets, and



$$L = \frac{1}{4\pi^2 C_{eff} f^2}$$

Oscillator Circuit Used To Measure Inductance

Figure II.4.2.2

Table II.4.2.1

Coil and Pipe Data

Coil A: Number of Turns = 50
Inductance = 306 microhenries
Normalized Inductance = 0.122 microhenries
Outside Diameter = 9.78 centimeters
Axial Length = 3.84 centimeters
Wound from 22 gauge round magnet wire
Aircore

Coil C: Number of Turns = 50
Inductance = 323 microhenries
Normalized Inductance = 0.129 microhenries
Outside Diameter = 10.46 centimeters
Axial Length = 3.94 centimeters
Wound from 22 gauge round magnet wire
Aircore

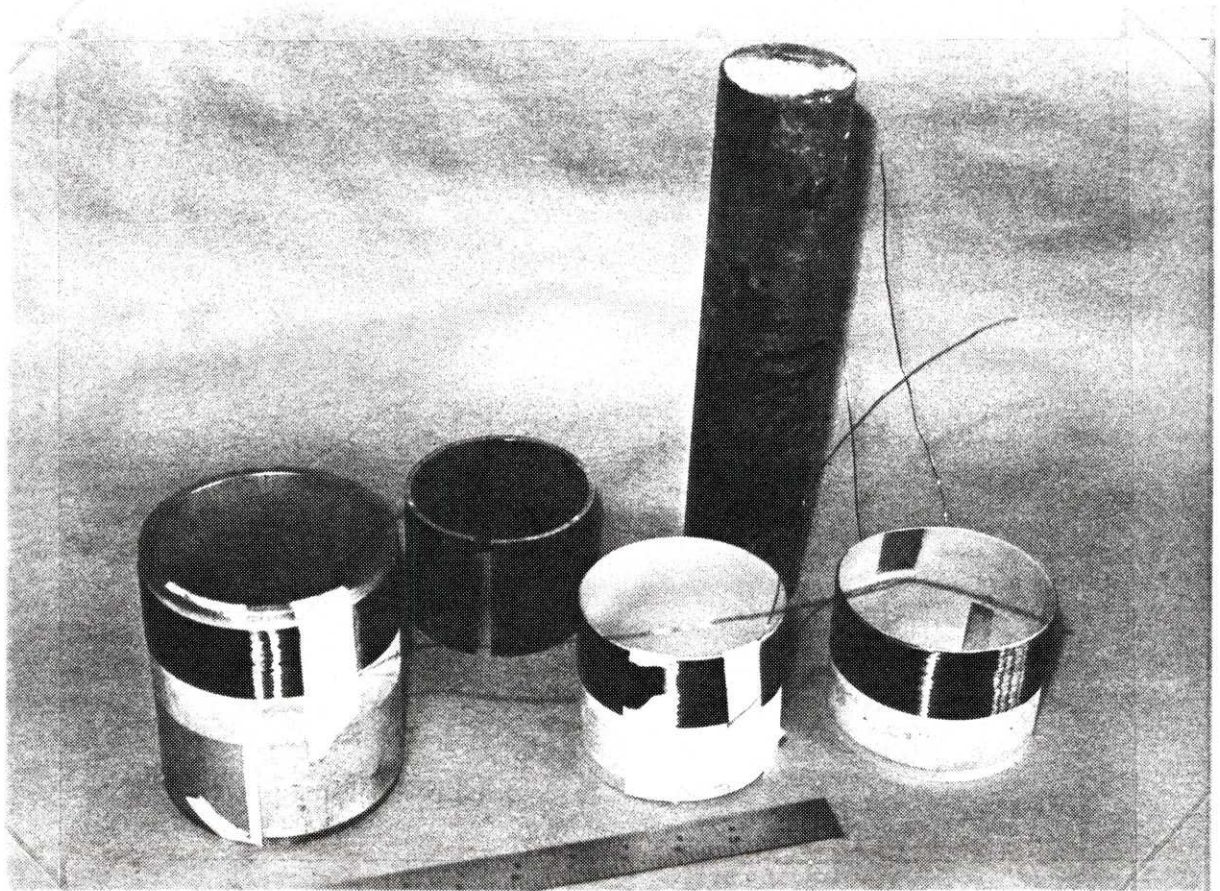
Iron Pipe #1: Axial Length = 13.2 centimeters
Outside Diameter = 11.3 centimeters
Wall Thickness = 6.0 millimeters
Slit Axially, With a 1 mm Insulated Gap
Mild Steel

Iron Pipe #3: Axial Length = 7.2 centimeters
Outside Diameter = 9.8 centimeters
Wall Thickness = 3.5 millimeters
Slit Axially, With a 9 mm Airgap
Steel

Iron Bar: Axial Length = 30.5 centimeters
Diameter = 7.0 centimeters
Steel

Figure II.4.2.3

Coils and Pieces of Iron Used to Measure dL/dx



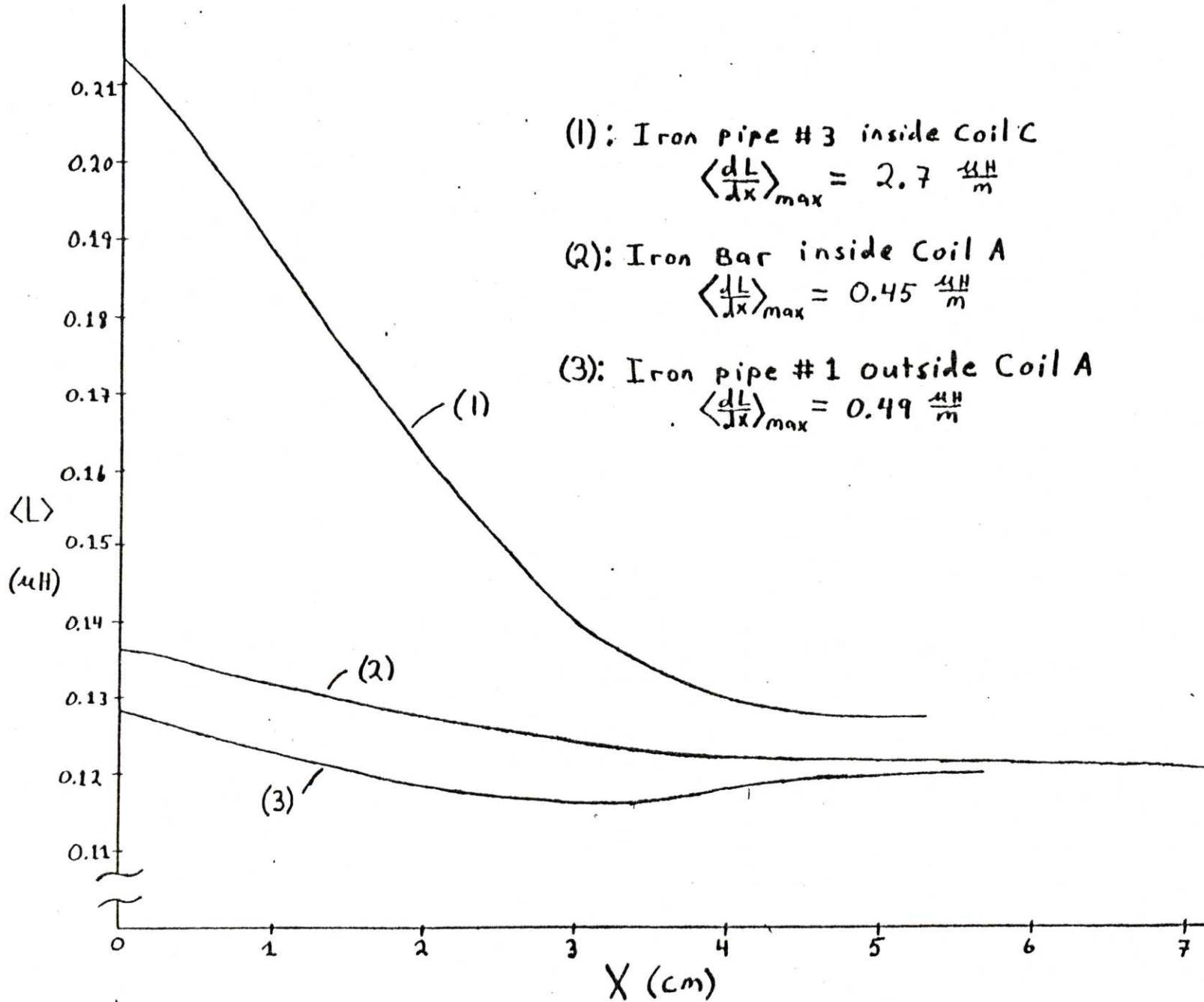
Iron Pipe #1

Coil A

Coil C

Iron Pipe #3

Iron Bar (rear)



Inductance Versus Separation Curves (Experimental)

Figure II.4.2.4

there is no bucket heating to impose a thermal limit on the device. (There is, of course, thermal heating of the drive coil, but, since this is spread over an extended area of the helix, it should not be a dominant limit.) This allows operation at the higher current limit imposed by either mechanical containment or commutating brush wear.

Of course ferromagnetic buckets have other problems. For example, soft iron saturates at a magnetic field of about 20,000 gauss, and most other ferromagnetic materials saturate at even lower fields. Thus the performance of ferromagnetic buckets in high magnetic fields suffers from the same limitations as buckets using permanent magnets, the only difference being that the field is twice as high.

II.4.3 Exotic Solution Conclusions

In viewing the possible alternative configurations for the design of helical rail guns, the three options considered here (active buckets, passive buckets using permanent magnets, and passive buckets using ferromagnets) tend to lend themselves to the tasks that they perform the best. For tasks involving moderate forces over distances that make inside geometries practical, permanent magnets can be effectively employed. In this case fixed mechanical clearances severely limit the magnetic coupling which can be achieved, so the surface current distribution of the permanent magnet becomes less of an issue. Also the moderate forces needed can be generated by moderate power supplies since the constant "current" generated by the magnet is now large relative to the drive coil current, and therefore an asset. And finally the assumption of inside geometry is advantageous to permanent magnets. The "Star Trek" door opener mentioned later is just such a task.

Passive ferromagnetic buckets are well suited to tasks involving the generation of moderate to large forces for very long times, since they are not limited by thermal heating in the bucket. The commercial aircraft take-off assist launcher described later is of this type.

Finally, active buckets can perform both of the above tasks well, in addition to tasks involving the generation of

high fields and high forces using large currents. Given their flexibility they are the design of choice for almost all applications. They will be utilized in all of the designs given later.

III. Experimental Results

III.1. 1-Meter Bench-Top Helical Rail Gun

The first helical rail gun constructed by the Electromagnetic Acceleration Group was the 1-meter long bench-top model to test the feasibility of the helical rail gun concept. Those tests proved successful; accelerations of up to 300 g's were demonstrated, and final velocities in the tens of meters per second range were achieved.

The 1-meter helical rail gun was constructed around a four inch diameter helix made by winding rectangular copper wire around a cylindrical phenolic tube. The wire was single strand 0.1 inch by 0.15 inch copper, insulated with a fiberglass, nylon and dacron wrap. It was potted in epoxy as it was wound around the phenolic, and after the epoxy had cured, the outside of the helix was machined on a lathe to expose bare copper.

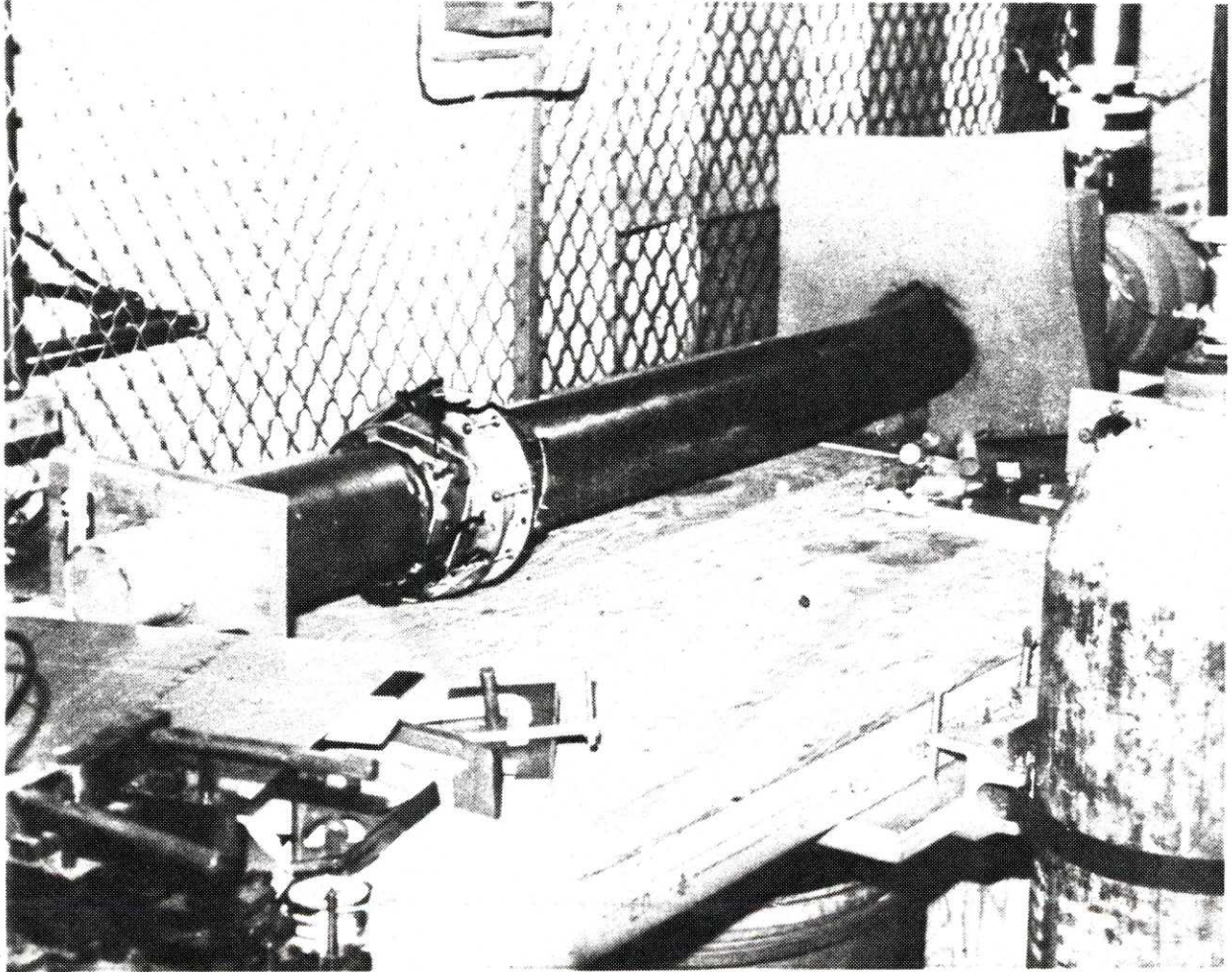
The bucket was constructed with a single circular drive coil, sliding on the outside of the helix, and with two drive coils, one fore and one aft, providing the propulsive forces. Each of the drive coils was energized by two leading brushes and two trailing brushes; power was supplied to the bucket by a tether made from 12 gauge multistranded insulated copper wire.

The bucket was constructed by first winding the bucket

coil onto the middle of a six inch long thin-walled phenolic tube, which had been machined to slide over the outside of the helix. The bucket coil was wound of 0.1 inch square copper magnet wire, and had a rectangular cross-section of 3.7 cm axial length and 1 cm radial build, with a total of 30 turns. The wire was potted in epoxy, and held in place by thin G-10 sidewalls fore and aft, which were secured by drawbolts. Next, the brush supports were made by epoxying thick phenolic rings to the ends of the thin walled tube. And finally the helix brushes, which consisted of graphite copper automobile starter motor brushes brazed onto the ends of beryllium copper leaf springs, were screwed to the brush supports and attached underneath the bucket coil drawbolts. The 1-meter benchtop helical rail gun is shown in Figure III.1.1.

Figure III.1.1

1-Meter Bench-Top Helical Rail Gun

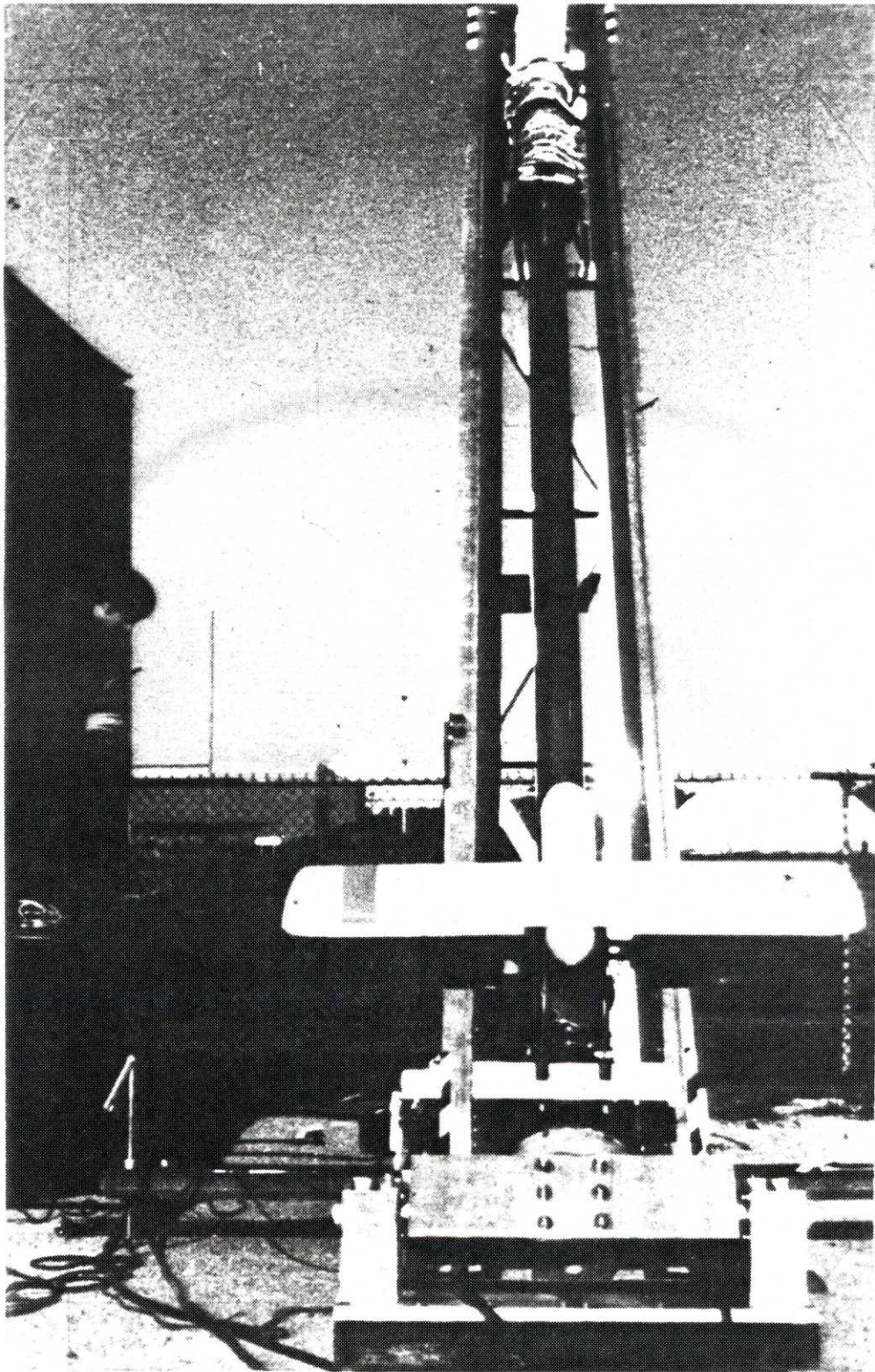


III.2. Glider Launcher

The helical rail gun glider launcher, shown in Figure III.2.1, is the largest project which the Electromagnetic Acceleration Group has undertaken to date. It features a 3.6 meter (12-foot) long helix, constructed from two 1.2 meter acceleration sections and one four-foot deceleration section, with a compound bucket which is supplied with power from adjacent feed rails running alongside the helix. It is mounted on a low six-wheeled cart making it transportable, and it has the capability to be adjusted to any launch angle up to 45 degrees, using a winch driven scissors mechanism. It has repeatedly launched 3.5 kilogram model gliders to a velocity of 40 meters per second, as well as a 1.75 kilogram rocket to 55 meters per second. Throughout, the power source used was four independently switched one farad electrolytic capacitor banks capable of storing a total of 240 kilojoules.

Figure III.2.1

Helical Rail Gun Glider Launcher



III.2.1. Construction

Construction of the glider launcher began in the summer of 1980, when work was begun on the helix and the capacitor banks, and concluded in September 1981, when the last modifications to the bucket were made prior to demonstration of the glider launcher's capabilities.

The helix was constructed in three sections from five foot pieces of transite pipe, an asbestos-cement composite commonly used for sewer pipe. The transite was first wetted with epoxy and wrapped with fiberglass cloth. Then, when the epoxy was fully cured, the fiberglass composite outer layer was machined on a lathe to a diameter of 4.895 inches. The length of the tubes was then cut to size. Next, the machined surface was wetted with epoxy and 0.1 inch by 0.15 inch insulated copper wire was wound around it to form the helix. (The wire was wound the "hard way", i.e. edge on, and the deceleration section was wound with the opposite winding pitch of the two accelerating sections.) The free ends of the wire were then secured by soldering them to specially machined bronze end caps, and finally the surface of the helix was machined to a final diameter of 5.000 inches in order to expose bare conductor and to provide a uniformly smooth surface for the helix brushes to slide on.

The helix was then assembled by sliding the helix sections over a stainless steel tube which served as an

inner core and support. Aluminum pillow blocks at either end clamped the tube, which was put in tension during assembly in order to provide axial compression of the helix sections. The difference in length between the helix and the stainless steel tube (about six feet) was made up with a phenolic over-run tube, which proved useful in testing as a space for foam braking pads, to stop the bucket in case electrical deceleration failed. Finally, horizontal plates were attached to the top and bottom of the front pillow block to hold the feed rails, which consisted of two square aluminum box beams running parallel to the helix, one on either side. This assembly is shown in Figure III.2.1.1.

The rear pillow block assembly was very similar to the front assembly, except that the horizontal plates extended further in order to accommodate fixing the hinge pins. These were aluminum pipes welded to aluminum blocks which were in turn secured to the horizontal plates. The hinge pins slid inside slightly larger pipes fixed to aluminum supports, which were in turn attached to the wheeled frame. This support arrangement fixed the helix and feed rails together, and allowed the entire assembly to be pivoted about its breech end. The breech is shown in Figure III.2.1.2.

The helix assembly was elevated by a scissors mechanism as shown in Figure III.2.1.3. The first stage elevated the helix far enough to allow the second stage to gain enough mechanical advantage to continue the elevation. When completely erected, the whole structure locked together with pins and rigidly supported the helix at a 45 degree angle.

Figure III.2.1.1
Front Helix Support

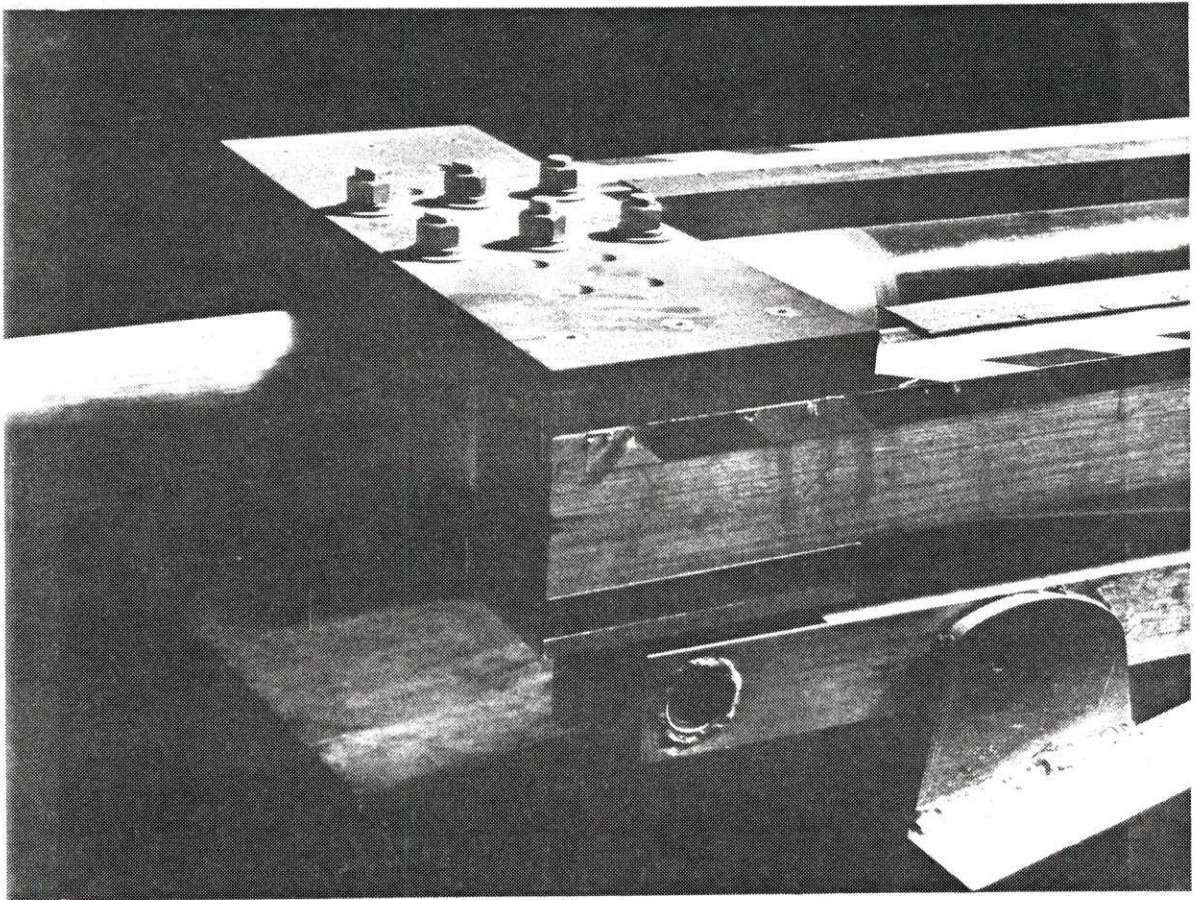


Figure III.2.1.2
Rear Helix Support (Breech)

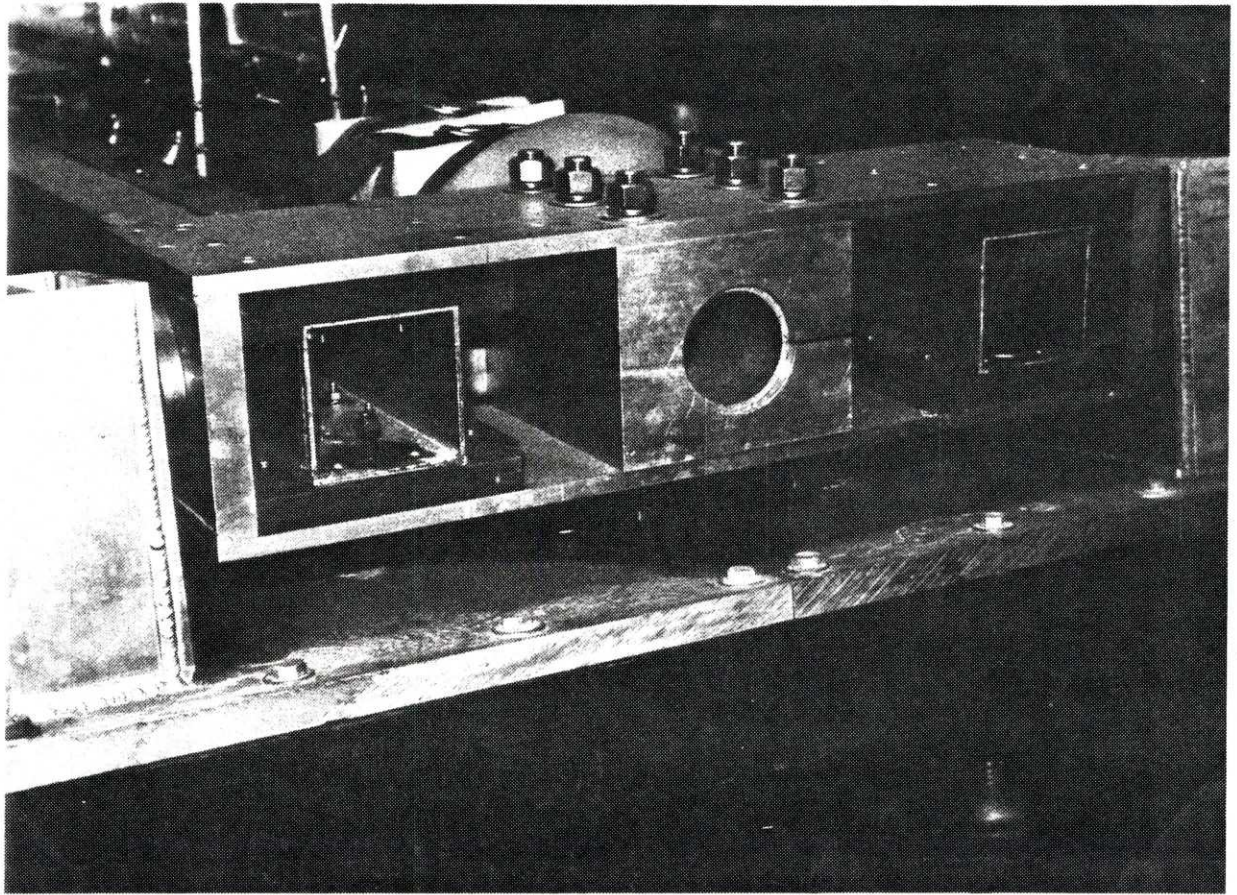
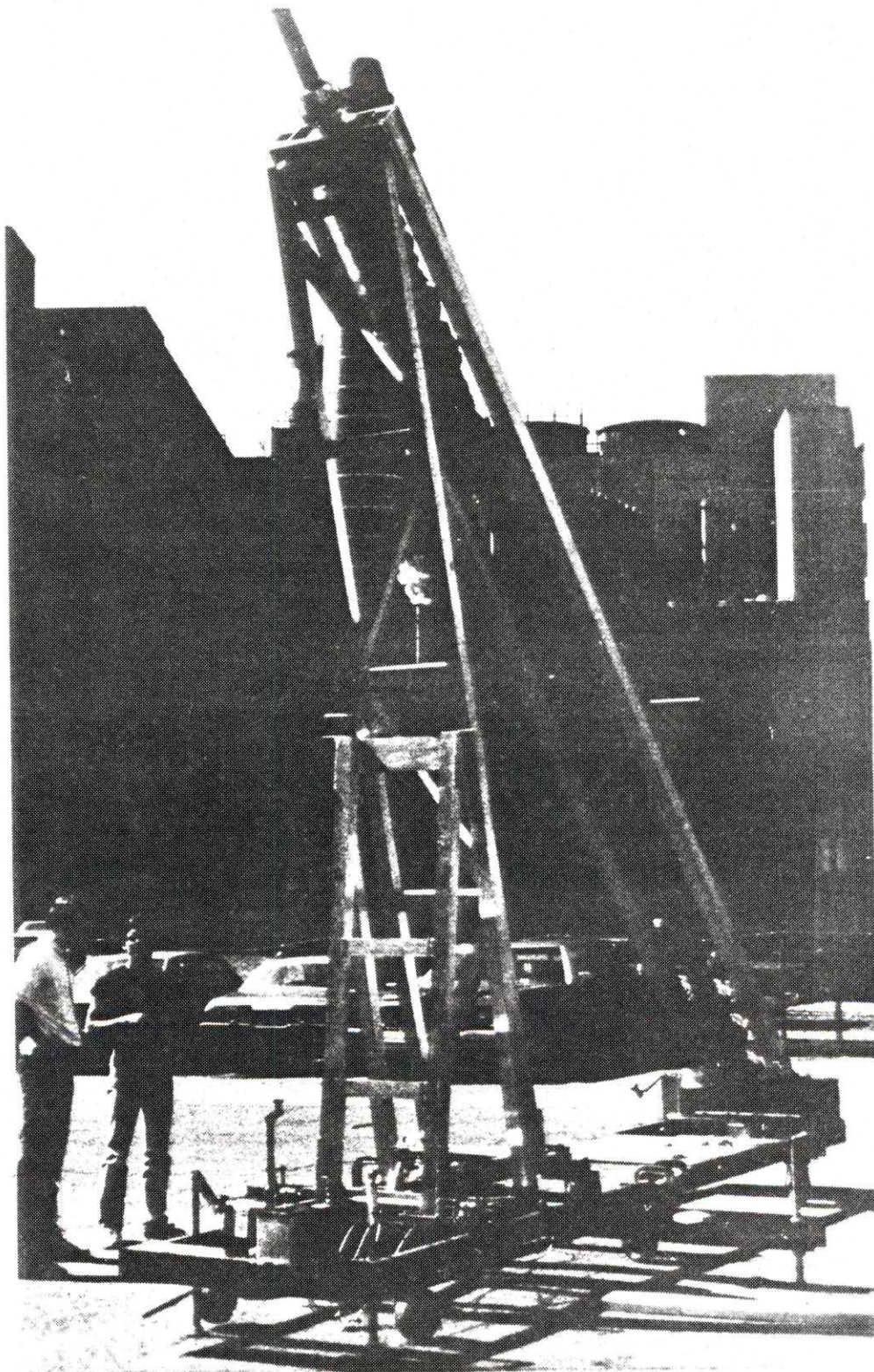


Figure III.2.1.3

Scissors Elevation Mechanism



The mechanism was operated by a winch and pulley arrangement, and the transition between stages was smooth and automatic.

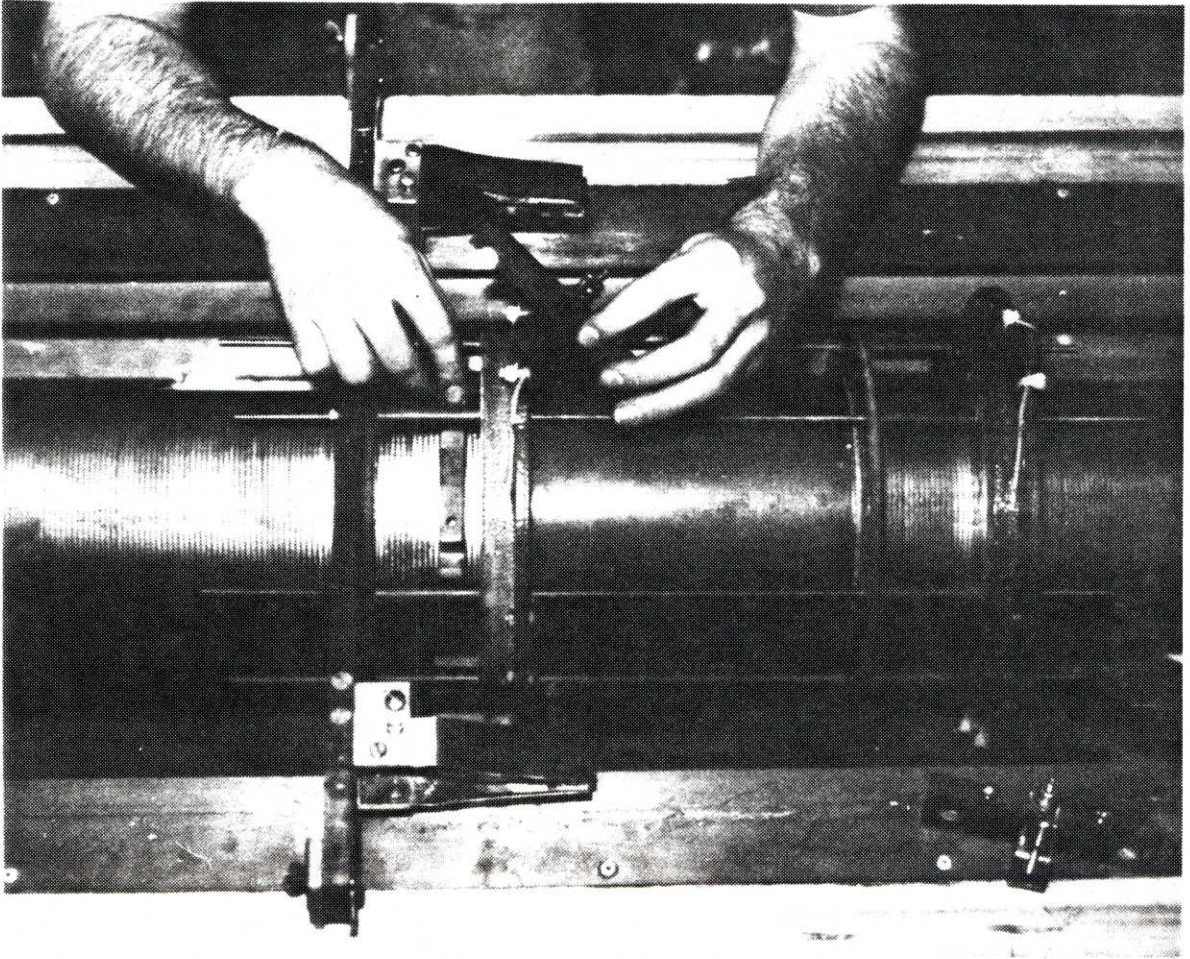
The final component of the system was the bucket. This went through three major changes and several minor ones in the course of testing. Briefly then, here is the evolution of the bucket. The first bucket consisted of two bucket coils with a ring of helix brushes between them. These helix brushes were brazed onto bolts and rigidly attached to the helix, which allowed the brushes to be spaced very closely. However, this design had to be abandoned after it was found that these brushes tended to break off under acceleration due to their rigidity.

The next bucket design replaced the ring of rigid brushes with brushes on the end of cantilevered springs. Three leading and three trailing brushes were used and a second complete bucket assembly was added behind the first. This arrangement performed satisfactorily until it was pushed to very high speeds and currents, when severe brush arcing and erosion occurred.

The third and final bucket design removed the leading bucket coil, since it was believed that the magnetic field of that coil was enhancing the arcing. The bucket then consisted of two bucket coil assemblies connected together by threaded rods and separated from one another by a thin walled phenolic tube. Each bucket coil assembly was made up of a trailing bucket coil and a leading bucket ring, which

were separated from one another by phenolic bushings slipped over the threaded rods. This left an area of bare helix accessible for the brushes, and also provided mounting points for the helix brush clamps, which were phenolic pieces that held the cantilevered springs of the brushes in place. The phenolic tube provided guidance for the bucket by having two teflon rings inside it rub on the helix, and thus prevent the bucket from tipping. The final addition to the bucket was the feed-rail brush holder. This was a piece of 1/2 inch thick G-10, machined to fit the front of the bucket, which extended out to the feed-rails on either side. In addition to preventing the bucket from being torqued around the helix by the axial component of the currents, it held the feed-rail brush holders and thence the feed-rail brushes which delivered power to the bucket. This bucket is shown in Figure III.2.1.4.

Figure III.2.1.4
Glider Launcher Bucket Assembly



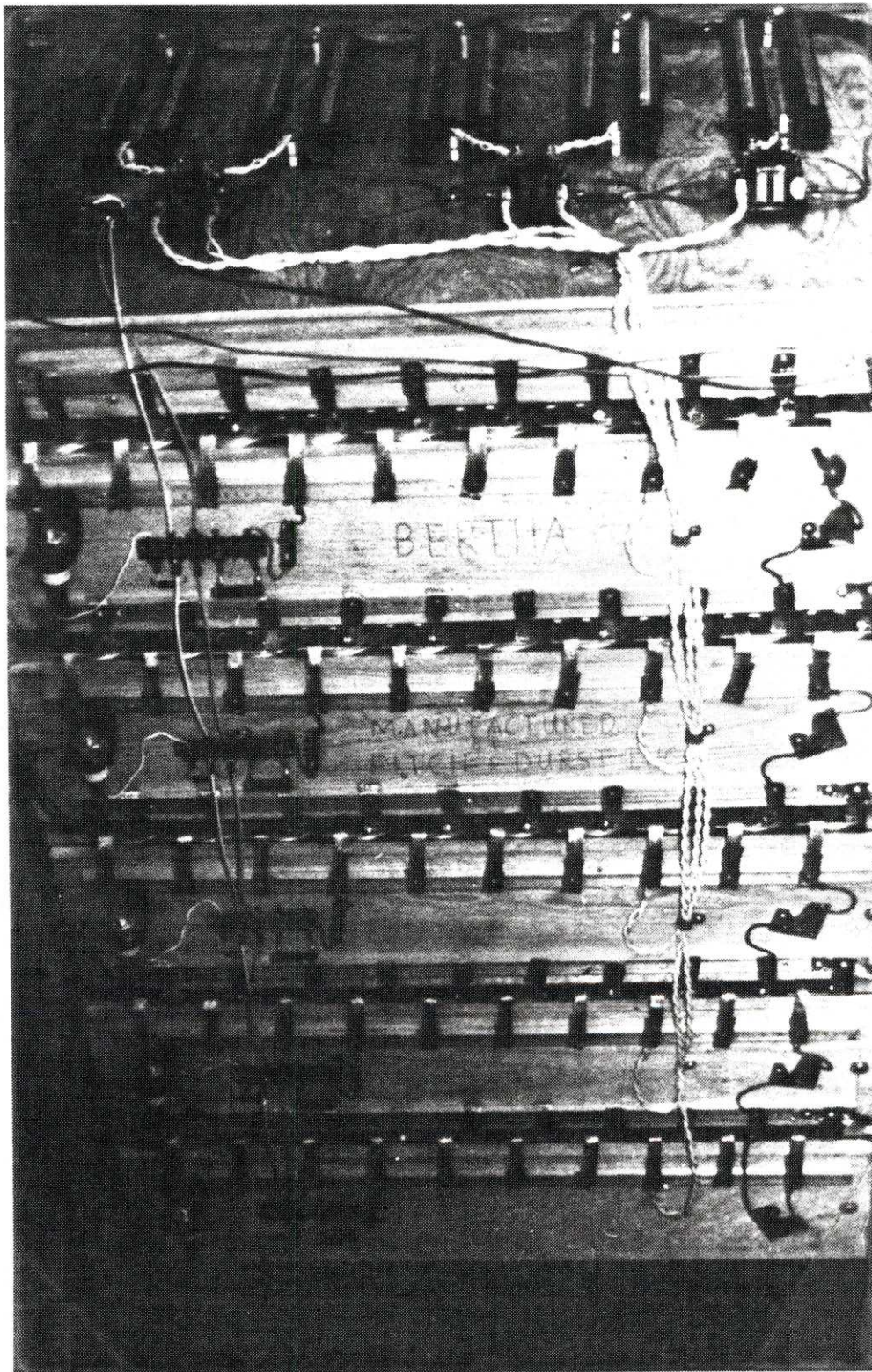
III.2.2. Capacitor Banks

The power source for the glider launcher was four one-farad electrolytic capacitor banks (one of which is shown in Figure III.2.2.1), which were SCR switched and capable of being discharged independently. Each bank was constructed by assembling racks of capacitors into shelves and the shelves into banks. Each rack contained eight beer can sized electrolytic capacitors, rated at 2500 microfarads and 350 volts, which were wired in parallel. Ten racks were then wired in parallel to produce a shelf and five shelves then made up an individual bank.

The capacitor banks were capable of being triggered independently by shelf, although in practice they were wired in such a manner that they could only be triggered by bank. Each shelf was provided with two SCR's connected in parallel, capable of standing off 1000 volts and carrying 250 amps rms apiece. Although this gave flexible switching capability, the primary reason for this arrangement (rather than one in which all the SCR's were paralleled at one point to switch the whole discharge current), was to insure that the discharge current would be distributed through all of the SCR's. When an SCR is switched on and is carrying current, the voltage drop across it is very small. If multiple SCR's are connected in parallel, and one happens to be triggered slightly before the others, it will hog all of

Figure III.2.2.1

One Farad Electrolytic Capacitor Bank



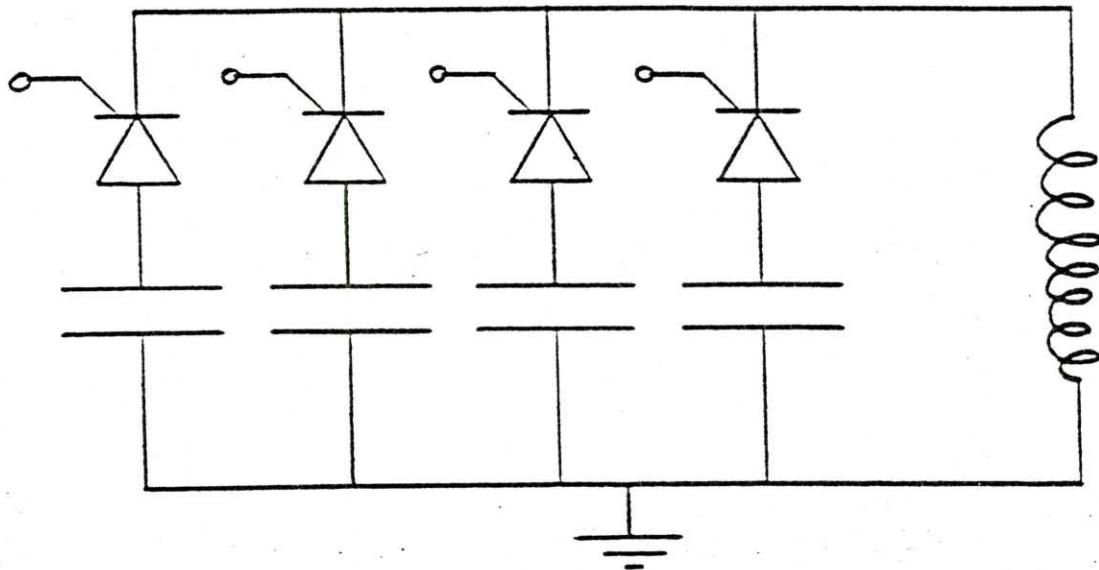
the available current. This removes any incentive for the other SCR's to begin conducting when they are triggered; it may also result in the first SCR being damaged or destroyed if the discharge current is higher than its current rating. Thus, the distributed SCR system requires synchronizing the switching of only the number of SCR's in a subdivision, whereas the fully paralleled SCR system requires synchronizing the switching of all of the SCR's used. (Both are shown in Figure III.2.2.2.)

Another reason to distribute the switching by shelf was to minimize the total energy available to a fault condition, should one occur. For example, should a capacitor can develop an internal short while the bank was charged, all of the capacitors in parallel with the damaged can would discharge through the short, possibly explosively. If the entire one quarter of a megajoule were allowed to discharge through the fault, this would be quite a dangerous condition. However, by distributing the switching, the most energy which could appear across a fault is the total energy of one shelf, which is much smaller, and therefore much safer. Thus, for systems requiring large numbers of SCR's, the distributed system is clearly superior, which is why it was used on the capacitor banks.

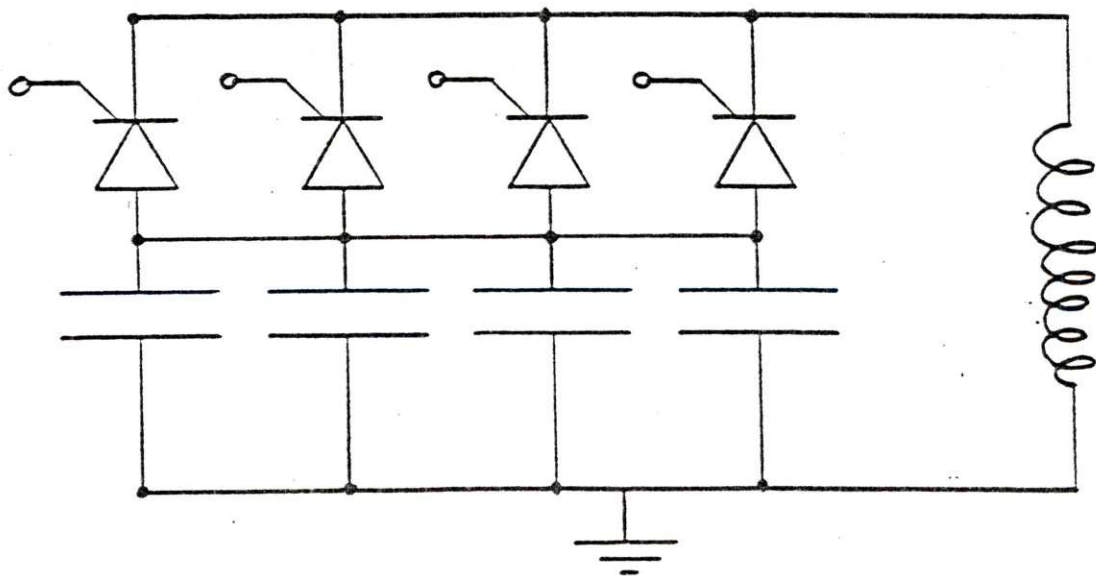
The capacitor banks were actually triggered by smaller capacitor boxes known as trigger boxes. These supplied sharp, high voltage signals to the trigger wires of the SCR's in the banks, in order to insure accurate triggering.

Figure III.2.2.2

Distributed Versus Lumped SCR Switching



Distributed SCR Switching



Lumped SCR Switching

These boxes were SCR switched, actuated by mechanical switches closed by the bucket. (The mechanical switches were made from two strips of sheet copper, placed in the path of the bucket so that it would force them into contact.) Since these switches could be placed at any station along the helix, the discharge current-versus-time profile could be tailored as desired.

One final note about the construction of the capacitor banks is of interest. It was noticed that electrolytic capacitors which had been allowed to sit unused for long periods of time often failed when charged up to their full rated voltage. To prevent this, the banks were "baked in" after construction, by charging them up to some moderate voltage (about 50 volts) and allowing them to hold this charge for an extended period of time (about 24 hours). This reformed the internal oxide layer which provides the voltage standoff capability in electrolytic capacitors; as a result of this action, only two capacitors out of 1600 failed in over 300 shots.

III.2.3. Testing

This section will deal briefly with the testing of the helical rail gun glider launcher, and will focus primarily on the problems and difficulties encountered in trying to get the performance of the system up to the design specifications.

Testing of the helical rail gun glider launcher began in earnest in the winter of 1981, and continued off and on until the system was demonstrated in September 1981. Initially the bucket was tested with a power tether, but the feed rails were soon added which made this unnecessary. The bucket was pulsed using many different staggered triggering configurations for the capacitor banks; however the best performance was obtained when all four banks were connected together and triggered at the breech end of the helix. (At a capacitor voltage of 310 volts, this produced a speed of 65 meters per second, the highest achieved by this device.) This configuration was given up though, because of the extreme acceleration loads it produced, and because of the severity of the helix arcing which it caused. The configuration which gave the best performance at moderate acceleration was two pair of two banks connected together, triggered separately. The first pair was triggered with the bucket stationary at the breech of the helix, while the second pair was triggered by the moving bucket as it reached

the one meter point. During the glider launches, this configuration was used successfully to launch 3.5 kilogram radio controlled model gliders to 40 meters per second for a downfield glide range of 500 meters, and to launch a 1.75 kilogram dart to 55 meters per second for a ballistic range of 300 meters. (All launches were at a 45 degree launch angle.) This last was the best performance obtained with a loaded bucket. Other test results, including the details of an individual shot, may be found in Appendix A, in the paper entitled **Helical Rail Glider Launcher**, by Mongeau and Williams.

III.2.3.1. Experimentally Observed Limits to Performance

In the section on theoretical limits to performance, the ultimate limits of a helical rail gun, thermal, mechanical, and electrical were discussed. In this section the observed limits to the performance of the helical rail gun glider launcher will be described.

The glider launcher was originally conceived of as a one-half scale model of a catapult which would be capable of launching 50 kilogram cargo gliders to 100 meters per second; consequently it was designed to be able to launch 5 kilograms of payload to 100 meters per second. However, although the bucket was found to be easily capable of accelerating 5 kilograms of payload to velocities comparable to that achieved with an unloaded bucket, the highest velocity which we were able to achieve with or without payload was only 65 meters per second. The speed was limited almost exclusively by helix brush arcing, which occurred at current levels much lower than those which would have been permissible had the performance been limited thermally or mechanically.

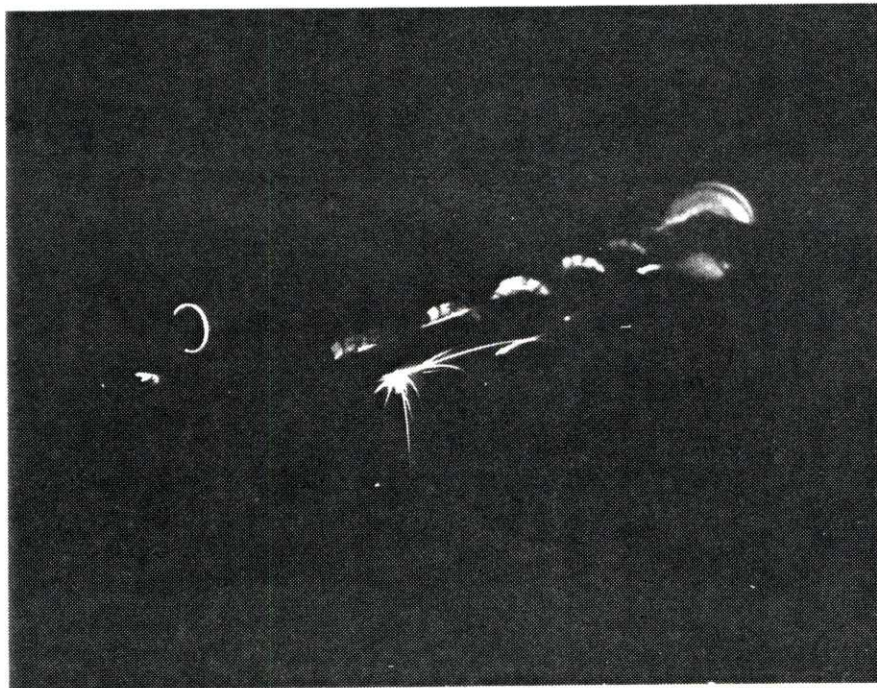
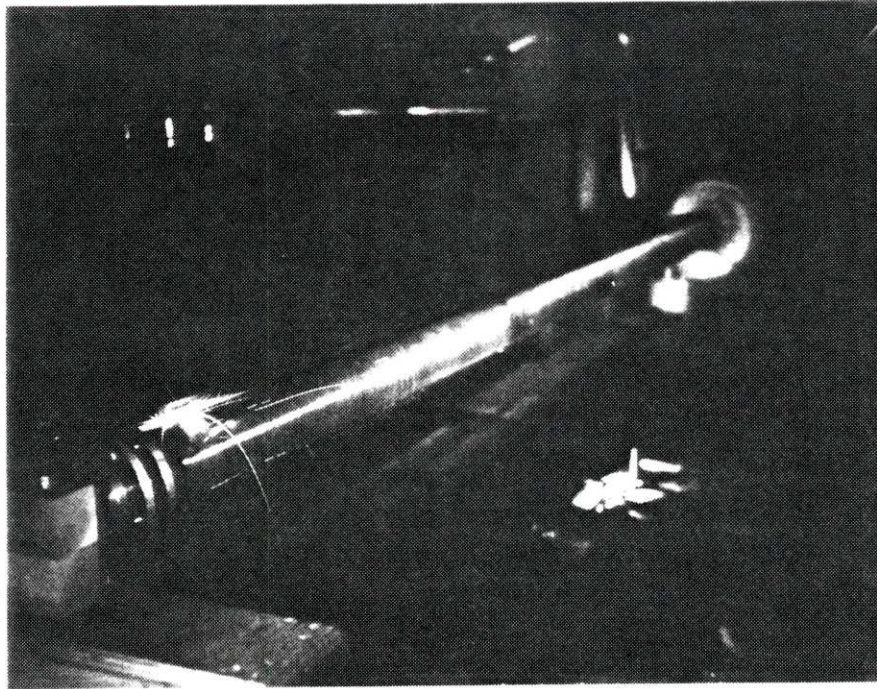
The helix brushes used were standard copper-graphite automobile starter motor brushes. They were $3/4$ inch wide and $1/4$ inch thick, which gave them a contact area of 1.21 square centimeters per brush. There were three leading and three trailing brushes per drive coil, and two drive coils

wired in parallel. Thus the brush current density was equal to the total current delivered by the capacitor banks divided by the total leading or trailing brush area of 7.26 square centimeters. For a typical high performance shot, where the peak delivered current was 5000 amps, the brush current density was 689 amps per square centimeter. (This typically produced a bucket velocity of 40 to 50 meters per second and corresponded roughly to the onset of heavy brush arcing.)

The brush arcing produced two effects which decreased the usefulness of the accelerator. The first was severely degraded brush life; the second was performance below that predicted by theory, due to arcs shorting out portions of the desired current path.

The brush life was severely affected by the length and severity of the brush arcing. In the most extreme case of brush wear which was observed during the tests, new helix brushes wore 1/4 inch in only three shots. The peak currents for these shots were between 7000 and 8000 amps (giving brush current densities of approximately 1000 amps per square centimeter), and a duration near this peak level of about 10 milliseconds. In each case the resulting peak speed was near 60 meters per second, with severe helix arcing lasting the duration of the shot (that is, the bucket arced continuously as it accelerated along the helix.) This type of continuous arcing is illustrated in Figure III.2.3.1.1, which is a photo of a shot of this type. In contrast, when the peak currents were limited to 3000-4000 amps, with

Figure III.2.3.1.1
Continuous Severe Helix Arcing



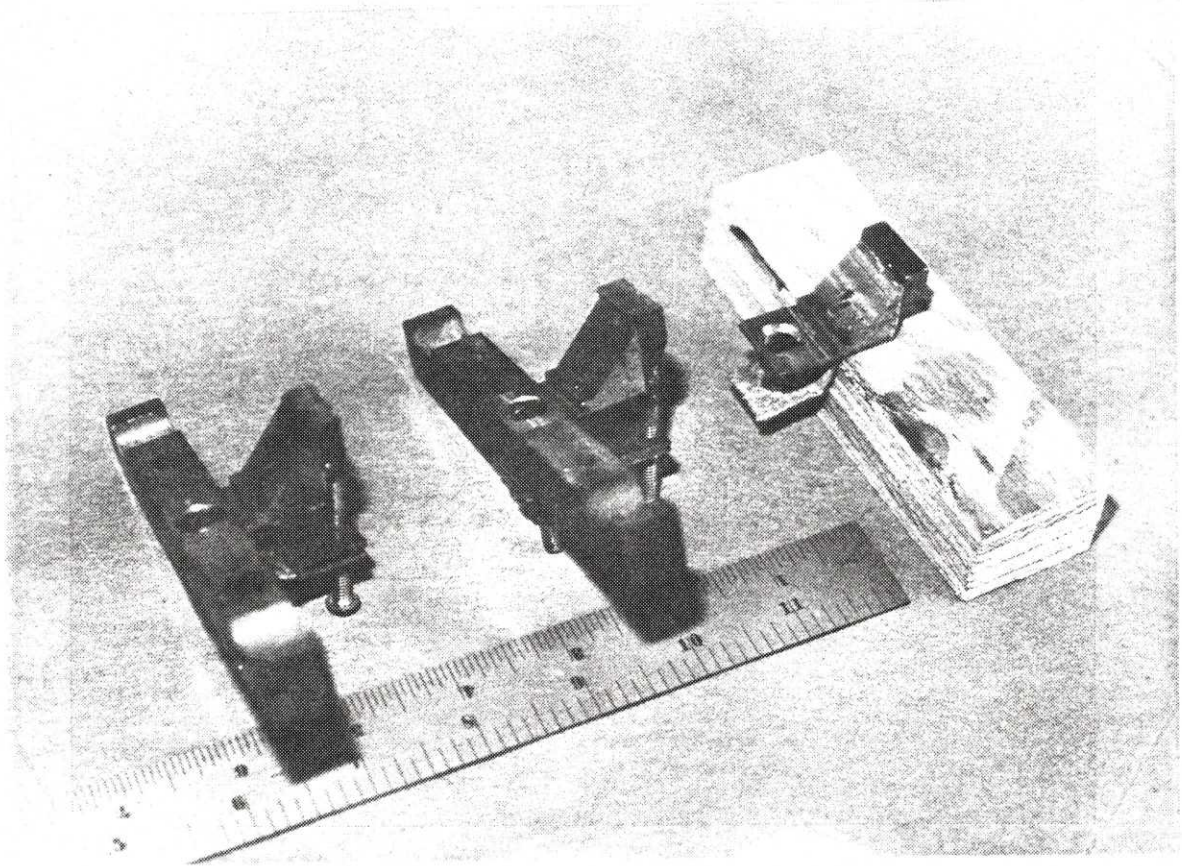
corresponding velocities near 40 meters per second, little to no arcing was observed, and brush wear at the end of 20 shots was less than 1/16 inch. A drag test was also performed, where a new set of helix brushes were installed but not connected electrically. No noticeable wear was evident in this case.

As mentioned in the theoretical analysis section, the leading brush arcs were much worse than the trailing brush arcs. The two burned brushes shown in Figure III.2.3.1.2 were installed new in the accelerator at approximately the same time. After a series of shots they were removed. As can be seen by comparing them with the new brush, the leading brush has worn at approximately twice the rate of the trailing brush.

In addition to affecting brush wear, brush arcing also affected the accelerator's ability to accelerate smoothly. Once arcing began, the current in the brush tended to flow through the arc which formed on the trailing edge of the brush. As the bucket speed increased, the length of the arc increased, causing the current to bypass more and more of the turns in the drive coil, reducing the acceleration of the bucket. (Taken to an extreme, the arc would actually leap from the leading brush to the trailing brush in a commutator flash-over, resulting in no current flowing in the drivecoil at all.) The energy dissipation in the arcs also resulted in an increased effective circuit resistance, which further reduced the performance.

Figure III.2.3.1.2

Leading and Trailing Helix Brushes



Leading
Brush

Trailing
Brush

New
Brush

III.2.3.2. Fault Conditions

There were four basic fault conditions observed in testing the helical rail gun glider launcher: arcing between the bucket coil and the helix; damage to the bucket or payload due to extreme acceleration; damaged or destroyed SCR's; and damaged capacitors. Although not all of these fault conditions would occur in every helical rail gun system, they occurred often enough in the testing of the glider launcher to significantly delay progress, and will be discussed here.

Arcing between the bucket coil and the helix was observed twice during testing. In both cases the bucket coil had been wound without insulation on the inner diameter in an effort to achieve tighter coupling and greater performance. However this left the inner diameter of the bucket coil insulated from the helix by only a thin layer of epoxy and the insulation on the bucket coil wire. Then, as the inner diameter of the bucket coil was subjected to frictional wear by the helix, this insulation thickness eventually decreased to the point where arcing occurred, so that the bucket coil had to be replaced. This problem was solved by insulating the inner diameter with a strip of 20 mil thick G-10. Because the magnetic coupling used in the mass-driver equation is an average over the two coil cross-sections, the effect on the performance of adding the insulation was

negligible.

Extreme acceleration loads caused the accelerator to malfunction on at least three occasions. As mentioned previously, the first bucket was unable to function properly because the extreme rigidity of the helix brush supports caused them to break off under acceleration. Also, the feed rail brush support broke under acceleration after it had been lightened by drilling holes in it. (It was subsequently repaired by epoxying thin G-10 sheets over the holes, which strengthened it considerably without adding significant weight. No further problems were noted subsequently.) And finally, in an initial launch test of the gliders, structural members inside a glider broke free under acceleration, resulting in loss of control and the glider crashing. However, this was later discovered to have been caused by a design miscalculation, which, when corrected, solved the problem. (These gliders were designed to be able to handle an acceleration of 100 g's, which they did flawlessly. Even repairs due to flight test crashes withstood acceleration by the glider launcher. See the excellent thesis by Marc Zeitlin for more details on the design and construction of these gliders.) Because of these incidents measures were taken to reduce the acceleration loads on the bucket and payload.

The damage due to acceleration loads was caused primarily by the peak acceleration produced by the launcher, while the performance depended on the average acceleration. For a typical shot (see Appendix A), a final velocity of 30.5

meters per second was reached in a distance of 3 meters. This corresponds to an average acceleration of 155 meters per second squared. However, for that same shot the peak acceleration was 710 meters per second squared. Thus there was ample room to reduce the loads caused by peak acceleration without affecting performance.

This was done by staggering the triggering of the capacitor banks to distribute the peak current over many smaller pulses, and by adding an inductor to the circuit to increase the width of an individual pulse. Staggering the triggering of the banks did distribute the current and have the desired effect; however, under identical conditions it was found that the use of an inductor large enough to compensate for the extreme acceleration tended to degrade the overall performance of the accelerator, due to the fact that the LC time constant was longer than the acceleration time.

One condition which was noticed during staggered trigger testing was voltage left in the capacitor banks after a shot. It became apparent that the SCR's in a capacitor bank could be turned off by the discharge of another bank. This was due to the fact that the sudden rise in voltage across the accelerator due to the firing of the second bank would cause the voltage drop across the SCR's of the first bank to become momentarily negative, turning them off. This problem was solved by increasing the pulse length of the trigger boxes, so that the SCR's were continuously triggered over

the length of a shot.

The inductor was found to successfully decrease the peak current and broaden the length of a pulse, but as previously noted turned out to be of little help in the end. The inductor consisted of varying number of turns of heavy gauge welding cable, loosely coiled in a two-foot diameter circle. The number of turns varied from 5 to 20, with the inductance varying from 36 to 575 microhenries. For comparison, the inductance of the accelerator alone was 40 microhenries, and the inductance of the accelerator plus the leads to the capacitor banks was 79 microhenries.

The other two fault conditions concern the capacitor banks used as a power source, rather than the accelerator itself. The first was SCR failure, where due to various conditions the SCR's used to switch the capacitor banks were damaged or destroyed during a shot. Usually the SCR's failed in the deceleration bank (i.e. the bank triggered just as the bucket reached the deceleration section, used to stop the bucket) since the bucket entering that section at high speed generated large reverse voltages, which drew large currents out of that bank. Since these failures presented a hazard to both safety and progress, the major classes of SCR failure which were observed in testing will be described here.

The SCR's in the capacitor banks were observed to fail in six distinct ways: blown open; blown shorted; marginal failure with spontaneous triggering at low voltages; marginal failure with spontaneous triggering at high

voltages; marginal failure requiring higher than normal levels of trigger signal for proper operation; and failure resulting in visible damage to the SCR. (By marginal failure I mean damage which was not immediately obvious upon testing the SCR for failure.) The first two failure modes, blown open and blown shorted, were relatively easy to detect and relatively safe, since on the next shot the shelf where the fault occurred would either refuse to discharge or to charge, respectively. In either case pre-triggering was not a problem. However, the next two failure modes were particularly insidious. Up to a certain voltage the failed SCR's would behave like a normal SCR. But when that voltage was reached (which was relatively constant for an individual SCR, but which varied between them), the affected SCR triggered spontaneously. For the low voltage marginal failures this voltage varied from about 15 to 50 volts; for the high voltage marginal failures it varied between 300 and 900 volts. The final two failure modes were the most benign of the six. The higher than normal trigger level failures were difficult to detect or to distinguish from the blown open failures; but once detected, they only required modifying the particular trigger box to place them back in service. The visible failures were immediately detectable, since they consisted of pinhead-sized holes burned in the case of the SCR, often accompanied by material being spewed out. This allowed them to be replaced immediately after failure, rather than after another shot.

The final fault condition observed was damage to the individual capacitors in the banks. Two faults of this kind occurred; in both cases an arc formed between the capacitor plates, destroying the electrolyte in that section and shorting out the capacitor.

III.3. Experimental Testing of Saddle Bucket Feasibility

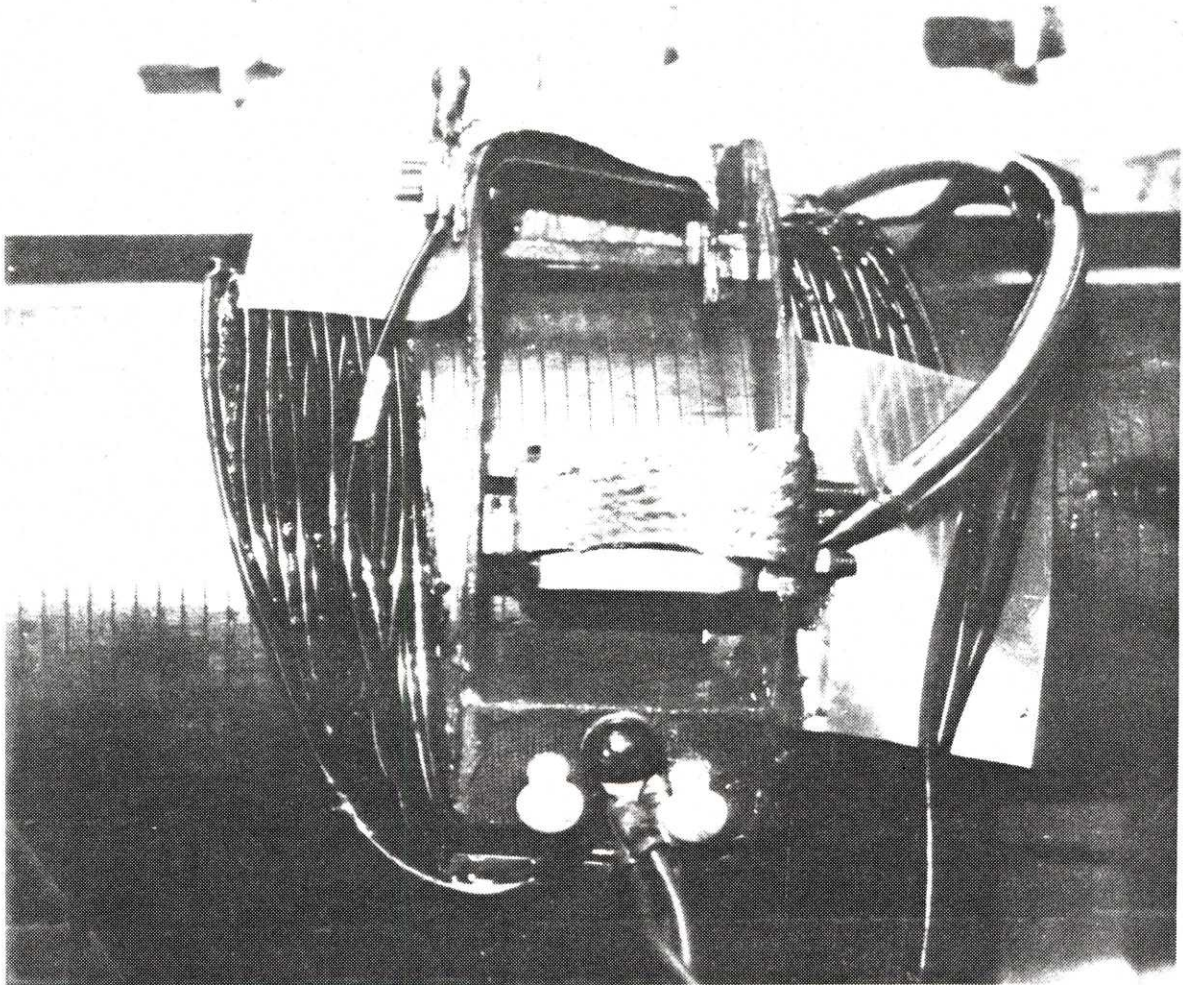
In order to experimentally test the feasibility of saddle bucket equipped helical rail guns, the saddle bucket shown in Figure III.3.1 was constructed. Rather than wind another helix, the original bucket was removed from the 1-meter benchtop helix so that it could be used for this test. The saddle bucket was then constructed directly on the helix.

First the helix was prepared by wrapping a section of it with five layers of heavy brown paper. Each layer was wrapped tightly around the previous layer and taped to itself so that five independent loops resulted. This allowed the saddle coil to be wound around the helix tightly, but still have sufficient clearance for removal and operation. Two circular annuli of 1/16 inch G-10 were then made, having an annular thickness of 1 inch, and an inside diameter which fit snugly over the paper covered helix. A quarter of their circumference was then cut away, leaving two "C" shaped pieces. Three rectangular blocks of phenolic were then epoxied between them, one at either end of the "C" and one in the middle, to form a two inch gap. This was the space for the helix brushes. This assembly was then slid over the helix and onto the paper, and allowed to cure.

Next, the saddle coil was wound. 1/10 inch round, dead-soft, aluminum wire was used for this because it was easy to work with and on hand. At first it was attempted to wind the

Figure III.3.1

Saddle Bucket Helical Rail Gun
(After Destructive Testing)



turns of the coil into an ordered pattern and epoxy them as they were being wound. However this proved to be impractical so the coil was jumble wound dry. Thirty turns were wound around the G-10 and phenolic frame and then epoxy was poured over the windings and allowed to cure.

Finally the bucket was removed from the helix and the brushes, leads and other details were added. The top few layers of paper had become soaked with epoxy and glued to the inside surface of the coil; this added additional insulation between the bucket coil and the helix, while allowing the bucket to be slid off the bottom few layers. All extraneous paper was then trimmed away. The bearing surfaces were added by drilling and threading two holes in each of the three phenolic blocks, to which were added nylon bolts. These nylon bolts could be screwed down until they made contact with the helix, which allowed the bucket to slide on nylon rather than the inside surface of the bucket. The helix brushes were made by soldering and bolting copper-graphite brushes to pieces of tinned copper braid and pieces of stainless steel shim stock. The stainless steel pieces were then bent and attached to the frame so that they would apply spring pressure to the brushes as they contacted the helix. The jumper wires were attached to the pieces of copper braid electrically, the tether was connected and the bucket was slid back onto the helix.

The bucket was then tested to determine what its magnetic coupling was. It was impractical to measure the actual

acceleration of the bucket, since that took place over a distance of only about 2 inches, so instead the final velocity of the bucket was measured using a wire-break velocity meter. This was then compared with the time integral of the current squared to determine the total impulse and thus dM/dz , the magnetic coupling. The results of these tests are shown in Table III.3.1; the magnetic coupling found was $\langle dM/dz \rangle = 0.92$ micro-henries per meter, which is normalized for the number of turns in the bucket and drive coil. This is comparable to other coaxial devices of this scale size, for example the glider launcher, which had a coupling of $\langle dM/dz \rangle = 1.5$ microhenries per meter.

The saddle bucket was then tested to destruction. At a peak current of 1900 amps, the front G-10 "C" delaminated from the middle phenolic spacer block with a loud crack, and was forced forward about 1/2 inch. The bucket was repaired by epoxying the two pieces back together, and adding two small wood screws for reinforcement. The bucket was then tested three times in succession at a peak current of 1600 amps. After each of these shots the bucket became progressively looser and "sloppier" on the helix, requiring the nylon bolts to be tightened. Finally, on the third shot, the front conductor delaminated again, this time with the windings delaminating from the G-10. This time the damage could not be so easily repaired, which brought the testing to an end.

Table III.3.1

Saddle Bucket Data and Experimental Results

Saddle Bucket Mass = 810 grams

Number of Saddle Turns = 30

Number of Drive Coil Turns = 12

Tether Mass = 455 grams

Capacitor Bank Data: Capacitance = 80 millifarads
 Voltage Rating = 900 volts
 Energy Storage = 32 kilojoules
 Electrolytic, SCR Switched

Test 1: Bank Voltage = 300 volts
 Peak Current = 1628 amps
 Peak Time = 3.02 milliseconds
 Integral I^2dt = 2.62×10^4 amp² seconds
 Peak Measured Speed = 7.3 m/s
 Calculated Coupling = 0.774 microhenries per meter

Test 2: Bank Voltage = 300 volts
 Peak Current = 1628 amps
 Peak Time = 3.00 milliseconds
 Integral I^2dt = 2.59×10^4 amp² seconds
 Peak Measured Speed = 8.55 m/s
 Calculated Coupling = 0.916 microhenries per meter

IV. Helical Rail Gun Design Considerations

IV.1. Motivation For The Design Of New Helical Rail Gun Systems

Up to this point, this thesis has been primarily concerned with the theoretical analysis of existing helical rail gun systems. This is fine if one is only interested in existing devices, but it is of limited use if one is trying to design a new helical rail gun to perform a given task, since the information is haphazardly presented. The presentation of a systematic method of design using the theory previously presented is one of the purposes of this chapter.

Why would anyone want to design a new helical rail gun? What are they good for? As mentioned in the introduction, helical rail guns excel at accelerating relatively large masses (kilograms to tonnes) to moderate velocities (zero to hundreds of meters per second). Also, since helical rail guns are energized electrically, they can be used whenever electric power is available, making them highly suitable for many applications. These applications cover a wide range, including the launching of military fighter aircraft, assisting commercial jetliners on take-off, launching remotely piloted vehicles or pilotless drones, expelling torpedoes from torpedo tubes, "cold-launching" nuclear

missiles from their silos, opening sliding doors in Star-Trek fashion, and even exotic possibilities such as certain orbital transfer missions. Each of these possibilities will be considered briefly below, and then the remainder of the section will be devoted to those with the most promise.

The launching of military fighter aircraft is an application which immediately comes to mind when the catapult-like properties of helical rail guns are described. Currently all of the fixed wing aircraft deployed on US Navy aircraft carriers are routinely launched by steam catapults, and it is a relatively easy task to design a helical rail gun catapult which could directly substitute for the existing system. Other similar military tasks include launching Air Force fighters directly from armored hangars to prevent their being attacked while taking off, and launching vertical take-off and landing aircraft, such as the Harrier, from the helicopter pads of destroyers so as to extend the aircraft's combat radius.

Assisting commercial airliners during take-off is another task to which helical rail guns are suited. In order to save fuel, helical rail guns could be built into the runways of airports, and used to slowly accelerate aircraft to take-off speed, either at reduced engine RPM or at reduced take-off distance.

Launching remotely piloted vehicles (RPV's) is a good application of helical rail guns, and in fact has been experimentally demonstrated by our model glider launcher.

Scaling up the glider launcher slightly to handle larger, powered RPV's presents no technical problems.

Helical rail guns could also be adapted to eject torpedoes from torpedo tubes, or intercontinental nuclear missiles from their hardened silos. In ejecting torpedoes, no bubbles would be produced, since compressed air would no longer be needed, although the many problems associated with operating in a salt water environment would have to be solved. In ejecting nuclear missiles from their silos, helical rail guns in the bore of the silo would be used to provide a "cold launch" for the missile. "Cold launching" missiles involves igniting their rocket engines in the air above the silos after they have been thrown out by some outside agent. Compared to the normal method of launching missiles, where the rocket engines are ignited in the silos, cold launching damages the silos very little, allowing them to be reloaded and used again.

On a more mundane level, helical rail guns can also be used to produce Star-Trek type sliding doors. By hiding the helix inside a wall and attaching the bucket to the door by means of a push-rod, a brief pulse of current can be used to accelerate the door. Then when the door is fully open (or closed) another pulse of current decelerates and stops the door.

The final application is more exotic and less immediately realizable. A large bore helical rail gun could be placed in low earth orbit and used as the first half of an upper stage for satellites put into orbit by the space shuttle. The

helical rail gun would accelerate these satellites to transfer orbit speeds, and the rocket engines normally carried onboard such satellites would circularize the satellite's orbit at the desired altitude. Meanwhile, highly efficient ion engines would recircularize the orbit of the helical rail gun in the days or weeks between shots. This application is highly dependent on brush technology however, since present technology electrical brushes fail at speeds approaching one kilometer per second, and orbital transfer missions typically require velocity changes of two to three kilometers per second.

The above list of applications is by no means exhaustive, and with a little thought could be extended considerably. However, it does tend to delineate the major classes of use, and therefore it will suffice for the task at hand; to wit, finding the best near term applications for helical rail guns. Examining the list, three applications appear to be the most immediately useful: launching aircraft, either military or commercial; cold launching nuclear missiles; and launching RPV's or drones.

As stated previously, launching RPV's has already been demonstrated, and scaling up the existing glider launcher with slight modifications to handle operational RPV's presents no technical problems. Therefore this problem will not be considered further.

Although the two remaining applications appear to be worthy of independent analyses, it turns out that both are

very similar design problems. For example, the Navy's top fighter, the F-14, masses 27 tonnes fully loaded at take-off and is launched from carriers at speeds up to 80 meters per second. On the other hand, the front line US intercontinental ballistic missile, the Minuteman 3, masses 35 tonnes, and if launched from its silo at 80 meters per second would rise 320 meters into the air. Since this is more than sufficient for a cold launch, it is apparent that the design techniques used to design aircraft launchers carry over to the design of nuclear missile launchers, and therefore aircraft launchers alone will be considered here.

IV.2. Design Method And Point Designs For Helical Railguns

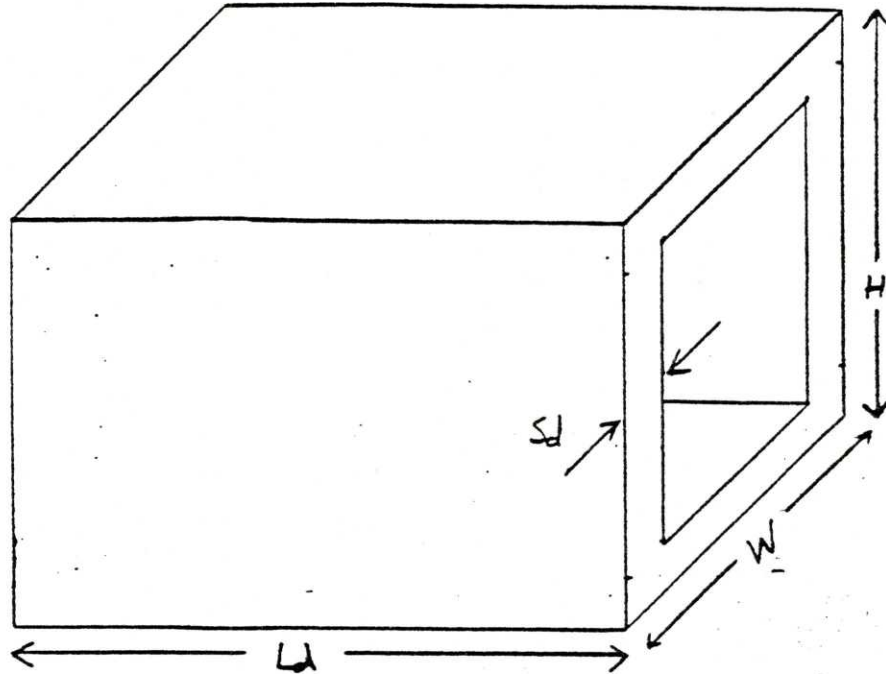
This section will describe a systematic method for the design of helical rail guns, given certain design parameters and constraints as initial conditions. This will be followed by an example of the design method, in which the parameters of a point design for a helical rail gun replacement for the current Navy steam catapult system will be worked out in detail. Finally, the parameters for three other helical rail gun point designs will be given: an Air Force fighter launcher, for installation in armored hangars; a VSTOL fighter launcher for deployment on the helicopter pads of destroyers; and a catapult to assist commercial airliners on take-off.

IV.2.1. Design Method

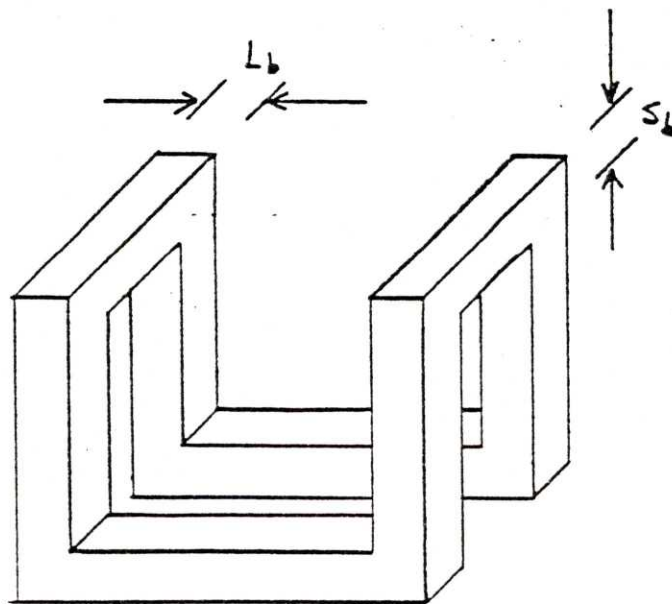
The design method presented here assumes that the helical rail gun being designed is to be used for aircraft launching. Consequently, it assumes that the accelerator is based on a rectangular geometry and uses a rectangular saddle bucket. It also assumes that the bucket is not mass limited, that is that the mass of the bucket will turn out to be much smaller than the mass of the aircraft being launched. If these assumptions are made, then it becomes a relatively easy task to optimize the accelerator for maximum efficiency, which is presented in detail in Appendix C. This design method is the result of that optimization. The following conventions are used throughout: L refers to the axial extent of the cross-section of a coil; S refers to the build of a coil; H refers to the height of the helix; W refers to the width of the helix; and the subscripts b and d refer to the bucket and drive coils, respectively. Also, any quantity which has been starred, such as L_d^* , means that that quantity has been normalized with respect to the width of the helix, W. Figure IV.2.1.1 illustrates these basic conventions. With this in mind then, the optimization consists of the following steps:

- (1) Determine which of the design parameters given below are specified or constrained: force (F),

Figure IV.2.1.1
Basic Dimensional Conventions



Drive Coil



Bucket Coil

final velocity (V_f), payload mass (M_p), launcher length (d), maximum acceleration (A_{max}), launch duration (τ), and maximum kinetic power (P_{max}).

- (2) Determine the remaining parameters by using Newton's laws. If the system is overspecified or underspecified, straighten out any conflicts, picking reasonable values as necessary.
- (3) From knowledge of the task to be performed, pick the kind of conductors to be used in the bucket and the helix (usually copper), and pick the height to width ratio of the helix (usually 1.5; see the discussion of the effects of geometry in the theory section.) Also pick a value for the largest acceptable width of the helix, W .
- (4) Using Figure IV.2.1.2, find the point of maximum \emptyset , subject to the constraint that the geometry of the drive coil must allow for the difficulty of winding very flat wire edge on. For example, if L_d/S_d were taken equal to five, then the drive coil could be wound from ten turns of wire having the same normalized cross-section as a two-by-four; that is wire which has a height to width ratio of 2. This wire can be wound edge on, but flatter wire would be more difficult. Thus, in lieu of specific information about the problem at

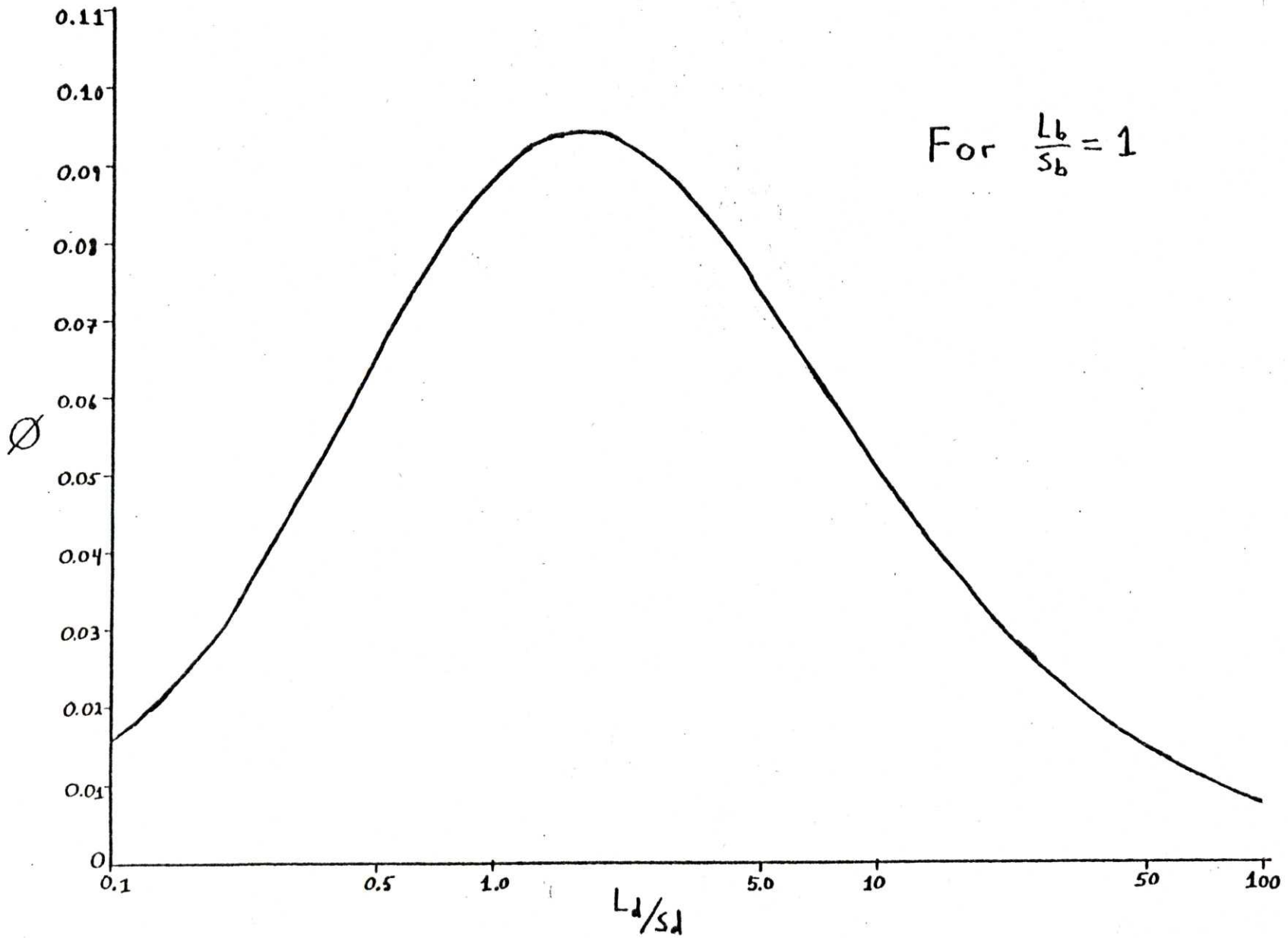


Figure IV.2.1.2
 \emptyset Versus L_d/S_d

hand, it is probably best to assume $L_d/S_d = 5$, yielding $\emptyset = 0.0725$.

(5) Now determine the drive coil parameters which maximize the efficiency of the accelerator.

In order to keep $S_d^* < 1/2$, \emptyset must be limited to $\emptyset < (L_d/S_d) q^2 / 4$, where

$$q^2 = (\sqrt{L_d/S_d} + \sqrt{L_b/S_b})^2 + (\sqrt{S_d/L_d} + \sqrt{S_b/L_b})^2 \quad \text{IV.2.1.1}$$

and

$$\emptyset = A_b^* q^2 \quad \text{IV.2.1.2}$$

Using Figure IV.2.1.3, which is a plot of the equation

$$Y = \emptyset \left\{ 2 \left[\frac{4H^{*2}}{\emptyset} + 1 \right]^{1/2} + \left[\frac{4}{\emptyset} + 1 \right]^{1/2} - 3 \right\} \quad \text{IV.2.1.3}$$

determine the maximum possible value of Y , based on the maximum value of \emptyset calculated above. Then,

$$A_b^* \frac{dM}{dz} = 4(\mu_0 / 4\pi) \emptyset Y \quad \text{IV.2.1.4}$$

and

$$r = \frac{V_f W A_b^* \frac{dM}{dz}}{4 \sqrt{\rho_b \rho_d} \sqrt{(H^*+1)(2H^*+1+L_d^*)}} \quad \text{IV.2.1.5}$$

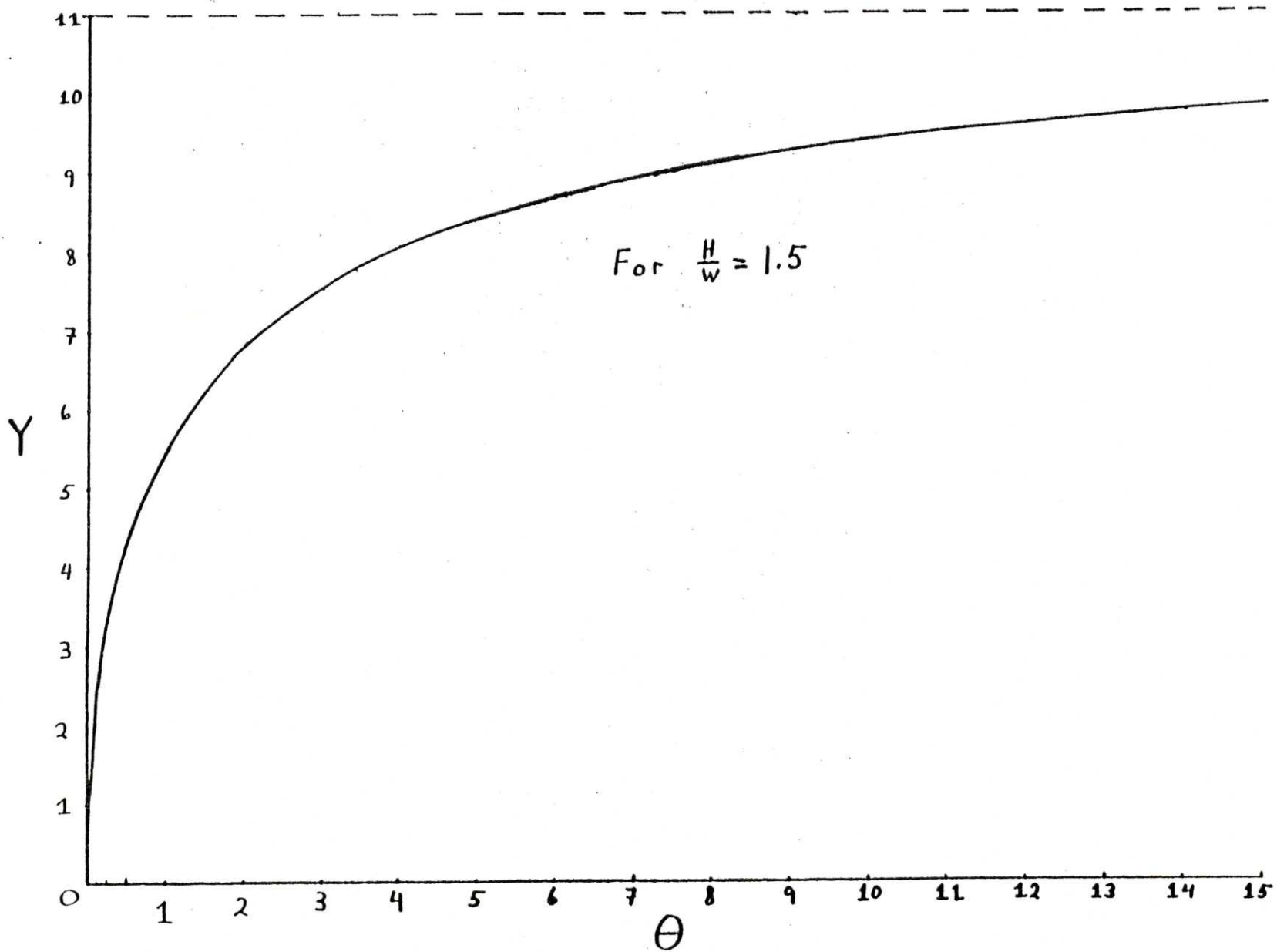


Figure IV.2.1.3
Y Versus θ

where r is the ratio of the final velocity to break point velocity, V_f/u , and is the argument of the efficiency functions plotted in Figure IV.2.1.4. (The figure is a repeat of Figure II.3.1). Thus, by cross-indexing r on the figure, the maximum efficiency deliverable by the accelerator can be determined.

- (6) In order to increase the performance of the accelerator, decrease r to as low a value as possible without decreasing the value of η significantly. Now calculate a new value for

$$A_b^* \frac{dM}{dz} = \frac{4 r \sqrt{\rho_b \rho_d} \sqrt{(H^*+1)(2H^*+1+L_d^*)}}{V_f W} \quad \text{IV.2.1.6}$$

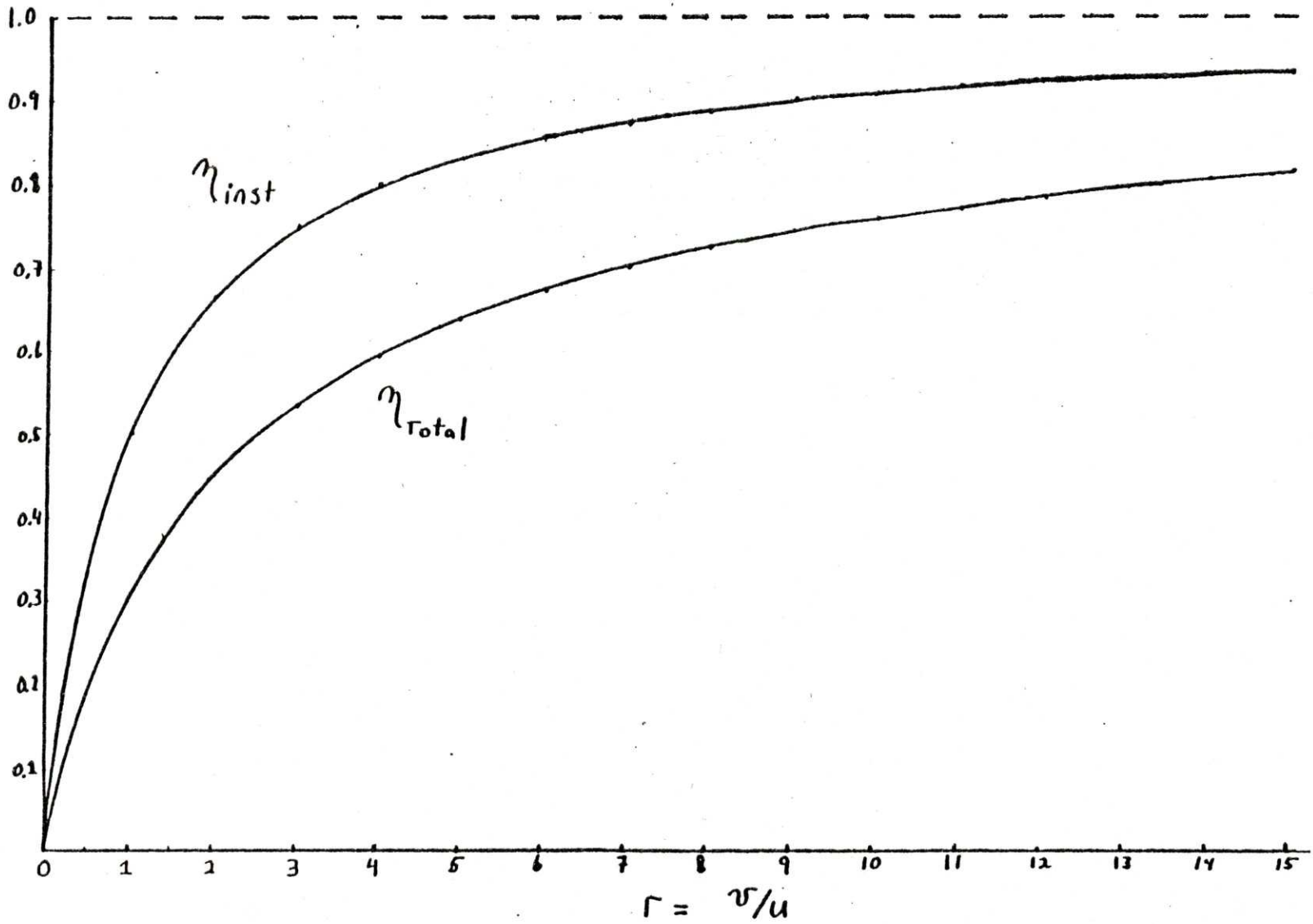
and then

$$Y = \frac{A_b^* \frac{dM}{dz}}{4 (\mu_0/4\pi) \phi} \quad \text{IV.2.1.7}$$

On Figure IV.2.1.3 cross index this value of Y to find a new value for θ . (If Y is too small to be effectively read off of the curve, the approximate formula

$$\theta = Y^2 / \{4H^* + 1\}^2 \quad \text{IV.2.1.8}$$

Figure IV.2.1.4
Instantaneous and Total Efficiency



may be used to obtain a value.) Now calculate a new value for A_b^* using Equation IV.2.1.2, and new values for L_d^* and S_d^* , using

$$L_d^* = \sqrt{A_b^* (L_d/S_d)} \quad \text{IV.2.1.9}$$

and

$$S_d^* = L_d^* / (L_d/S_d) \quad \text{IV.2.1.10}$$

(7) The constraints on the bucket current density should be calculated as,

$$J_{b\max} < \sqrt{\frac{C_v \Delta T}{\rho_b \tau}} \quad \text{IV.2.1.11}$$

and

$$J_{b\max} < 2 \alpha \left(\frac{H^*+1}{S_d^*} \right) \sqrt{\left(\frac{\rho_d}{\rho_b} \right) \frac{(H^*+1)}{(2H^*+1+L_d^*)}} J_{\text{brushmax}} \quad \text{IV.2.1.12}$$

where C_v is the volume specific heat of the bucket conductor, ΔT is the allowable bucket temperature rise, α is the fraction of the circumference of the helix in contact with the brushes, J_{brushmax} is the maximum allowable brush current density, and where the two equations are the limits on bucket current density due to adiabatic heating of

the bucket and due to limits on brush current density respectively. $J_{b\max}$ should be limited to the smaller of the two.

- (8) The number of buckets needed can now be calculated from

$$N_{\#min} = \frac{F}{(J_{b\max})^2 (A_b^*) (A_b^* \frac{dM}{dz}) \sqrt{\left(\frac{\rho_b}{\gamma \lambda}\right) \frac{(2H^* + 1 + L_d^*)^2}{(H^* + 1)}} W^4} \quad \text{IV.2.1.13}$$

which is nothing more than the mass-driver equation rewritten. The value of $N_{\#min}$ found should be rounded up to the next largest integer. There are now two extreme cases to be considered:

- (A) If $N_{\#min}$ is excessive (if it is 100 for example), then the most potent way of bringing it back down to a reasonable value is to increase W . If this is impossible, or if it is desired to also increase the efficiency, the number of buckets can be decreased by increasing r (since $N_{\#min} \sim 1/r$ for brush limited current densities, and $N_{\#min} \sim 1/r^3$ for thermally limited current densities). This process has a limit, however, in that r can only be increased to its maximum limit, found above. Finally, the number of buckets can be reduced by relaxing the constraints on the bucket

current density.

(B) If $N_{\#min}$ is small, then the scale size of the accelerator can be decreased if desired.

(9) Generate a dM/dz map for the drive coil dimensions which are now fixed. A dM/dz map is a table which gives values for the mutual inductance gradient between the drive coil on which the map is based, and an imaginary current filament placed at regularly spaced grid locations around the coil. The computer program BMAP, contained in Appendix A, generates such a map for saddle wound filaments around rectangular drive coils. (Note that if desired, dM/dz maps may be made dimensionless, since the basic equations are scale size independent.) Finally, fit A_b to the dM/dz map, so as to maximize the magnetic coupling but also allowing space for real clearances. This determines the bucket coil dimensions, L_b and S_b .

(10) The fine details of the geometry of the bucket and drive coil, such as the number of turns in each, can now be specified. The optimized turns ratio is

$$N_d/N_b = \sqrt{\frac{R_b^{\circ}}{R_d^{\circ}}} \quad \text{IV.2.1.14}$$

where R_b° and R_d° are the single turn resistances

of the bucket and drive coils, respectively (that is those resistances which would be measured if the whole cross-section of the coil were filled with a single large turn of wire). They can be calculated as

$$R_d^{\circ} = 2 \rho_d (W + H) / A_d \quad \text{IV.2.1.15}$$

and

$$R_b^{\circ} = 2 \rho_b (L_d + W + 2H) / A_b \quad \text{IV.2.1.16}$$

where ρ is resistivity, W is the width of the helix, H is the height of the helix, and L_d is the axial dimension (length) of the drive coil.

- (11) The size of the power supply must now be specified. The maximum kinetic power was determined in step (2), but the total power needed is the sum of the maximum kinetic power and the resistive power dissipated. The resistive power loss is the sum of the power being dissipated in the bucket and the power being dissipated in the drive coil, but by designing for maximum efficiency we have forced these two to be equal. Thus the resistive power is just twice the quantity $R_b^{\circ} A_b^2 J_b^2$ times the overall number of

buckets in the device.

- (12) The actual number of turns in the device is found by matching the impedance to the requirements of the power supply to be used. First the maximum power is divided by the number of buckets to get P_b . Then a reasonable voltage drop per bucket, ΔV , is picked and the current flowing into each bucket, I , is found by dividing P_b by ΔV . The bucket resistance is then

$$R_b = R_b^o A_b^2 J_b^2 / I^2 \quad \text{IV.2.1.17}$$

and the number of turns in the bucket

$$N_b = A_b J_b / I \quad \text{IV.2.1.18}$$

The number of turns in the drive coil is then calculated using Equation IV.2.1.14; together these determine the size of wire to be used in winding the helix and the bucket coil.

IV.2.2. Design Example: Replacement Navy Catapult

For an example of the method just given, consider the design of a helical rail gun which could be used to replace the steam catapults now in use on Navy aircraft carriers. The present catapults can generate a force of 1.07 million newtons over a distance of 95 meters; fully loaded fighter aircraft can be launched at speeds of up to 85 meters per second. For a fully loaded fighter aircraft massing 30,000 kilograms (which is the approximate gross weight of an F-14) this corresponds to an acceleration of about three and one half g's.

Of the remaining parameters, only the launch duration, τ , and the maximum kinetic power, P_{\max} , are of further interest. (This is due to the fact that we already know the force which must be generated; in designing a force to launch a specific load, one would use the mass and acceleration to find the force.) Assuming constant acceleration the launch duration is

$$\tau = 2 d / V_f = 2.24 \text{ seconds} \quad \text{IV.2.2.1}$$

and the maximum kinetic power is

$$P_{\max} = F V_f = 90.95 \text{ MW} \quad \text{IV.2.2.2}$$

Now pick all the conductors to be copper and pick the height to width ratio to be the standard $H/W = 1.5$. Also, in order to backfit the helical rail gun into the space vacated by the steam catapult, the helix should be limited to a width of about 1 meter. If L_d/S_d is taken equal to 5, and if L_b/S_b is assumed to be roughly equal to 1, then from Figure IV.2.1.1, \emptyset is found to be equal to 0.0725. Using these parameters, the maximum value of θ is found to be 15.71. From Equation IV.2.1.3 this corresponds to a value $Y = 9.87$, and then Equation IV.2.1.4 gives $A_b^* dM/dz = 2.86 \times 10^{-7}$ H/m. Putting it all together yields $A_b^* = A_d^* = 1.25$; $L_d^* = 2.50$; and $S_d^* = 0.50$ for the most efficient possible design.

By Equation IV.2.1.5 these yield a value of $r = 88.7$, with a corresponding maximum instantaneous efficiency of 98.9%, and a total efficiency of 94.9%. These efficiencies are way out on the flat of the curve, so we can afford to trim r and lose very little. If we take $r = 20$, this is still an instantaneous efficiency of 95.2% and a total efficiency of 84.8% so we're still fine as far as that goes. Since reducing r merely reduces $A_b^* dM/dz$ by the ratio $r_{\text{new}} / r_{\text{old}}$, the new value is $A_b^* dM/dz = 6.45 \times 10^{-8}$ H/m; since \emptyset remains unchanged, Equation IV.2.1.7 yields $Y = 2.224$. Now cross-indexing this value on Figure IV.2.1.2 yields a value for θ of 0.10, which can be plugged into Equation IV.2.1.2 to get a new value for A_b^* . Then, using Equations IV.2.1.9 and IV.2.1.10 the new coil dimensions are found to be $A_b^* = 7.96 \times 10^{-3}$, $L_d^* = 0.199$, and $S_d^* = 3.99 \times 10^{-2}$.

At this point it is convenient to state why it was necessary to generate a second design which actually had a lower efficiency than the original design. Since the first design filled the entire volume of the helix with conductor, it should be apparent that it would be impossible to wind a helix in this configuration, although one might be able to construct such a helix by stacking Bitter plates. Also, in the optimization, it was assumed that the helix was of thin build, that is that the thickness of the windings was small compared to the width of the helix. This design certainly is not. Thus, given the constructional difficulties and the uncertainty of optimization, a second design was needed to overcome these.

The two limits on the bucket current are given in Equations IV.2.1.11 and IV.2.1.12. To calculate the thermal limitation, the specific heat for copper is $3.4 \text{ J/}^\circ\text{K cm}^3$, while the resistivity is $1.7 \times 10^{-6} \text{ ohm-cm}$. Because of the need to be able to fire the accelerator rapidly and repeatably (once every two minutes, for as long as an hour) the heating in the bucket must be strictly limited. For this reason choose $\Delta T = 10^\circ\text{C}$. The launch duration is known from above to be $\tau = 2.24$ seconds. Putting all of these together yields an adiabatic heating limit of $J_{b\text{max}} < 2988 \text{ amps/cm}^2$.

To calculate the brush current density limit, we must first determine the helix circumference fraction in contact with the brushes, α . The most this value can be for a

rectangular saddle bucket with $H/W = 1.5$ is 0.8. However a more conservative estimate would allow for less than perfect packing density and structural supports, so we shall assume $\alpha = 0.65$. Also we need a value for the maximum allowable brush current density. Rotary DC electric motors used to propel subway cars commonly handle brush current densities of 15 amps/cm^2 , so it seems reasonable to suppose that our accelerator could successfully operate at that level as well. Plugging these values into Equation IV.2.1.12 yields a maximum allowable bucket current density of $J_{b\text{max}} < 942.8 \text{ amps/cm}^2$. Since the current density in the bucket is limited by the requirements of the brushes (as it almost always is), this lower value should be used in place of the thermal limit.

The number of buckets required to produce the total force required can now be calculated using Equation IV.1.2.13. For our case at hand, this calculation yields $N_{\#min} = 18.09$ which must be rounded up to yield the required number of 19. Although this number is not huge, it is larger than we would like to have (five buckets is much more reasonable to allow for redundancy, and yet still keep the complexity down). The lowest number of buckets possible to us is indeed five if we use the original design which maximized efficiency, but all of the difficulties associated with that prevent us from doing so. Therefore let's choose an intermediate number like ten buckets, and see if a compromise design works better.

With ten buckets, $A_b * dM/dz$ is just twice the value

calculated for the twenty bucket case. Iteration then yields $Y = 4.27$, and from the graph $\theta = 0.47$. The new coil dimensions are $A_b^* = 3.74 \times 10^{-2}$, $L_d^* = 0.432$, and $S_d^* = 8.65 \times 10^{-2}$. Since these are still very much in the thin coil regime this design appears to be superior to the previous one, given that it requires fewer components and has marginally better instantaneous efficiency (97.9% vs 96.2%); however, note the large difference in the bucket masses. For the 19 bucket case, the total mass of moving conductor is 11,304 kilograms, about one third the mass of an F-14. But for the 10 bucket case, the total mass of moving conductor is much larger at 29,505 kilograms, which is comparable to the mass of the planes being accelerated and which therefore invalidates the modeling used. Thus, we are essentially stuck with the 19 bucket case.

A dM/dz map can now be calculated based on these dimensions so that the actual, rather than approximate, performance can be calculated. In the dM/dz map shown in Figure IV.2.2.1, clearances of 1 cm have been assumed all around, although they are lost in the grain of the table in this case. (Clearances become much more important as the scale size is reduced, or as the clearance distance becomes comparable to the build of the coil.) So, for this example, $\langle dM/dz \rangle = 8.58 \times 10^{-6}$ H/m (which is very close to the value of $dM/dz = 8.10 \times 10^{-6}$ H/m that was predicted.) Also, $L_b = 11$ cm and $S_b = 7$ cm are the values which maximize the magnetic coupling, and which should be used. (The desired

Figure IV.2.2.1

Navy Replacement Catapult dM/dz Map

THIS IS A DM/DZ MAP FOR SADDLE WINDINGS AROUND A RECTANGULAR DRIVE COIL. THE TOP ROW REPRESENTS THE FRONT EDGE ($Z=L/2$) OF THE COIL, AND THE LEFTMOST COLUMN REPRESENTS THE DM/DZ VALUES FOR SADDLE FILAMENTS TOUCHING THE SURFACE OF THE COIL ($X=0$).

HELIX WIDTH = 1
 HELIX HEIGHT = 1.5
 DRIVE COIL LENGTH = .199
 WINDING DEPTH = .0399

MATRIX SPACING IS .01

ALL MATRIX VALUES ARE IN MICRO-HENRIES PER METER.

19.43	14.95	12.36	10.58	9.22	8.12	7.22	6.45	5.80	5.23	4.74
16.92	14.43	12.34	10.70	9.40	8.33	7.44	6.68	6.02	5.45	4.96
14.86	13.35	11.84	10.50	9.35	8.37	7.53	6.80	6.16	5.61	5.11
13.20	12.23	11.15	10.09	9.13	8.27	7.50	6.83	6.23	5.69	5.22
11.85	11.19	10.41	9.60	8.81	8.07	7.39	6.78	6.22	5.72	5.27
10.73	10.27	9.70	9.07	8.43	7.81	7.22	6.67	6.17	5.70	5.28
9.80	9.47	9.04	8.54	8.03	7.51	7.00	6.52	6.07	5.64	5.25
9.01	8.76	8.43	8.05	7.63	7.19	6.76	6.34	5.93	5.55	5.19
8.33	8.14	7.89	7.58	7.24	6.87	6.50	6.14	5.78	5.44	5.11
7.73	7.59	7.39	7.15	6.86	6.56	6.25	5.93	5.61	5.31	5.01
7.21	7.11	6.95	6.75	6.51	6.26	5.99	5.71	5.44	5.16	4.90
6.75	6.67	6.54	6.38	6.19	5.97	5.74	5.50	5.26	5.02	4.78
6.34	6.28	6.17	6.04	5.88	5.70	5.50	5.29	5.08	4.86	4.65
5.97	5.92	5.84	5.73	5.59	5.44	5.27	5.09	4.90	4.71	4.52
5.64	5.60	5.53	5.44	5.33	5.20	5.05	4.89	4.73	4.56	4.38
5.33	5.31	5.25	5.17	5.08	4.97	4.84	4.70	4.56	4.40	4.25

bucket coil cross-section is shown on the map bounded by the solid line.)

Now that the bulk geometry of our accelerator is determined, all that is required is to specify the number of turns in the bucket and drive coil. In order to use the optimized turns ratio given in Equation IV.2.1.14 we must determine the single turn resistance of both the bucket and drive coil. These are given by Equations IV.2.1.15 and IV.2.1.16; plugging in the appropriate values yields $R_b^0 = 17.9$ micro-ohm, and $R_d^0 = 10.7$ micro-ohm, which gives an optimum turns ratio of $N_d/N_b = 1.67$.

Finally, the maximum power which must be delivered by the power supply is the sum of the maximum kinetic power and the total resistive power. The maximum kinetic power has already been calculated and is $P_{\max} = 90.95$ megawatts. The resistive power loss per bucket is then $P_{res} = 2R_b^0 A_b^2 J_b^2$; since there are nineteen such buckets, the total resistive power is 3.83 megawatts. Thus the total power which must be supplied by the power supply is just $P_{total} = 94.78$ megawatts. By arranging the buckets in series or parallel, or by changing the number of turns in a bucket, the accelerator can be configured to accept any available combination of voltage and current.

The above parameters are summarized in Table IV.2.2.1.

Table IV.2.2.1

Parameters for Navy Replacement Catapult

Acceleration Parameters:

Force = 1.07×10^6 Newtons

Length = 95 meters

Velocity = 85 meters per second

Catapult Parameters:

Single Boomed

Helix Width (W) = 1.00 meters

Helix Height (H) = 1.50 meters

Number of Buckets = 19

Drive Coil Length (L_d) = 0.199 meters

Helix Winding Thickness (S_d) = 0.0399 meters

Bucket Cross-section Axial Thickness (L_b) = 0.11 meters

Bucket Cross-section Thickness (S_b) = 0.07 meters

Magnetic Coupling (dM/dz) = 8.58 microhenries per meter

Number of Saddle Turns = 8

Number of Drive Coil Turns = 10

Bucket Conductor Mass = 11,304 kilograms

Conductor: Copper

Electrical Parameters:

Power Supply Voltage = 8805 volts

Power Supply Current = 10,765 amps

Delivered Maximum Power = 94.78 megawatts

Brush Current Density = 15 amps/cm²

IV.2.3. Point Design: Air Force Fighter Launcher

As part of the United States' defense commitments, the Air Force currently has fighter aircraft based in Western Europe to deter Soviet attack, or should deterrence fail, to defend against Soviet attack. In order to provide protection against their being destroyed on the ground, these aircraft are based in armored concrete hangars which work as long as the aircraft are inside them. However, in order to take-off and perform its mission an aircraft must taxi a significant distance from the hangar to the runway, where it can gather sufficient speed to become airborne. Typically this process takes a few minutes, and in this time the aircraft is highly vulnerable to being attacked and successfully destroyed, since it cannot defend itself and since it is no longer protected by its hangar. If a means could be found to accelerate the aircraft to flight speed in or near the hangar, however, this vulnerability would be much reduced.

Helical rail guns may be able to provide such a means. If a specially designed helical rail gun catapult were installed in an armored hangar, fighters could be shot out the front of the hangar at flight speed and take-off immediately, thus alleviating the problem of take-off vulnerability. Helical rail guns are particularly well suited for this job, since they operate from electric power which is almost universally available (although specialized

power supplies or energy storage may have to be provided), and since they could be retrofitted to existing hangars if that proves feasible. The parameters for a point design for an F-15 fighter launcher are given in Table IV.2.3.1.

Table IV.2.3.1

Air Force Fighter Launcher Parameters

Acceleration Parameters:

Force = 347,186 Newtons

Length = 100 meters

Velocity = 75 meters per second

Catapult Parameters:

Single Boomed

Helix Width (W) = 1.00 meters

Helix Height (H) = 1.50 meters

Number of Buckets = 4

Drive Coil Length (L_d) = 0.409 meters

Helix Winding Thickness (S_d) = 0.0818 meters

Bucket Cross-section Axial Dimension (L_b) = 0.20 meters

Bucket Cross-section Thickness (S_b) = 0.16 meters

Magnetic Coupling (dM/dz) = 3.60 microhenries per meter

Number of Saddle Turns = 8

Number of Drive Coil Turns = 10

Bucket Conductor Mass = 10,045 kilograms

Conductor Material: Copper

Electrical Parameters:

Power Supply Voltage = 1,535 volts

Power Supply Current = 17,360 amps

Maximum Delivered Power = 26.65 megawatts

Brush Current Density = 15 amps/cm²

IV.2.4. Point Design: Launching Harriers From Destroyers

Presently the United States Navy maintains twelve operational large deck aircraft carriers, which carry over 80 aircraft apiece. These ships comprise by far the bulk of the Navy's offensive striking power, and a great deal of its defensive capability as well, which has the effect of making these ships not only highly capable, but also highly visible targets of great value. Thus, since it is impossible to build a ship that is completely invulnerable to any threat, it is currently being debated within the Navy and in the Congress just how vulnerable they really are.

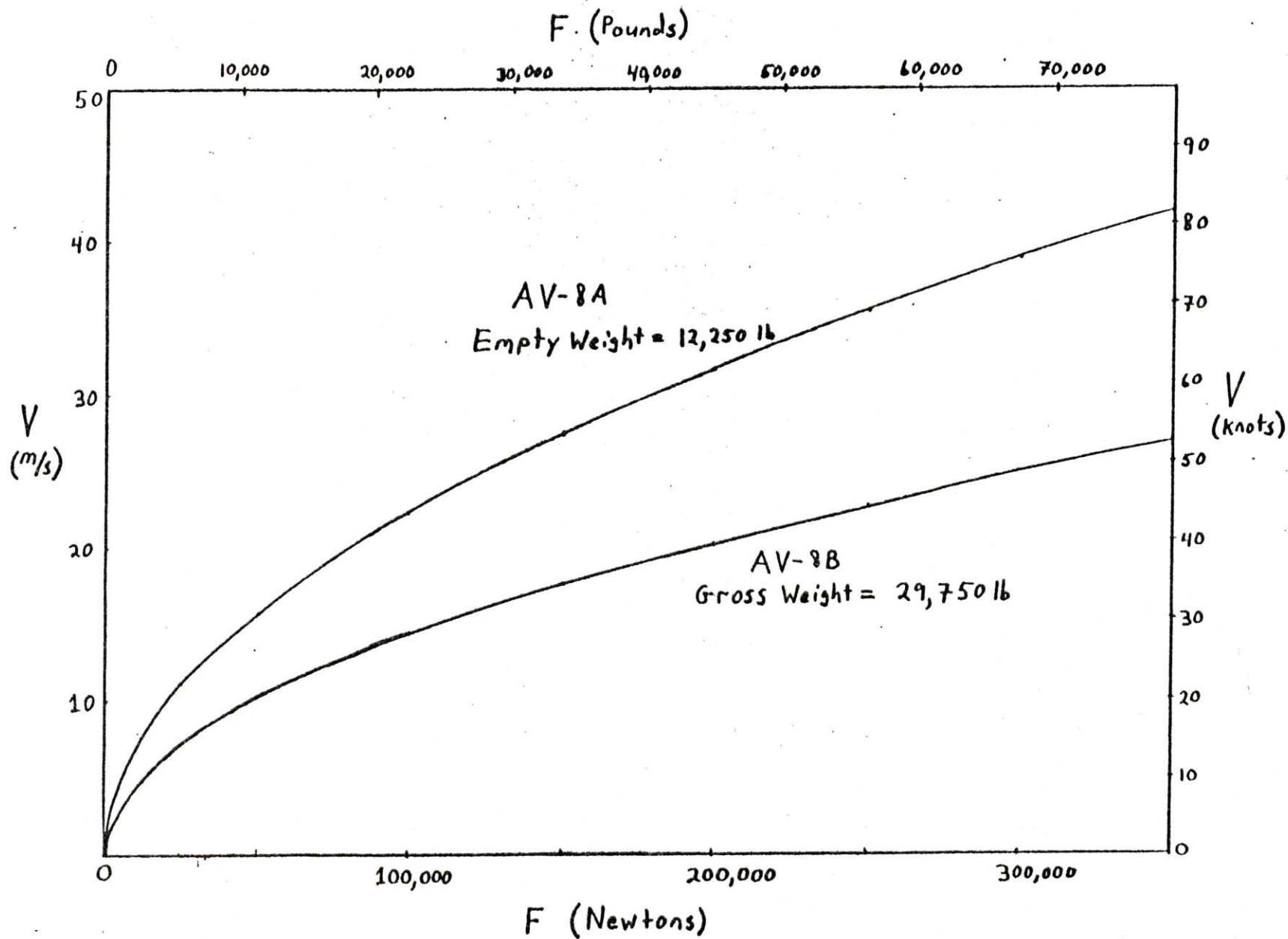
One solution to this potential problem which has been suggested is to base Vertical Take-Off and Landing (VTOL) fighters, such as the AV-8B Harrier II, on the helicopter pads of the destroyers, cruisers and helicopter carriers which are now operational in the fleet. The problem with this approach is that vertical take-off uses enormous quantities of fuel, which limits the combat radius of a fully loaded aircraft, or which requires that the aircraft carry only a light load of weapons. (A vertical landing, on the other hand, does not use nearly as much fuel as a vertical take-off, since the aircraft is much lighter, having burned almost all of its fuel, and dropped all of its ordnance.) Thus, if a way could be found to allow the aircraft to gain forward airspeed so that the wings

supported a significant fraction of the weight, the overall performance would be greatly increased. One way which has been proposed to do this is to build new ships with a short runway and ski-jump ramp on their bow. However, this requires the design and building of a whole new class of ships, which would take a long time to complete. Also, the Harriers could then be based effectively only on these few ships.

Intelligent application of helical rail guns would eliminate this objection. Helical rail gun catapults could be installed in the helicopter decks of destroyers, cruisers, and helicopter carriers where they would accelerate the Harriers or other VTOL aircraft based on these ships to flight speed. Figure IV.2.4.1 shows a family of curves for the launch speed of the aircraft for different take-off weights and applied catapult forces. The curves are plots of the energy equation.

$$V_f = \sqrt{\frac{2 F d}{M}} \quad \text{IV.2.4.1}$$

for both versions of the Harrier, the AV-8A (which is operational now) and the AV-8B (which is not yet operational, but which is a higher performance aircraft), where d , the launcher length, has been taken to be a constant equal to the length of the aircraft (approximately 14 meters in both cases). The points of interest include all combinations of the following: maximum nose gear tow load = 9,000 lb; maximum main gear tow load = 16,000 lb; and



Launch Velocity Versus Applied Force for Harriers

Figure IV.2.4.1

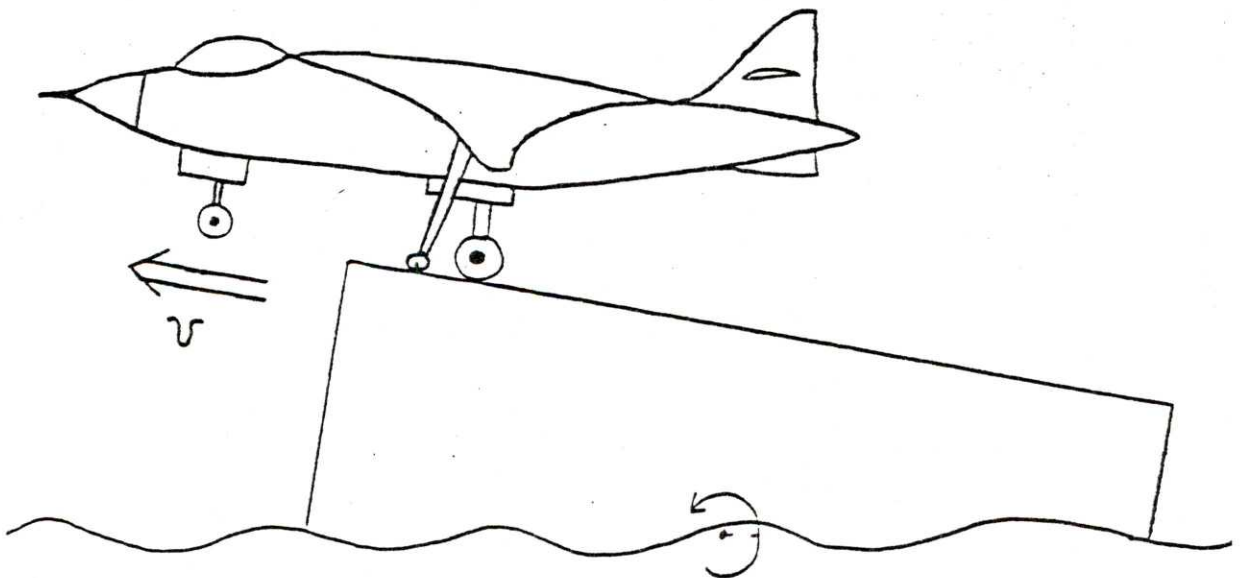
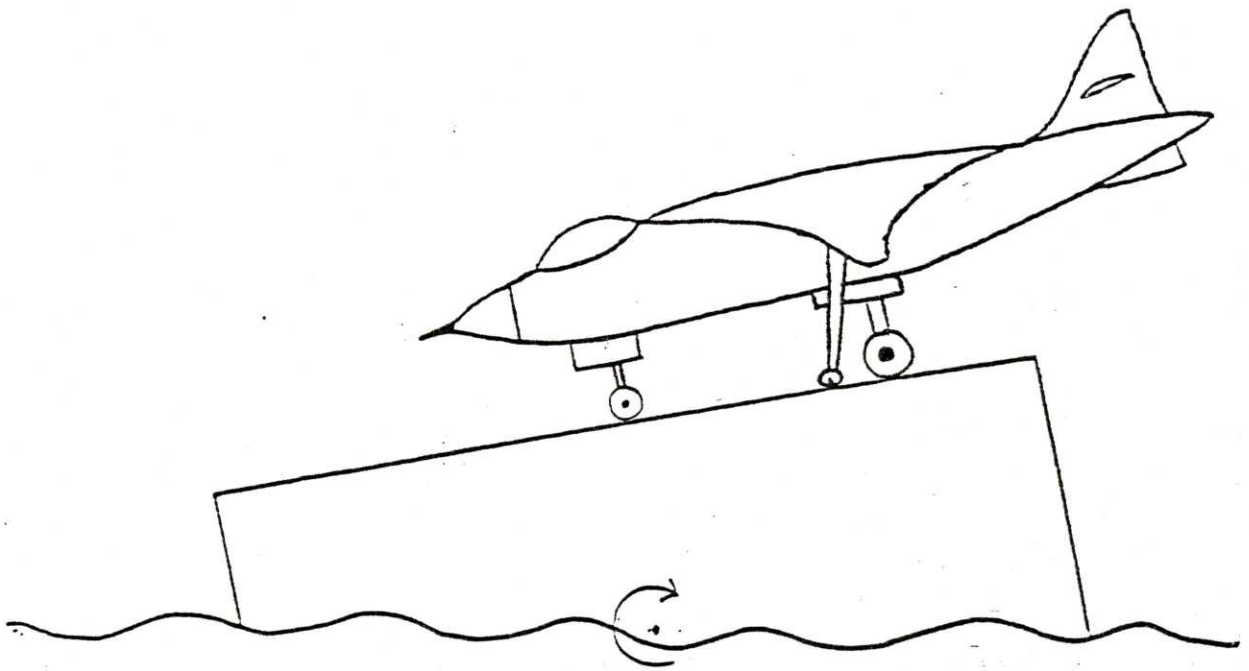
maximum engine thrust at sea level = 21,500 lb. Both of the towing load limits are for attachments low on the landing gear, and it may be possible to apply more force if the attachment can be made higher on the gear. Still, even at these limits a fully loaded aircraft (29,750 lb for the AV-8B) can be accelerated to 40 knots in its own length, which is an appreciable forward velocity for these aircraft, given their ability to vector their thrust. Thus the addition of helical rail gun catapults to the decks of these ships (73 ships capable of accomodating approximately 500 Harriers; **Aviation Week and Space Technology**, 9/21/81, pg. 63) would be a valuable addition to their effectiveness.

A helical rail gun equipped ship of this type would also be able to launch its aircraft at a positive angle from the horizontal, much as a ski-jump ramp equipped ship can. Since the aircraft would be launched off the beam of the ship, due to the position of the helicopter pad at the stern, the normal roll of the ship will alternately point the nose of the aircraft at the sky and at the surface of the water. By waiting to launch until the aircraft is pointed at the sky, a positive angle is achieved. This arrangement is shown in Figure IV.2.4.2.

Finally, many of the ships which can accept helicopters or Harriers do not have a steam based propulsion plant, and therefore could not accept the installation of a steam catapult. All ships do have onboard electrical power, however, and therefore could accept a helical rail gun catapult. The parameters for a point design for a VTOL

Figure IV.2.4.2

Launching at a Positive Angle to the Horizontal



catapult with the capabilities cited above are given in
Table IV.2.4.1

Table IV.2.4.1

Harrier Launcher Parameters

Acceleration Parameters:

Force = 111,206 Newtons

Length = 14 meters

Velocity = 20.7 meters per second

Catapult Parameters:

Single Boomed

Helix Width (W) = 0.67 meters

Helix Height (H) = 1.00 meters

Number of Buckets = 4

Drive Coil Length (L_d) = 0.19 meters

Helix Winding Thickness (S_d) = 0.038 meters

Bucket Cross-section Axial Dimension (L_b) = 0.10 meters

Bucket Cross-section Thickness (S_b) = 0.07 meters

Magnetic Coupling (dM/dz) = 5.68 microhenries per meter

Number of Saddle Turns = 8

Number of Drive Coil Turns = 10

Bucket Conductor Mass = 1425 kilograms

Conductor Material: Copper

Electrical Parameters:

Power Supply Voltage = 336 volts

Power Supply Current = 8082 amps

Maximum Delivered Power = 2.72 megawatts

Brush Current Density = 19.4 amps/cm²

IV.2.5 Point Design: Commercial Airliner Launcher

Helical rail gun catapults could also be used as an aid to airliners taking off from commercial airports. Using this extra assist, jetliners could take-off in a much shorter length of runway than normal; then, if take-off speed had not been achieved, due to icing or the aircraft being overgrossed, the pilot would have extra runway which would normally be unavailable to decide to continue the take-off or to abort. This would be particularly useful for runways such as Washington National Airport which are not really long enough for the traffic they must handle.

Use of electromagnetic assistance on take-off would also decrease the noise and pollution in the vicinity of the airport. This is of value for urban airports and other highly congested areas.

The parameters for a point design of such a launcher are given in Table IV.2.5.1.

Table IV.2.5.1

Commercial Aircraft Catapult

Acceleration Parameters:

Force = 1.02×10^6 Newtons
Length = 1,000 meters
Velocity = 75 meters per second

Catapult Parameters:

Double Boomed
Helix Width (W) = 1.00 meters
Helix Height (H) = 1.50 meters
Number of Buckets = 10
Drive Coil Length (L_d) = 0.409 meters
Helix Winding Thickness (S_d) = 0.0818 meters
Bucket Cross-section Axial Dimension (L_b) = 0.20 meters
Bucket Cross-section Thickness (S_b) = 0.16 meters
Magnetic Coupling (dM/dz) = 3.60 microhenries per meter
Number of Saddle Turns = 8
Number of Drive Coil Turns = 10
Bucket Conductor Mass = 25,114 kilograms
Conductor Material: Copper

Electrical Parameters:

Power Supply Voltage = 4,126 volts
Power Supply Current = 18,819 amps
Maximum Delivered Power = 77.64 megawatts
Brush Current Density = 15 amps/cm²

IV.3. Power Supplies

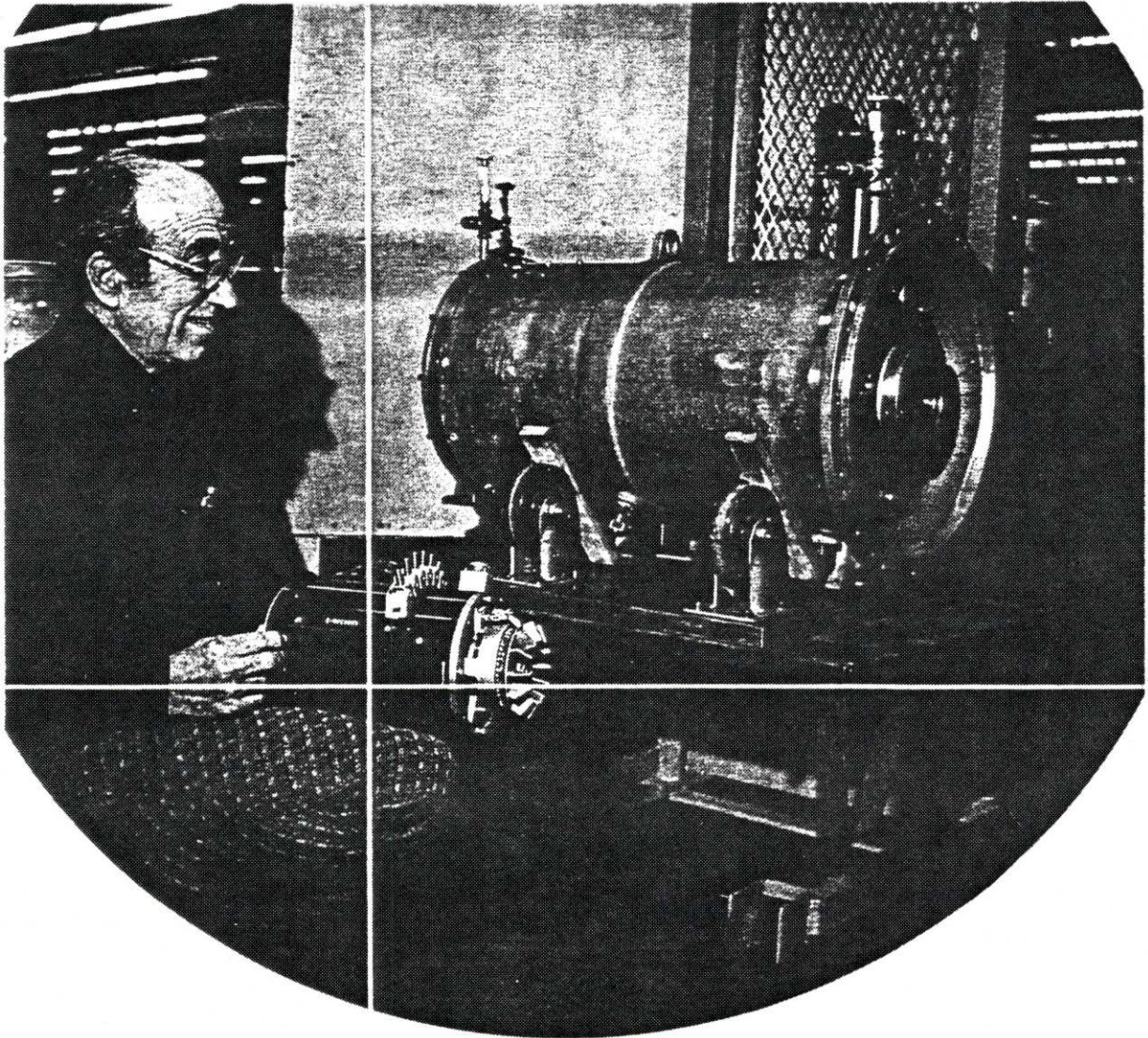
In all of the point designs thus far considered, it has been assumed that a power supply was available which would provide a constant current of the requisite magnitude at an arbitrary voltage. Most of the power levels required have been in the megawatt range, with some as high as 100 megawatts. For normal land based operations, such as the commercial aircraft launcher, these kinds of power levels should not be prohibitive, as they can be obtained from the existing power grid, or from a dedicated power plant built on site. For the military missions, however, and especially for those shipboard applications, a premium is placed on lightness and compactness, since these power supplies must be carried around or protected from attack.

The military applications are therefore on the borderline between being able to justify using electric power directly from a large generator or needing some form of intermediate energy storage. One form of direct electrical generation which shows promise for those applications requiring lower peak levels of power, such as the Harrier launcher, is the class of high power generators being developed as an outgrowth of the aerospace industry. For example, Bendix has developed a generator capable of an output of 3.2 megawatts which weighs only 850 pounds, and is smaller in size than a fifty gallon drum. (See Figure IV.3.1.) Putting three or

Figure IV.3.1

Bendix Megawatt Generator

28B371-1 Brushless AC Generator 3150 KW



**Electric &
Fluid Power
Division**

four of these onboard a destroyer or cruiser to power a catapult certainly does not seem unreasonable. For the higher power applications, however, such as the replacement catapult for aircraft carriers, or the Air Force fighter launcher, the problem is more difficult. There, some form of energy storage may have to be used to achieve the high power levels required, either as a supplement to direct generation or as a total replacement for it. This energy storage could take the form of a large inductor, some form of rotating pulse-rated generator, or other storage schemes, such as compressed air. Since this is currently an area of intense research, it would be premature to tie the design of these accelerators to any one scheme.

V. Conclusions

Helical rail guns are an exciting new class of electromagnetic accelerators which are technically advanced enough to be applied to real world problems, such as aircraft launching, but which still have many areas that are sufficiently poorly understood, such as the problem of commutating brush arcing, to yield fruitful research topics. At present the application which appears most useful and beneficial is the ship based VTOL aircraft launcher, and this should be explored in more depth and detail. Questions which need to be answered in that regard are the maximum accelerating force which can be applied to the aircraft, and the effect on the ships engines of suddenly diverting more than ten megawatts of power from the propulsion of the ship to the propulsion of an aircraft. Also, the power supply for such a device needs to be looked at in much greater detail, to determine what generator configuration is best suited to such application, or even if energy storage should be used.

With regard to the basic physics involved in helical rail guns, the phenomenon least understood remains helix commutation, and commutating brush arcing. None of the theories developed as of this writing satisfactorily explain why the leading brush arcing is so much worse than the trailing brush arcing, although inclusion of the magnetic fields generated by the bucket coils may change this.

Experimental tests should be performed using the two piece capacitative brush described in the section on theory to see if it actually suppresses helix brush arcing. Tests should also be performed with complete rings of helix brushes, to test the theory that this configuration acts like an ordinary sliding brush which merely spirals around the track of the helix and thus never really commutates.

In conclusion, helical rail guns show great promise for future applications. They can perform important tasks which would be difficult or impractical to perform using other methods, and they can be custom designed to fit the task at hand.

A. Appendix A: Helical Rail Glider Launcher

HELICAL RAIL GLIDER LAUNCHER

By
Peter Mongeau and Fred Williams

Abstract: The electromagnetic acceleration group at MIT has undertaken to build an electric glider launcher. The launcher features a mobile helical rail accelerator and power supply. It will launch a 6 foot radio-controlled glider for an overall range of several miles. This device is a prototype for a larger system that will provide a launch platform for munition and supply loaded gliders and a wide variety of RPV's. A 6 meter helical rail launcher has been constructed and is being tested. It is a twin boom device designed to accelerate a 5 kg glider to 100 m/s at 100 g's acceleration.

INTRODUCTION

Helical rail accelerators are a class of high performance linear accelerators. They are synonymous with Thom and Norwood's "sliding coil accelerator" as well as Marshall and Weldon's "repulsion coil projector". At the risk of confusing the issue further, we prefer the more descriptive name "helical rail accelerator". This stems from the fact that these accelerators are topologically equivalent to taking the rails and armature of a rail gun and twisting them into coaxial helices.

Essentially, they are an air-core linear DC electric motor commutated by conventional sliding brushes attached to a moving bucket or slidor (analogous to the rotor). The slidor is constructed to run coaxially on the inside or outside of a helical conductor which serves as the stator. A limited section of the helix is energized by the slidor brushes. These brushes are situated to provide a maximum and continuous thrust as the slidor moves down the helix. Helical rail accelerators offer high performance and integral force containment in conjunction with high efficiency (greater than 50%).

MECHANICAL DESIGN

The launcher's mechanical design revolves around keeping the two booms rigid during the anticipated 2000 pound launch forces. The booms themselves are stainless steel tubes supported at each end by braced aluminum "V's". These two V's are in turn mounted to one aluminum I beam extending the length of the launcher which ties the whole assembly together. Several sturdy mounting fixtures are provided to permit tensioning of the booms and the I beam thus guaranteeing a stiff structure.

Manuscript received January 23, 1981.

The authors are with the Francis Bitter National Magnet Laboratory, Massachusetts Institute of Technology, Cambridge, MA 02139, respectively.

The stator helix is rectangular wire edge-wound on fiberglass-transite composite tubes. These tubes have mating ends of brass that serve as electrical as well as mechanical connectors. Several tubes can be slid over the steel boom and are clamped to form a continuous helix of high rigidity and good alignment. On each boom there are four 5 foot long tubes. The first three are the accelerator, while the fourth has an opposite pitch helix and will be used to decelerate the buckets once the glider has been released.

The buckets house the slidor windings and the brush assembly. For our initial design each boom has one bucket, although more buckets could be added to increase the total force per boom. The buckets are stationed together by a yoke structure which accelerates the glider while assuring the tandem bucket alignment. For the initial testing a single boom was mounted with 3 helix wound tubes (2 acceleration - 1 deceleration).

It should be pointed out that the entire launcher is extremely overdesigned and should be able to withstand the ultimate performance limit of the electrical accelerator itself. Figure 1 shows what the entire system might look like in the field.

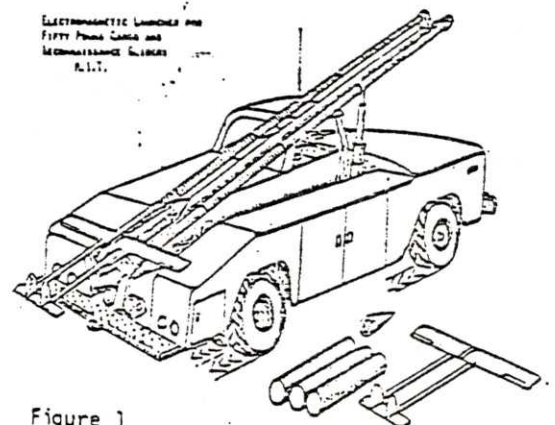


Figure 1

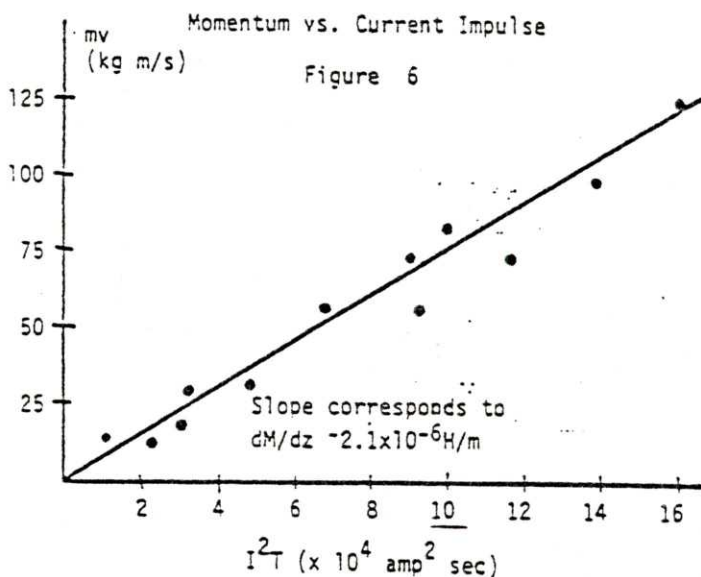
ELECTRICAL DESIGN

The energy source for the launcher is a large array of electrolytic filter capacitors. Each one is roughly the size of a beer can and is rated at 2500µF, 350 volts and will store 150 joules. We have 1600 of them for a total of 240 kJ. They are arranged electrically in 20 cells, each cell featuring separate SCR switching and control. This allows a staggered discharge into a common load permitting any desired output pulse form. The entire bank is housed in 4 steel cabinets mounted on casters; each cabinet can be easily handled by one person. Figure 2 shows the simplified capacitor bank schematic.

Where N_b and N_d are the bucket and drive coil turns respectively, and dM/dz is the mutual inductance gradient between the two coils. This relationship can be verified in several ways. The most direct is to simultaneously measure the current and the time rate of change of velocity. This involves finding small differences in velocity over short distances. Alternatively, one can determine the terminal velocity as a function of the current history. The momentum can be found from (1) to be

$$mv = \int F dt = b \int I^2 dt \quad (2)$$

A linear relationship between momentum and " $I^2 t$ " would then substantiate the motor force of (1). Figure 6 plots several shots over a wide range of momentum. The linear dependence supports the above argument.



Most rotary motor engineers think of motor operation in terms of the "back emf" which is the dynamic voltage one must push against in doing electro-mechanical work. For the linear motor the electrical power converted to mechanical work is

$$P = V_{\text{bemf}} I = Fv = BI^2 v \quad (3)$$

The back voltage if then

$$V_{\text{bemf}} = bIv \quad (4)$$

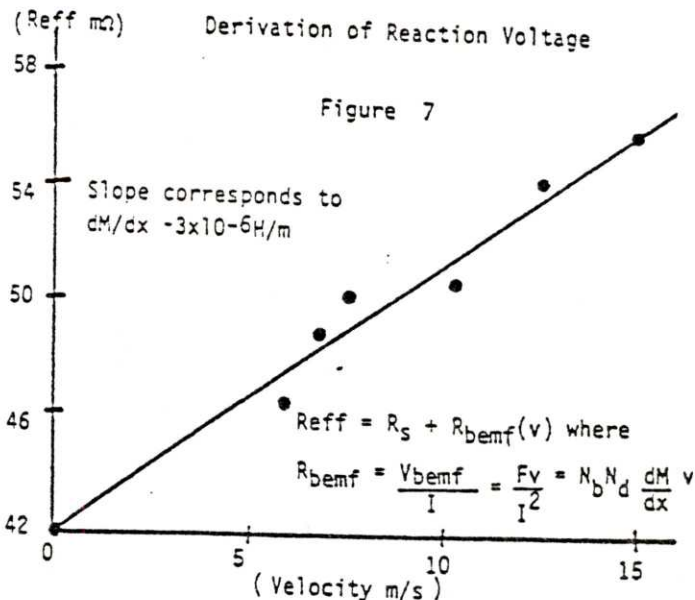
Which can be thought of as due to a dynamic resistance

$$R_{\text{bemf}} = bv \quad (5)$$

The effective resistance is then

$$R_{\text{eff}} = R_s + R_{\text{bemf}}(v) \quad (6)$$

Where R_s is the stationary DC resistance. Figure 7 plots this resistance versus velocity. The linear proportionality agrees well with the design parameters of $dM/dz = 2.3 \times 10^{-6} \text{ H/m}$.



Finally the theory of operation can again be checked by comparing the observed electro-mechanical efficiency to the theoretical one. The instantaneous efficiency is

$$n(v) = \frac{bv}{bv + R_s} \quad (7)$$

And the average efficiency is

$$n_{\text{ave}} = \frac{1}{v_f} \int_0^{v_f} n(v) dv \quad (8)$$

Where v_f is the final velocity. Table 1 tabulates the performance of a typical shot, and again the agreement with experiment is good. If we extrapolate the performance to higher velocities, we find that at $v_f = 75 \text{ m/s}$ we would be achieving 50% efficiency. This observation demonstrates one of the helical rail gun's chief advantages: very high efficiency can be achieved even at very modest velocities. Direct consequence of the good coupling of multi-turn coaxial geometry

Table I.

Typical Shot Performance

v_{max}	= 30.5 m/s
acc_{max}	= $710 \text{ m/s}^2 = 73 \text{ g's}$ ($I_{\text{peak}} = 2 \text{ KA}$)
F_{max}	= 2.9 KN = 650 lbs
Bank Energy	= 24.3 KJ (3 farad bank at 125 V)
N_{exp}	= 16% (including 18mΩ tether resistance as versus 24 mΩ motor resistance)
for n_{ave}	= 16% would require
$a = \frac{bv_f}{R}$	= .4 or $b = N_b N_d \frac{dM}{dz}$
$\frac{dM}{dz}$	= $1.5 \times 10^{-6} \text{ H/m}$ (or $dM/dz = 2 \times 10^{-6} \text{ H/m}$ including drag)

LIMITS

Only a limited range of velocities have been thoroughly tested. Thus far, there is no evidence of reaching any intrinsic limits. For simplicity we have extrapolated this reference accelerator design to give an idea of the limits of helical accelerators in general.

Using a tensile strength of 20,000 psi in the copper windings and a solenoidal field approximation, we derive a net drive force of 16,800 lbs per bucket coil and an acceleration of 7,300 g's. The bucket can thermally sustain this acceleration for a period of 2 seconds at which time it would be traveling 15 km/s. These results can be significantly improved by reinforcing the copper windings or by "field shading", a technique by which the drive coil and bucket coil cancel each others longitudinal fields.

The most serious uncertainty about high speed operation (greater than 1 km/s) is the sliding electrical contacts of the brushes. Marshall has determined that high current density brushes fail at speeds above approx. 1 km/s. However, the helical geometry permits multiturn windings and a full circumferential set of brushes, both features which decrease brush current substantially. Further experiments will have to be made to see if the 1 km/s limit can be successfully exceeded in the lower current density regime.

CONCLUSIONS

Based on our preliminary experiments there seems to be little doubt that the completed launcher will satisfy the design goals of $v_f = 100\text{m/s}$ and a payload mass of 5 kg. Beyond our initial objectives we are led to wonder just how broad the useful area of operation of helical rail guns is. Several kilometer per second launchers may seem optimistic at first, but the present brush limitations are amenable to research and development and the rewards of greater than 90% efficiency (at these velocities) makes the effort very attractive. At the other extreme accelerating several ton's at the 100m/s regime is a trivial matter of connecting a sufficient number of launchers together or simply scaling the size of the launcher appropriately.

ACKNOWLEDGEMENTS

The research reported in this paper was performed at the Francis Bitter National Magnet Laboratory at the Massachusetts Institute of Technology supported by the National Science Foundation. The research was supported by the U.S. Army Armament Research and Development Command and the Defense Advanced Research Projects Agency, D.O.D., under contract No. DAAK10-79-C-0/84. The software used here for field analysis, particularly that of figure 3, was developed by Ken McKinney, a member of our group, as part of his undergraduate thesis. It revolves around a current filament approach using an approximation of the exact analytical solutions rather than a finite difference method. We would also like to acknowledge Henry Kolm for his guidance throughout this investigation.

REFERENCES

- [1] K. Thom and J. Norwood, "Theory of an Electromagnetic Mass Accelerator for Achieving Hypervelocities", Langley Research Center, June 1961.
- [2] R. Marshall and W. Weldon, "Comparison of Linear Induction, Synchronous and Homopolar Accelerators...", Center for Electromechanics University of Texas, Austin, December 1979.
- [3] R. Marshall, "Moving Contacts in Macro-Particle Accelerators", Seminar on Energy Storage Compression and Switching, Canberra, Australia, November 1977.

B. Appendix B: BMAP Program and Explanation

B.1. Theory Behind The Program BMAP

The finite length current filament shown in Figure B.1.1 produces a magnetic field at all points in space

$$\vec{B}(r, \phi, y) = \left(\frac{\mu_0 I_1}{4\pi r} \right) \left[\frac{(y + \frac{L}{2})}{\{(y + \frac{L}{2})^2 + r^2\}^{3/2}} - \frac{(y - \frac{L}{2})}{\{(y - \frac{L}{2})^2 + r^2\}^{3/2}} \right] \vec{i}_\phi \quad \text{B.1.1}$$

and if a differential length current filament is now placed somewhere in space it will feel a force

$$d\vec{F} = \vec{I}_2 \times \vec{B} \, ds \quad \text{B.1.2}$$

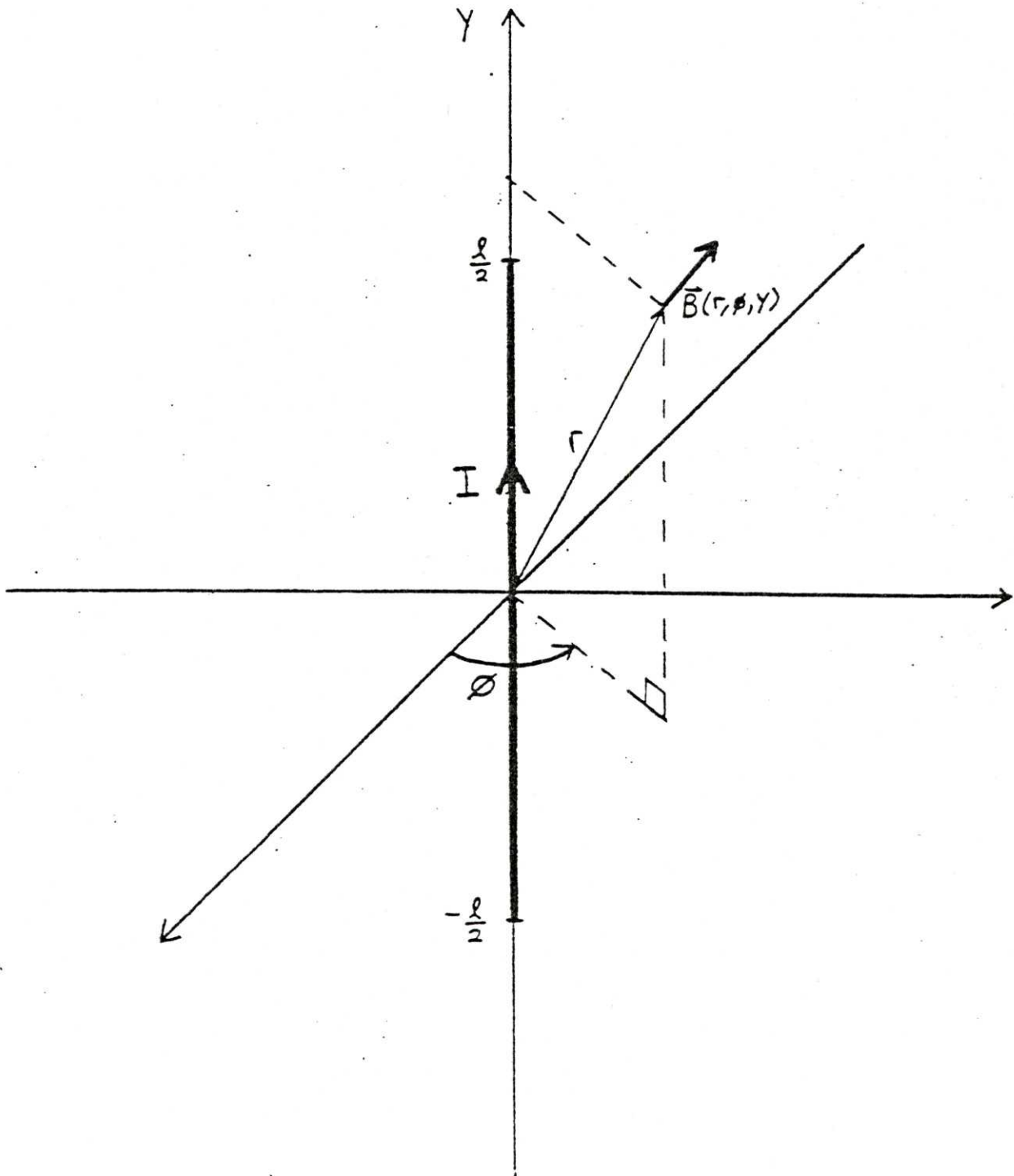
The force felt by a second finite length current filament placed arbitrarily in space parallel to the y-axis is found by integrating these differential forces and is

$$F = \left(\frac{\vec{i}_r}{r} \right) \int_{y=a}^{y=b} \left(\frac{\mu_0 I_1 I_2}{4\pi r} \right) \left[\frac{(y + \frac{L}{2})}{\{(y + \frac{L}{2})^2 + r^2\}^{3/2}} - \frac{(y - \frac{L}{2})}{\{(y - \frac{L}{2})^2 + r^2\}^{3/2}} \right] dy \quad \text{B.1.3}$$

Now this force is directed in the radial direction and therefore is composed of both propulsive forces directed along the z-axis, and explosive forces directed along the x-axis. Also, since we are interested in dM/dz rather than forces, this must be divided by the two currents flowing. When this is done we get

Figure B.1.1

Magnetic Field From a Finite Current Segment



$$dM/dz = \left(\frac{\mu_0}{4\pi}\right)\left(\frac{z}{r^2}\right) \int_{y=a}^{y=b} \left[\frac{(y+\frac{\ell}{2})}{\{(y+\frac{\ell}{2})^2+r^2\}^{1/2}} - \frac{(y-\frac{\ell}{2})}{\{(y-\frac{\ell}{2})^2+r^2\}^{1/2}} \right] dy \quad \text{B.1.4}$$

which becomes upon evaluating the integral

$$dM/dz = \left(\frac{\mu_0}{4\pi}\right)\left(\frac{z}{r^2}\right) \left\{ \left[\left((b+\frac{\ell}{2})^2+r^2 \right)^{1/2} - \left((a+\frac{\ell}{2})^2+r^2 \right)^{1/2} \right] \right. \\ \left. - \left[\left((b-\frac{\ell}{2})^2+r^2 \right)^{1/2} + \left((a-\frac{\ell}{2})^2+r^2 \right)^{1/2} \right] \right\} \quad \text{B.1.5}$$

This is the magnetic coupling between two current filaments. To compute the magnetic coupling between a filamentary rectangular drive coil and a filamentary saddle bucket, all that must be done is to add up all the different contributions. Actually, since the real finite build coils will be centered relative to one another, it is only necessary to compute the magnetic coupling for the filamentary drive coil and filamentary bucket hairpin shown in Figure B.1.2 and multiply by two. When this is done, and the mathematics followed through, the result is Equations B.1.6.

$$dM/dz = 4 (u / 4) (z) \{Q_1 + Q_2 - Q_3 - Q_4\}$$

$$Q_i = \{(V_{1i})^{1/2} - (V_{2i})^{1/2} - (V_{3i})^{1/2} + (V_{4i})^{1/2}\} / r_i^2$$

(i = 1, 2, 3, 4)

$$r_1^2 = x^2 + z^2$$

$$r_2 = r_1$$

$$r_3^2 = (W + x)^2 + z^2$$

$$r_4^2 = (H + x)^2 + z^2$$

B.1.6

$$V_{11} = V_{13} = (H + x)^2 + r_{1,3}^2$$

$$V_{21} = V_{23} = r_{1,3}^2$$

$$V_{31} = V_{33} = x^2 + r_{1,3}^2$$

$$V_{41} = V_{43} = H^2 + r_{1,3}^2$$

$$V_{12} = V_{14} = (W + x)^2 + r_{2,4}^2$$

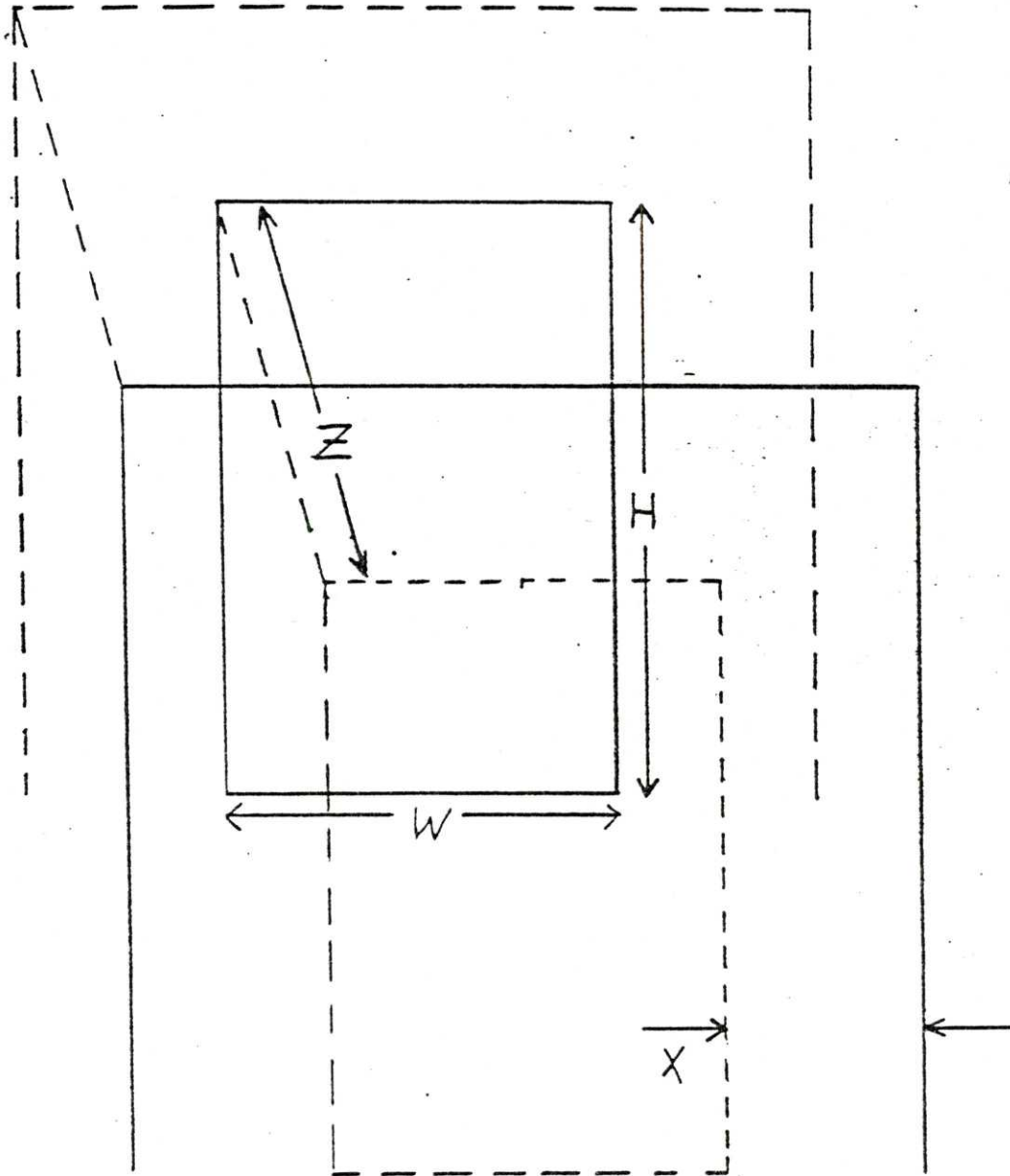
$$V_{22} = V_{24} = 0$$

$$V_{32} = V_{34} = x^2 + r_{2,4}^2$$

$$V_{42} = V_{44} = 0$$

Figure B.1.2

Filamentary Bucket Hairpin and Drive Coil Rectangle



E.2. BMAP: A Program To Calculate Rectangular Saddle Bucket
DM/DZ's

```

10 PRINT "THIS PROGRAM PRINTS A DM/DZ MAP FOR SADDLE WINDINGS AROUND A"
20 PRINT "RECTANGULAR DRIVE COIL OF SPECIFIED SIZE AND DIMENSIONS. "
30 PRINT "THE CONVENTIONS USED ARE AS FOLLOWS:"
40 PRINT
50 PRINT "W = THE WIDTH OF THE HELIX (OUTSIDE DIMENSION)"
60 PRINT
70 PRINT "H = THE HEIGHT OF THE HELIX (OUTSIDE DIMENSION)"
80 PRINT
90 PRINT "L = THE AXIAL LENGTH OF THE DRIVE COIL"
100 PRINT
110 PRINT "S = THE TRANSVERSE THICKNESS OF THE DRIVE COIL WINDINGS"
120 PRINT
130 PRINT "X = THE TRANSVERSE DISTANCE FROM THE SURFACE"
140 PRINT "    OF THE DRIVE COIL"
150 PRINT
160 PRINT "Z = THE AXIAL DISTANCE FROM THE MID-PLANE OF THE DRIVE COIL (L/2)"
170 PRINT
180 PRINT "THIS PROGRAM GIVES OUTPUT IN DIMENSIONAL FORM; THE UNITS"
190 PRINT "USED FOR DISTANCE ARE ASSUMED TO BE METERS. HOWEVER, SINCE"
200 PRINT "THE BASIC MUTUAL INDUCTANCE GRADIENT EQUATIONS ARE SCALE"
210 PRINT "SIZE INDEPENDENT, ANY OTHER CONSISTENT DISTANCE UNITS WILL"
220 PRINT "WORK JUST FINE (I.E. INCHES OR CENTIMETERS ARE OK). IN ALL"
230 PRINT "CASES THE UNITS OF THE TABLE BEING CALCULATED HERE WILL BE"
240 PRINT "MICRO-HENRIES PER METER."
250 PRINT
260 PRINT "INPUT THE DRIVE COIL PARAMETERS W,H,L,S"
270 INPUT W,H,L,S
280 PRINT "INPUT THE MATRIX SPACING (USUALLY LESS THAN S)"
290 INPUT G1
300 PRINT
310 LPRINT "THIS IS A DM/DZ MAP FOR SADDLE WINDINGS AROUND A RECTANGULAR"
320 LPRINT "DRIVE COIL. THE TOP ROW REPRESENTS THE FRONT EDGE (Z=L/2) OF THE"
330 LPRINT "COIL, AND THE LEFTMOST COLUMN REPRESENTS THE DM/DZ VALUES"
340 LPRINT "FOR SADDLE FILAMENTS TOUCHING THE SURFACE OF THE COIL (X=0)."

```

```

470 REM I IS THE AXIAL GRID SPACING; J IS THE TRANSVERSE GRID SPACING
480 FOR I=0 TO 25
490 FOR J=0 TO 15
500 Q9=0
510 REM K IS THE AXIAL GRID SPACING THROUGH THE DRIVE COIL BUILD
520 FOR K=0 TO 9
530 Z=I*G1+L*(9-2*K)/20+L/2
540 REM P IS THE TRANSVERSE GRID SPACING THROUGH THE DRIVE COIL BUILD
550 FOR P=0 TO 3
560 S1=S*(1+2*P)/8
570 X=J*G1+S1
580 H1=H-2*S1
590 W1=W-2*S1
600 X1=X
610 V=H1+X
620 B=1
630 GOSUB 920
640 Q1=Q
650 X1=W1+X
660 GOSUB 920
670 Q3=Q
680 V=X1
690 X1=X
700 B=0
710 GOSUB 920
720 Q2=Q
730 X1=H1+X
740 GOSUB 920
750 Q4=Q
760 Q9=Q9+Z*(Q1+Q2-Q3-Q4)
770 NEXT P
780 NEXT K
790 REM DIVIDING BY 40 BECAUSE 40 FILAMENTS WERE USED IN DRIVE COIL
800 Q9=Q9/40
810 M1=(4E-7)*Q9
820 M=M1*1E6
830 PRINT M;
840 LPRINT USING "###.## "; M;
850 NEXT J
860 PRINT
870 LPRINT
880 PRINT
890 LPRINT
900 NEXT I
910 PRINT
920 R2=X1*X1+Z*Z
930 V1=V*V+R2
940 V2=R2*B
950 V3=X*X+R2
960 V4=(H1*H1+R2)*B
970 Q=(SQR(V1)-SQR(V2)-SQR(V3)+SQR(V4))/R2
980 RETURN
990 END

```

Appendix C: Optimization Based on Efficiency

The instantaneous efficiency of any electromagnetic accelerator is

$$\eta_{\text{inst}} = 1 / (1 + u/v) \quad \text{C.1}$$

where u is the break point velocity defined as the power loss divided by the generated force. For purely resistive losses this can be given in terms of current densities and conductor cross-sectional areas, and is

$$u = \frac{R_b^o}{\langle \frac{dM}{dz} \rangle} \left[\left(\frac{J_d}{J_b} \right) \left(\frac{A_d}{A_b} \right) \left(\frac{R_d^o}{R_b^o} \right) + \left(\frac{J_b}{J_d} \right) \left(\frac{A_b}{A_d} \right) \right] \quad \text{C.2}$$

where the subscripts b and d refer to the bucket and drive coil respectively, and the superscript o means single turn. It has already been shown that for optimum efficiency the power dissipation in the bucket must equal the power dissipation in the drive coil; thus

$$J_d^2 A_d^2 R_d^o = J_b^2 A_b^2 R_b^o \quad \text{C.3}$$

which leads to

$$u_1 = \frac{2 \sqrt{R_b^o R_d^o}}{\langle \frac{dM}{dz} \rangle} \quad \text{C.4}$$

where the subscript 1 on the u signifies that one optimization has been performed. The single turn resistances can now be rewritten in terms of cross-sectional areas, current path lengths, and resistivities as

$$R = \rho \ell / A \quad \text{C.5}$$

which, when plugged in yields

$$u_1 = \frac{2 \sqrt{\rho_b \rho_d \ell_b \ell_d}}{\langle \frac{dM}{dz} \rangle (A_b + A_d) \sqrt{\left(\frac{A_b}{A_b + A_d}\right) \left(\frac{A_d}{A_b + A_d}\right)}} \quad \text{C.6}$$

The relative balance between the two coil cross-sectional areas can now be adjusted independently of the other parameters if the areas are normalized to the scale factor $A_b + A_d$. When this is done, it is found that the break point velocity is minimized with $A_b = A_d$. This assumes that the two current path lengths, ℓ_d and ℓ_b , are independent of the cross sectional areas. For the thin build coil resistance approximations we have used, this is strictly true for all drive coils and all non-saddle bucket coils. For saddle bucket coils, the path length is influenced by the axial length of the drive coil, but I am going to assume that this is negligible.

The minimum break point velocity is thus

$$u_{\min} = \frac{2 \sqrt{\rho_b \rho_d \ell_b \ell_d}}{\langle \frac{dM}{dz} \rangle A_b} \quad \text{C.7}$$

This is more conveniently written as

$$\langle dM/dz \rangle A_b = \frac{2r \sqrt{\rho_b \rho_d l_b l_d'}}{V_f} \quad C.8$$

where r has been used for the ratio V_f/u , and is directly related to the efficiency by Equation C.1.

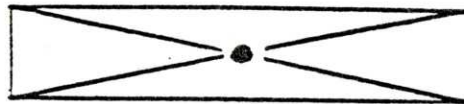
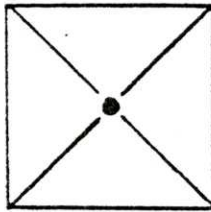
From experience with dM/dz maps, the average magnetic coupling felt by an arbitrary rectangular bucket coil cross-section wrapped around an arbitrary rectangular drive coil cross-section is equal to the magnetic coupling felt by the current filament at the geometric center of that bucket coil cross-section, at least to within 5% or so. (This is almost certainly due to the fact that we are seeing a dominant first order effect, but I have not attempted to prove this.) By symmetry, the drive coil can be replaced by the current filament at its geometric center. This situation is shown in Figure C.1.

The magnetic coupling between the two current filaments must still be solved for. For rectangular geometries, Appendix B gives analytic expressions for the magnetic coupling; for circular geometries, the expressions involve elliptic integrals, and therefore cannot be solved analytically. However, even the analytic expressions for rectangular geometries are too hard to deal with effectively, and simplifications are in order.

Figure C.2 shows how the rectangular geometry saddle bucket problem can be simplified. The single complicated

Figure C.1

Replacement of Finite Build Coils With Central Filaments



⊥

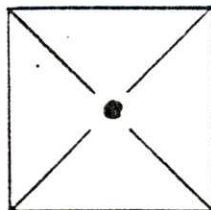
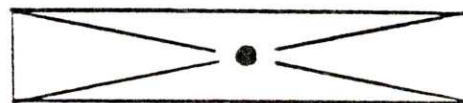
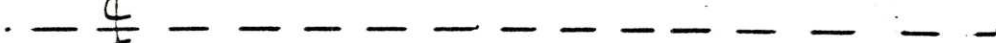
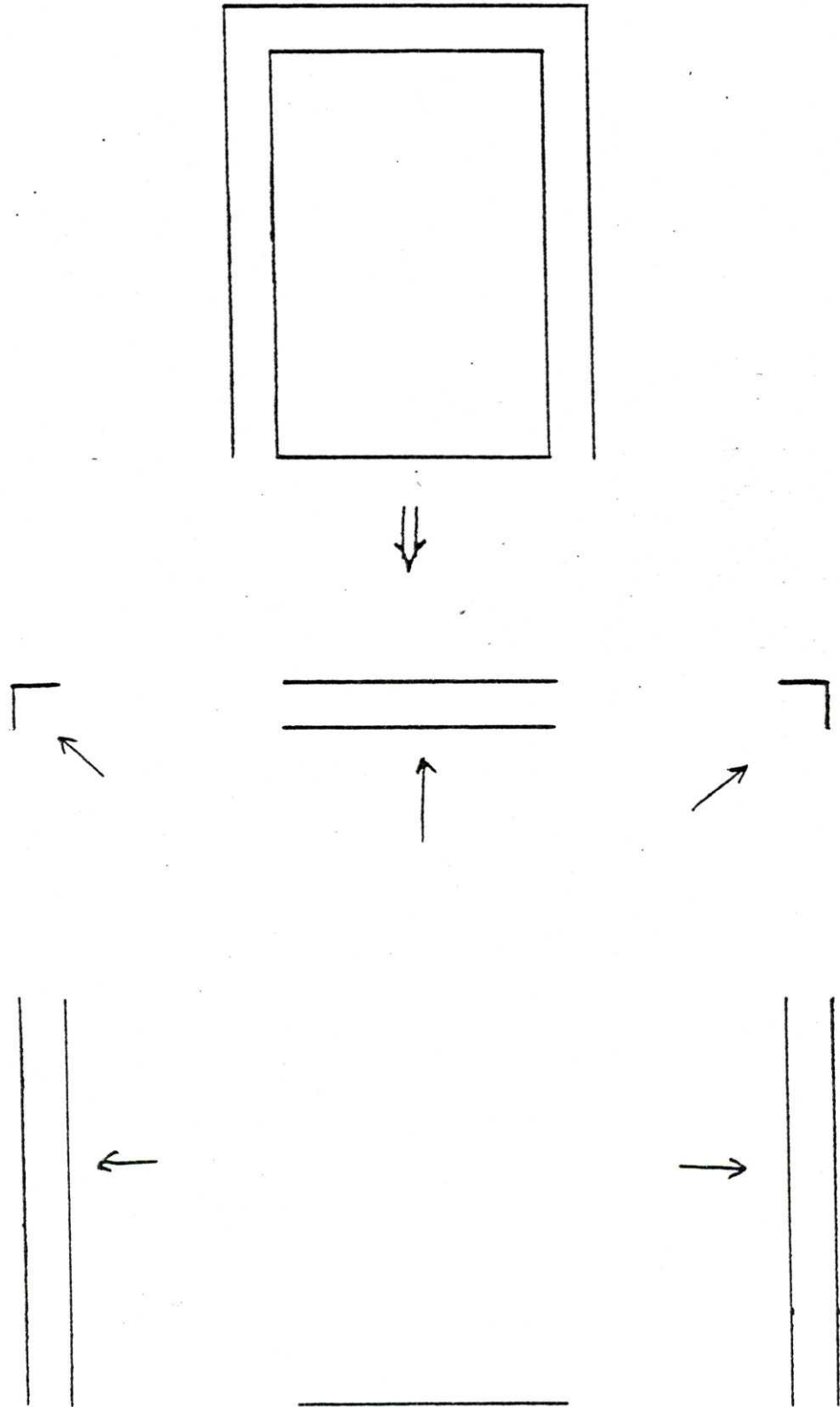


Figure C.2

Simplification of the dM/dz Calculation Problem



problem has been broken down into three simple problems by separating the sides and lopping off the corners. Although this introduces two major sources of error, they do tend to cancel one another out. Separating the sides tends to increase the calculated coupling, since the opposite sides which acted to decrease the coupling are no longer there. However, lopping off the corners tends to decrease the calculated coupling, since they added to it and are no longer there. I have not attempted to determine which effect dominates; it may be situation dependent.

If this simplification is made then, the coupling between a rectangular drive coil and a rectangular saddle bucket coil can be approximated as

$$\langle dM/dz \rangle = 4 \left(\frac{\mu_0}{4\pi} \right) \left(\frac{z}{x^2+z^2} \right) \left\{ 2 [H^2+x^2+z^2]^{1/2} + [W^2+x^2+z^2]^{1/2} - 3 [x^2+z^2]^{1/2} \right\} \quad \text{C.8}$$

where z is the axial distance between the filaments and x is the transverse distance between them. These distances can then be given in terms of the coil dimensions as

$$z = (L_b + L_d) / 2 \quad \text{C.9}$$

and

$$x = (S_b + S_d) / 2 \quad \text{C.10}$$

where the clearances have been assumed to be zero. The coil

dimensions can now be given in terms of the ratios L_b/S_b and L_d/S_d and the coil cross-sectional areas A_b and A_d . Since $A_b = A_d$,

$$L_d = \sqrt{A_b (L_d/S_d)} \quad \text{C.11}$$

$$S_d = \sqrt{A_b / (L_d/S_d)} \quad \text{C.12}$$

$$L_b = \sqrt{A_b (L_b/S_b)} \quad \text{C.13}$$

$$S_b = \sqrt{A_b / (L_b/S_b)} \quad \text{C.14}$$

Plugging these into Equation C.8 yields

$$A_b^* \frac{dM}{dz} = 4 \left(\frac{\mu_0}{4\pi} \right) Y \left\{ \frac{\sqrt{\frac{L_d}{S_d}} + \sqrt{\frac{L_b}{S_b}}}{q^{3/2}} \right\} \quad \text{C.15}$$

with

$$q^2 = \left(\sqrt{\frac{L_d}{S_d}} + \sqrt{\frac{L_b}{S_b}} \right)^2 + \left(\sqrt{\frac{S_d}{L_d}} + \sqrt{\frac{S_b}{L_b}} \right)^2 \quad \text{C.16}$$

$$\theta = A_b^* q^2 \quad \text{C.17}$$

and

$$Y = \theta \left\{ 2 \left[\frac{4H^{*2}}{\theta} + 1 \right]^{1/2} + \left[\frac{4}{\theta} + 1 \right]^{1/2} - 3 \right\} \quad \text{C.18}$$

The function Y has the asymptotic value as θ becomes large of $Y_{\max} = 2(2H^{*2} + 1)$. This allows us to define the maximum

value of A_b^* dM/dz purely in terms of the ratios L_d/S_d and L_b/S_b , and to define the convenient dimensionless function θ ,

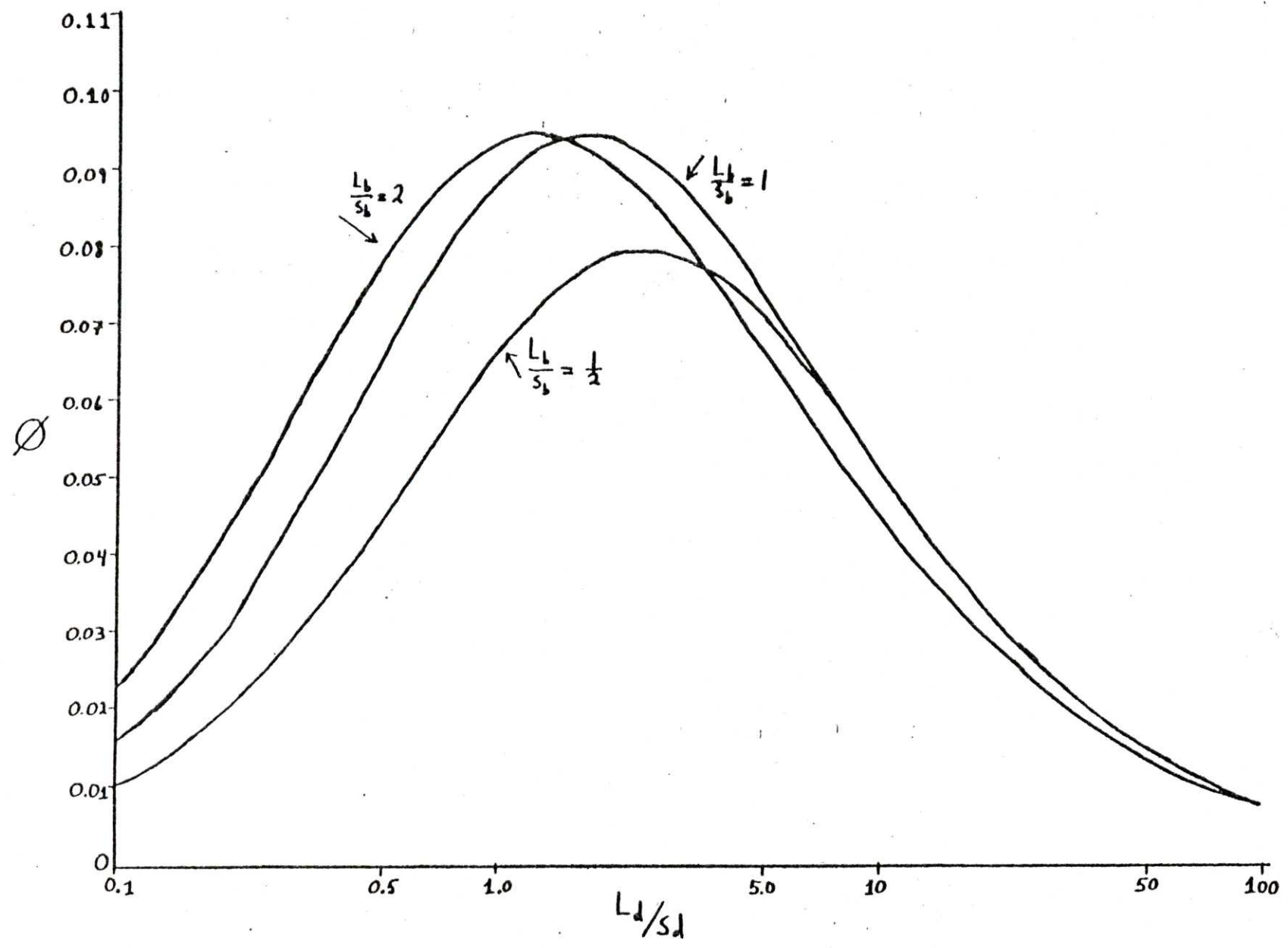
$$\theta = \frac{\left(\sqrt{\frac{L_d}{S_d}} + \sqrt{\frac{L_b}{S_b}}\right)}{\left\{\left(\sqrt{\frac{L_d}{S_d}} + \sqrt{\frac{L_b}{S_b}}\right)^2 + \left(\sqrt{\frac{S_d}{L_d}} + \sqrt{\frac{S_b}{L_b}}\right)^2\right\}^{3/2}} \quad \text{C.19}$$

which is plotted in Figure C.3 for $L_b/S_b = 1/2, 1, \text{ and } 2$. So the optimization algorithm is as follows: first pick the value of L_d/S_d which maximizes θ , subject to the constraints imposed by the problem, and assuming $L_b/S_b = 1$; next, pick the maximum value for θ based on the requirement that S_d^* be less than $1/2$, i.e.

$$\theta \leq (L_d/S_d) q^2 / 4 \quad \text{C.20}$$

Then, using the all of the above, calculate values for A_b^* , L_d^* , and S_d^* ; and finally, generate an actual dM/dz map based on L_d^* and S_d^* to give the final configuration.

Figure C.3
 ϕ Versus L_d/S_d For Various L_b/S_b



Biographical Note

Osa Edward Fitch was born in Stillwater, Oklahoma, on February 15, 1960. After an extended stay of approximately 2 weeks, he moved to Pensacola, Florida, which set a pattern of frequent moves that continues to the time of this writing. He has lived in Bermuda, Florida, California, Hawaii, Virginia, and Massachusetts, and has travelled through most of the fifty states. He considers himself a citizen of Texas, and has strong ties to Virginia as well.

Since the age of seven, the author has been fascinated by the idea of becoming an astronaut, and has bent all his efforts in that direction. With that goal in mind, he enrolled in MIT on an NROTC Scholarship with the intention of obtaining a degree in Aerospace engineering and becoming a Naval aviator. Having completed this program, he will receive his commission as an Ensign on May 31, 1982, and will graduate the following day. Through the NROTC program, he has attended the Airborne School at Fort Benning, Ga., and Winter Survival School at Brunswick, Me.

The author has also been active in supporting the Objectivist newspaper, **Ergo**, at MIT, where he has been production manager, and has written extensively. He is strongly committed to the philosophy of Objectivism and to the maintenance of Liberty and individual freedom.

The author is a member of Tau Beta Pi, the National Engineering Honor Fraternity, and Sigma Xi, the Scientific Research Society of North America.

Bibliography

Carlsaw, H. S., Jaeger, J. C., Conduction of Heat in Solids, Second Edition, Oxford at the Clarendon Press, 1959.

Gray, D. E., Coordinating Editor, American Institute of Physics Handbook, pg 5-165, McGraw Hill Book Company, New York, 1972.

Marcus, A., Operating Experience With The Fringe-Fibre Brush, paper released by Safety Electrical Equipment Corporation Division of Stone-Platt Industries, Ltd., Wallingford, Connecticut, 1981.

Mongeau, P. P., Coaxial Air Core Electromagnetic Accelerators, Ph. D. Thesis (Physics), Massachusetts Institute of Technology, Cambridge, Massachusetts, 1981.

Montgomery, D. B., Solenoid Magnet Design, Wiley, New York, 1969.

Thom, K., Norwood, J., Theory Of An Electromagnetic Mass Accelerator For Achieving Hypervelocities, NASA Technical Note D-886, June 1961.

Weast, R. C., Editor, CRC Handbook of Chemistry and Physics, 59th Edition, CRC Press Inc., West Palm Beach, Florida, 1978.

Zeitlin, M. J., Design, Construction, and Testing of an Electro-Magnetically Launched Model Glider, S. M. Thesis (Aeronautics and Astronautics), Massachusetts Institute of Technology, Cambridge, Massachusetts, 1981.